ISSN 0021-3438 (Print)
ISSN 2412-8783 (Online)

IZVESTIYA
NON-FERROUS METALLURGY

Vol. 31, No. 1, 2025

Scientific and Technical Journal
Founded in 1958
4 Issues per year

ИЗВЕСТИЯ ВУЗОВ
ЦВЕТНАЯ МЕТАЛЛУРГИЯ

Том 31, № 1, 2025

Научно-технический журнал
Основан в 1958 г.
Выходит 4 раза в год

ISSN 0021-3438 (Print)
ISSN 2412-8783 (Online)

IZVESTIYA NON-FERROUS METALLURGY

Vol. 31, No. 1
2025

Scientific and Technical Journal Founded in 1958 4 Issues per year http://cvmet.misis.ru

Journal is included into the List of the peer-reviewed scientific publications recommended by the Highest Attestation Commission of the Ministry of Education and Science of the Russian Federation for publishing the results of doctoral and candidate dissertations

Abstracting/Indexing: Russian Science Citation Index (RSCI), Chemical Abstracts (Online), INIS, OCLC ArticleFirst, Ulrich's Periodicals Directory, VINITI Database (Abstract Journal)

Founder

National University of Science and Technology "MISIS"
Address: 1 Bld, 4 Leninskiy Prosp., Moscow 119049, Russia
http://www.misis.ru

Editorial Staff

Address: NUST MISIS, 1 Bld, 4 Leninskiy Prosp., Moscow 119049, Russia
Phone: +7 (495) 638-45-35
E-mail: izv.vuz@misis.ru

Leading Editor – A.A. Kudinova
Executive Editor – O.V. Sosnina
Layout Designer – E.A. Legkaya

Certificate of registration No. 015842 (13.03.1997)
Re-registration PI No. ФС77-79229 (25.09.2020)

Subscription: Ural-Press Agency

Signed print 17.03.2025. Format 60×90 1/8.
Offset paper No. 1. Digital printing. Quires 11,25
Order 21751. Free price

Printed in the printing house of the MISIS Publish House
1 Bld, 4 Leninskiy Prosp., Moscow 119049, Russia. Phone/fax: +7 (499) 236-76-17

ISSN 0021-3438 (Print)
ISSN 2412-8783 (Online)

ИЗВЕСТИЯ ВУЗОВ
ЦВЕТНАЯ МЕТАЛЛУРГИЯ

Том 31, № 1
2025

Научно-технический журнал Основан в 1958 г. Выходит 4 раза в год http://cvmet.misis.ru

Журнал включен в Перечень рецензируемых научных изданий, рекомендованных ВАК Минобрнауки РФ для публикации результатов диссертаций на соискание ученых степеней

Журнал включен в базы данных: Russian Science Citation Index (RSCI), Chemical Abstracts (Online), INIS, OCLC ArticleFirst, Ulrich's Periodicals Directory, РИНЦ, БД/РЖ ВИНИТИ

Учредитель

ФГАОУ ВО Национальный исследовательский технологический университет «МИСИС»
Адрес: 119049, г. Москва, Ленинский пр-т, 4, стр. 1
http://www.misis.ru

Редакция журнала

Адрес: 119049, г. Москва, Ленинский пр-т, 4, стр. 1, НИТУ МИСИС
Тел.: +7 (495) 638-45-35
E-mail: izv.vuz@misis.ru

Свидетельство о регистрации № 015842 от 13.03.1997 г.
Перерегистрация ПИ № ФС77-79229 от 25.09.2020 г.

Подписка: Агентство «Урал-пресс»

Ведущий редактор – А.А. Кудинова
Выпускающий редактор – О.В. Соснина
Дизайн и верстка – Е.А. Легкая

Подписано в печать 17.03.2025. Формат 60×90 1/8.
Бум. офсетная № 1. Печать цифровая. Усл. печ. л. 11,25
Заказ 21751. Цена свободная

Отпечатано в типографии Издательского Дома МИСИС
119049, г. Москва, Ленинский пр-т, 4, стр. 1. Тел./факс: +7 (499) 236-76-17

CONTENTS

СОДЕРЖАНИЕ

Metallurgy of non-ferrous metals

Foundry

Physical metallurgy and heat treatment

Energy and resource saving

Металлургия цветных металлов

Литейное производство

Металловедение и термическая обработка

Энерго- и ресурсосбережение

UDC 669.334.6
https://doi.org/10.17073/0021-3438-2025-1-5-13

Research article
Научная статья

Pilot tests for processing oxidized copper ores from the Erdenetiin Ovoo deposit using heap leaching

S. Gantulga[1], Ts. Tsend-Ayush[2], B. Altantuyaa[1], S.V. Mamyachenkov[3]

[1] **Mongolian University of Science and Technology**
34 Sukhebator Str., Ulaanbaatar 14191, Mongolia

[2] **SOE "Erdenet Enterprise"**
Friendship Square, Erdenet, Orkhon aimag 61027, Mongolia

[3] **Ural Federal University n.a. the First President of Russia B.N. Eltsin**
19 Mira Str., Ekaterinburg 620002, Russia

✉ Sergey V. Mamyachenkov (svmamyachenkov@yandex.ru)

Abstract: In the current context of declining reserves of high-grade copper sulfide ores, oxidized ores are becoming an important source of mineral raw materials containing non-ferrous and precious metals. Traditional flotation processing of these ores results in low-grade concentrates with poor metal extraction rates (40–60 %). Heap leaching is considered the most promising method for processing such ores. As a result of prolonged intensive mining at the Erdenetiin Ovoo deposit (Erdenet, Mongolia), approximately 800 million tonnes of oxidized ore dumps with an average copper content of 0.45–0.48 % have accumulated within the open-pit boundary. Global experience in processing such secondary raw materials demonstrates the high economic efficiency of copper extraction through heap leaching, followed by solvent extraction and electrowinning (SX-EW) of copper from the pregnant leach solution. For the State-owned Enterprise Erdenet, it is essential to conduct leaching studies on oxidized ores and pilot testing of this technology on the ore from existing ore dumps. To achieve this, 35 boreholes were drilled in the dumps (16 in dump No. 8a and 19 in dump No. 12), from which core samples were collected. The mineralogical composition of the oxidized copper ore samples was analyzed, and the effect of heap leaching parameters (ore particle size, solution acidity, etc.) on copper recovery into the pregnant leach solution was determined. To more accurately assess the recoverable copper from the two dumps, composite samples were collected from each borehole, and large-scale heap leaching tests were conducted in 30 open-cycle columns. The test results showed that copper extraction rate from dump No. 8a ranged from 35.8 % to 69.1 %, with an average of 56.0 %, while dump No. 12 exhibited extraction rates ranging from 51.8 % to 77.4 %, with an average of 63.6 %.

Keywords: Erdenetiin Ovoo oxidized copper ore, mineralogical analysis, heap leaching, sulfuric acid consumption, particle size, copper extraction.

For citation: Gantulga S., Tsend-Ayush Ts., Altantuyaa B., Mamyachenkov S.V. Pilot tests for processing oxidized copper ores from the Erdenetiin Ovoo deposit using heap leaching. *Izvestiya. Non-Ferrous Metallurgy*. 2025;31(1):5–13.
https://doi.org/10.17073/0021-3438-2025-1-5-13

Полупромышленные испытания переработки окисленных медных руд месторождения Эрдэнэтийн Овоо методом кучного выщелачивания

С. Гантулга[1], Ц. Цэнд-Аюуш[2], Б. Алтантуяа[1], С.В. Мамяченков[3]

[1] **Монгольский университет науки и технологии**
Монголия, 14191, Улан-Батор, ул. Сухэбатора, 34

[2] **ПГС «Предприятие Эрдэнэт»**
Монголия, 61027, Орхонский аймак, г. Эрдэнэт, Площадь Дружбы

[3] **Уральский федеральный университет им. первого Президента России Б.Н. Ельцина**
Россия, 620002, г. Екатеринбург, ул. Мира, 19

✉ Сергей Владимирович Мамяченков (svmamyachenkov@yandex.ru)

Аннотация: В современных условиях сокращения запасов богатых медных сульфидных руд источником минерального сырья, содержащего цветные и благородные металлы, становятся окисленные руды. При их переработке традиционным флотационным методом получают низкосортные концентраты при низком (40–60 %) извлечении металлов. Наиболее перспективным направлением переработки подобных руд является кучное выщелачивание. В результате многолетней интенсивной эксплуатации месторождения Эрдэнэтийн Овоо (г. Эрдэнэт, Монголия) в контуре карьера накоплено около 800 млн т отвалов окисленной руды со средним содержанием меди 0,45–0,48 %. Мировой опыт переработки такого техногенного сырья показывает высокую экономическую эффективность извлечения меди методом кучного выщелачивания с последующим извлечением меди из продуктивного раствора по технологии «экстракция–электролиз». Для ПГС «Предприятие Эрдэнэт» актуально проведение исследований выщелачивания окисленных руд и укрупненных испытаний технологии на руде существующих отвалов. Для решения поставленной задачи в отвалах пробурено 35 скважин (16 – в отвале № 8а и 19 – в отвале № 12), из которых получены керновые пробы. Изучен минералогический состав проб окисленной медной руды, определено влияние условий кучного выщелачивания (крупности руды, кислотности раствора и др.) на показатели перевода меди в продуктивный раствор. Для более точного определения количества меди, которое можно получить методом выщелачивания из двух отвалов, из каждой скважины отобрана составная (композитная) проба и в 30 колоннах проведены укрупненные испытания кучного выщелачивания в открытом цикле. В результате этих испытаний для отвала № 8а извлечение меди составило от 35,8 до 69,1 % (среднее значение – 56,0 %), а для отвала № 12 – варьировалось в диапазоне 51,8–77,4 % (среднее значение – 63,6 %).

Ключевые слова: окисленная медная руда Эрдэнэтийн Овоо, минералогический анализ, кучное выщелачивание, расход серной кислоты, крупность, извлечение меди.

Для цитирования: Гантулга С., Цэнд-Аюуш Ц., Алтантуяа Б., Мамяченков С.В. Полупромышленные испытания переработки окисленных медных руд месторождения Эрдэнэтийн Овоо методом кучного выщелачивания. *Известия вузов. Цветная металлургия*. 2025;31(1):5–13. https://doi.org/10.17073/0021-3438-2025-1-5-13

Introduction

As of January 1, 2022, the geological services of the state-owned mining and processing enterprise Erdenet Mining Corporation (Mongolia) estimated the reserves of oxidized copper ore in dumps No. 8a and 12 of the Erdenetiin Ovoo deposit at 49.0 million tonnes, with an average copper content of 0.48 %. In the near future, Erdenet Mining Corporation plans to construct a cathode copper production plant to process oxidized ore using the Heap Leach — Solvent Extraction/Electrowinning (HL-SX/EW) technology.

Mined ore that did not meet processing grade requirements was stockpiled in dumps No. 8a and 12 over many years. This long-term accumulation led to significant alterations in the ore properties due to natural environmental factors such as precipitation, wind, and temperature fluctuations. Representative samples were collected to determine copper content, phase composition, the suite of minerals present in the ore, and their solubility. These data were then used to forecast the potential technical

and economic indicators of heap leaching for this material.

The hydrometallurgical heap leaching (HL-SX/EW) technology is considered one of the most promising methods for processing oxidized copper ore due to its low-cost and environmentally friendly characteristics [1—3]. Erdenet Mining Corporation aims to build a cathode copper production facility based on this process, using ore extracted from waste dumps [4; 5].

The ore in dumps No. 8a and 12 has a relatively high copper content (0.48 %). Since this oxidized ore was stockpiled over an extended period, it exhibits a high degree of oxidation influenced by natural weathering and climate conditions. Preliminary leaching tests on these dumps have been conducted since 2014 by institutions such as the Chinese BGRIMM Institute and the Technological Research Laboratory (TRL) of MAK LLC (Russia). Samples for these tests were collected from the dump surface using an excavator bucket at depths of 2.0—2.8 m. Consequently, the representativeness of these samples is considered insufficient [6; 7]. Column leaching tests conducted by BGRIMM established that copper extraction rates of 40—50 % could be achieved. Meanwhile, TRL tests, which employed additional leaching enhancement techniques, indicated that leaching could extract between 35 % and 80 % of the total copper into the pregnant leach solution. These results highlight a broad range of potential copper extraction rates [8; 9].

To obtain more accurate data, semi-industrial-scale tests were performed using samples from 35 boreholes drilled in dumps No. 8a and 12 at depths ranging from 18 to 75 m. These samples exhibited high representativeness, and composite samples were prepared based on the weight ratio of each borehole. These composite samples were then subjected to heap leaching in large-scale test columns (30 columns).

Sample preparation

Core samples from dumps No. 8a and 12 were screened through a 75 mm mesh sieve. The +75 mm fraction was crushed using a jaw crusher with a 35 mm discharge gap to achieve a particle size of –75 mm (100 % passing) for heap leaching tests.

The sequence of sample preparation and chemical analysis is shown in Fig. 1.

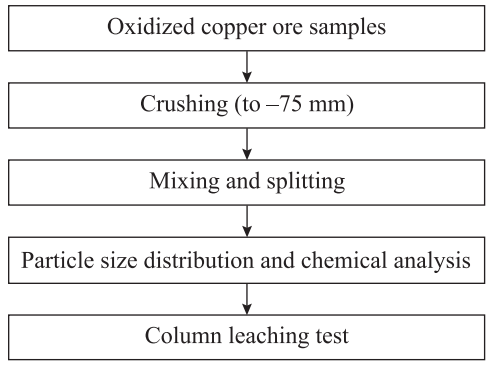

Fig. 1. Sequence of sample preparation and chemical analysis

Рис. 1. Последовательность пробоподготовки и химического анализа

Pilot column leaching tests

Pilot column leaching tests were conducted in accordance with widely used methodologies [10—12]. Copper extraction depends on numerous factors, such as the particle size distribution of the ore, total copper content, the distribution of primary sulfide and oxidized copper, mineral composition, temperature and leaching duration, initial solution concentration, and the flow rate of the diluted sulfuric acid solution [13—15].

The column leaching tests were carried out under the following conditions:

— ore particle size: 100 % passing –75 mm (with 80 % of the fraction in the range of 17.8—33.1 mm, corresponding to P_{80});

— leaching duration: 93—95 days;

— sulfuric acid concentration: 20 g/dm^3 during the first 5 days, 15 g/dm^3 from days 6 to 10, 10 g/dm^3 from days 11 to day 40, and 5 g/dm^3 for the remaining period;

— leachate application rate: 6.1 dm^3/(m^2·h);

— acid leaching method: uniform distribution from the top of the column;

— number of columns: 30.

The schematic diagram of the column leaching tests is shown in Fig. 2.

When the copper leaching rate slowed down, the process was halted by stopping the supply of the leaching solution. This was followed by rinsing with clean water for 24 h to drain the residual solution. After drainage, the moist ore samples were extracted from the columns, air-dried in an open area, screened using the standard method, and composite samples (collected while maintaining the ratio of the original sample and ore particle size) were analyzed for each fraction.

Mineralogical analysis

The results of the copper speciation analysis indicate that in dump No. 8a, the content of primary copper is 31.1 %, secondary copper is 42.9 %, and oxidized copper

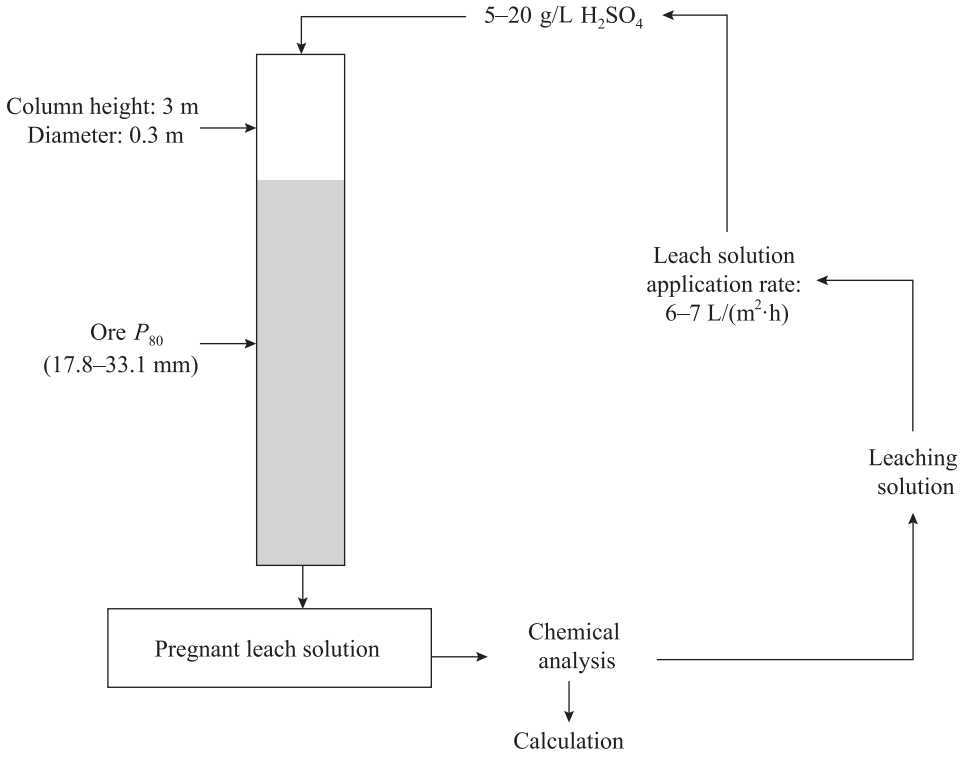

Fig. 2. Schematic diagram of the leaching tests

Рис. 2. Схема проведения испытаний

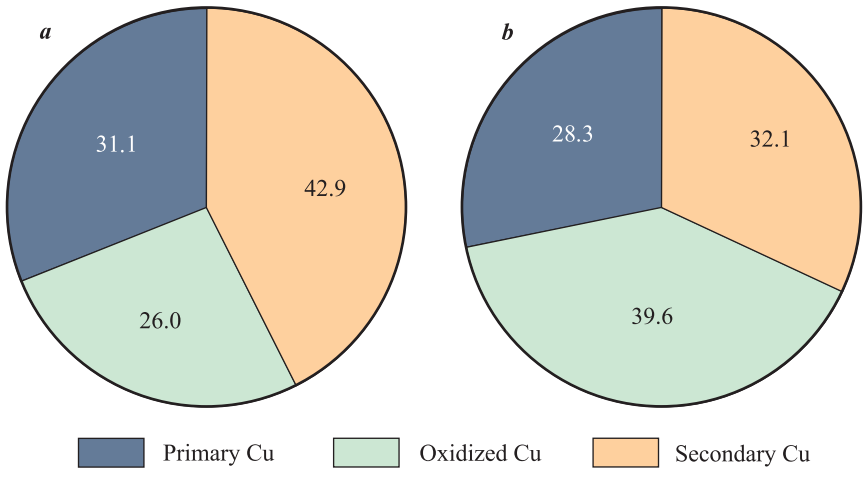

Fig. 3. Diagram of copper phase analyzes (%) in dumps No. 8a (***a***) and No. 12 (***b***)

Рис 3. Диаграмма анализов (%) медной фазы в отвалах № 8а (***a***) и 12 (***b***)

is 26.0 %. In dump No. 12, the average content of primary copper is 28.3 %, secondary copper is 32.1 %, and oxidized copper is 39.6 % (Fig. 3).

The results of the analysis of host rocks and ore minerals, conducted using *X*-ray diffraction (XRD) and a automated mineral analyzer (TIMA), are presented in Table 1.

The mineral composition of each dump differed significantly in the content of major rock-forming minerals such as quartz, plagioclase, potassium feldspar, muscovite, and pyrite, while the content of other minerals was similar.

Copper minerals are present as aggregates tightly intergrown with the gangue matrix. Spatially, covellite tends to displace and replace chalcopyrite and pyrite grains within the gangue matrix.

Table 1. **Mineral composition (%) of dumps No. 8a and 12**

Таблица 1. Минеральный состав (%) отвалов № 8а и 12

No.	Type	Mineral composition	Dump No.	
			8a	12
1	Gangue minerals	Quartz	25.8	28.7
2		Plagioclase	37.4	29.7
3		Feldspar	9.2	6.8
4		Muscovite	15.7	18.1
5		Clay minerals	7.43	13.05
6		Carbonates	0.36	0.35
7		Other minerals	1.27	1.34
8	Ore minerals	Pyrite	1.48	0.66
9		Copper-bearing minerals	0.82	0.76
10		Hematite	0.32	0.36
11		Sphalerite	0.13	0.14
12		Molybdenite	0.02	0.01
			100	100

Results of pilot column leaching tests

The relationship between copper extraction rate and leaching time is shown in Fig. 4.

It is evident that for the oxidized ore dumps No. 8a and 12, the copper dissolution process proceeded relatively quickly during the first 17 days, after which it began to stabilize.

Fig. 5 illustrates the total copper recovery, as well as copper extraction rate averaged for each phase and across different particle size classes.

A general trend observed is that oxidized copper minerals exhibit good solubility across all particle size classes, while primary and secondary sulfide copper minerals show relatively lower dissolution rates. Copper extraction rate into the solution is highest for samples with a particle size of –6.3 mm. For particle sizes ranging from –25 mm to +6.3 mm, the copper extraction can be described as moderate, while for coarser particles, it is minimal. This behavior is attributed to the fact that the leaching rate in a heterogeneous system strongly depends on the reactive surface area. Additionally, due to the large number of copper mineral particles in the finer fractions—liberated from the rock-forming materials—favorable conditions are created for effective interaction with sulfuric acid. This, in turn, enhances the leaching process [16—20].

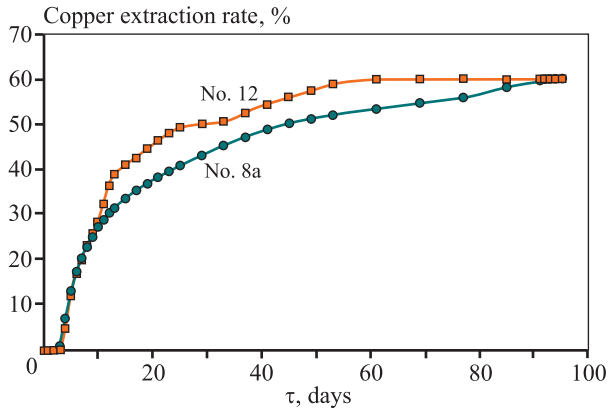

Fig. 4. Copper extraction rate during the leaching process

Рис. 4. Извлечение меди в процессе выщелачивания

For the pilot column leaching test samples, copper extraction values were calculated, chemical analyses were conducted, and the particle size distribution of the loaded samples (P_{80}) from dumps No. 8a and 12 was determined. The results are presented in Tables 2 and 3.

For dump No. 8a, copper extraction rate ranged from 35.8 % to 69.1 % with sulfuric acid consumption between 2.0 and 22.6 kg/t (average value — 23.11 kg/t). The ore particle size, represented by the P_{80} value (the sieve size through which 80% of the material passes), ranged from 17.8 to 33.1 mm. In dump No. 12, copper extraction rate ranged from 51.81 % to 77.4 %, with sulfuric acid consumption between 22.8 and 24.6 kg/t (average consumption — 23.3 kg/t), and the P_{80} value ranged from 18.1 to 29.3 mm.

Copper extraction rate was calculated using two methods based on the copper content in the leaching residue and the pregnant leach solution [21]:

— comparing the copper content in the leaching residue with the copper content in the pre-leaching samples;

— comparing the amount of copper in the total solution collected during leaching with the amount of copper in the pre-leaching sample.

Conclusions

1. Previously, the average copper content in the oxidized ore dumps No. 8a and 12 of the Erdenetiin Ovoo deposit was estimated using Micromine software at 0.47—0.49 %, with a degree of oxidation of 14.7—20.5 %. According to the results of this study, the average copper content was found to be 0.30—0.38 %, and the oxidation degree ranged from 25.6 % to 41.2 %. This demonstrates the influence of natural factors on changes in ore pro-

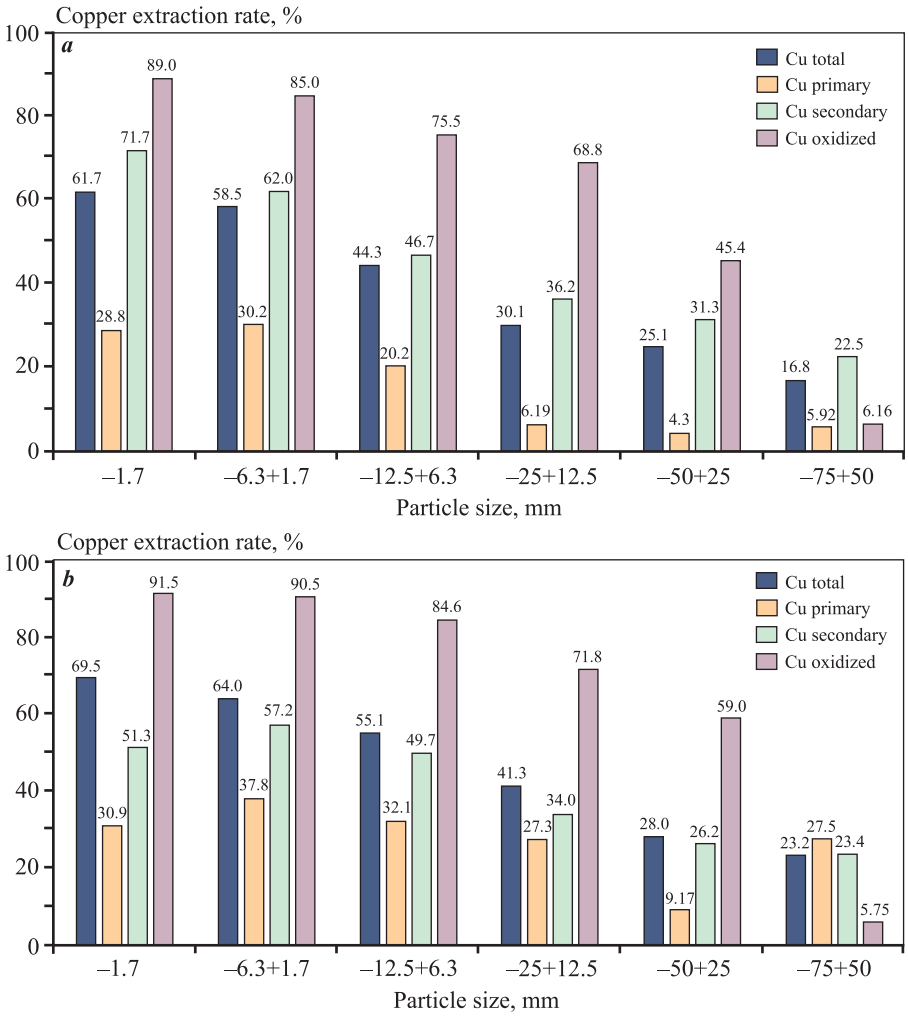

Fig. 5. Diagram of total copper recovery and copper extraction rate by particle size fraction for dump No. 8a (***a***) and dump No. 12 (***б***)

Рис. 5. Диаграмма общего извлечения меди и извлечения меди по каждой фракции для отвала № 8а (***a***) и отвала № 12 (***b***)

perties within the dumps. It was established that the oxidation rate of dump ores in the Erdenet region exceeds 0.6 % per year.

2. Based on the pilot column leaching tests, copper extraction rate ranged from 35.8 % to 69.0 % for dump No. 8a, with an average of 56.0 %, and from 51.8 % to 77.4 % for dump No. 12, with an average of 63.6 %. Since dump No. 12 has a higher oxidation degree, its copper extraction rate was also higher compared to dump No. 8a.

3. In borehole samples from dumps No. 8a and 12, the quartz content was 25.86 % and 29.46 %, plagioclase — 37.46 % and 34.72 %, potassium feldspar — 9.21 % and 6.88 %, muscovite — 15.74 % and 18.05 %, and pyrite — 1.48 % and 0.66 %, respectively. Summarizing the mineral composition for each dump revealed significant differences in the content of major rock-forming minerals (quartz, plagioclase, potassium feldspar, and muscovite), while the content of other minerals was similar. dump No. 8a showed higher pyrite content and the presence of sulfide minerals with relatively larger particle sizes. A distinctive feature of dump No. 12 samples was the relatively low number of pyrite particles, reduced grain sizes of sulfide minerals, and chalcopyrite observed as rims surrounded by secondary copper minerals.

4. Particle size and copper phase distribution significantly affect copper extraction rate during heap leaching. For both dumps, approximately 60 % of the total dissolved copper was extracted from the –1.7 mm size fraction, which accounted for less than 30 % of the total ore weight. However, the recovery of coarse fractions during screening and the copper extraction rate from coarse-grained fractions remained low.

5. It was determined that when the mass fraction of fine particles (–1.7 mm) exceeds 30 %, there is an increased risk of reduced solution permeability. Fine-

Table 2. **Generalized test results (dump No. 8a)**

Таблица 2. Обобщенные результаты испытаний (отвал № 8а)

No.	Time, days	Particle size P_{80}, mm	Cu_{total}	Phase analysis, %			Fe_{total}	Extraction, %	
				Cu_{prim}	Cu_{ox}	Cu_{sec}		Cu	Fe
1	95	18	0.36	26.4	25.6	48.0	3.17	54.5	2.5
2	95	25	0.26	29.3	27.4	42.9	3.28	61.7	3.4
3	95	22	0.29	28.1	31.5	40.1	2.91	68.1	8.3
4	95	18	0.34	35.2	34.6	29.9	2.96	50.8	4.1
5	95	27	0.45	20.3	27.1	52.6	2.56	69.1	10.5
6	95	33	0.29	34.3	23.1	42.7	2.84	61.0	8.7
7	95	21	0.32	25.0	36.4	38.6	2.63	54.7	8.6
8	95	25	0.28	28.3	20.4	51.3	3.27	57.3	5.1
9	95	25	0.27	35.1	18.7	46.3	2.96	46.5	6.6
10	93	22	0.25	37.5	15.1	47.4	2.99	47.5	8.6
11	93	21	0.32	26.7	32.6	40.7	3.11	60.7	6.0
12	95	18	0.27	46.4	16.1	37.1	3.31	35.8	8.4
13	95	19	0.25	34.4	24.3	41.3	3.10	50.0	6.4
14	93	20	0.29	18.9	25.2	55.9	3.61	66.1	10.2
Average values		**22**	**0.30**	**30.5**	**25.6**	**43.9**	**3.05**	**56.0**	**7.0**

Table 3. **Generalized test results (dump No. 12)**

Таблица 3. Обобщенные результаты испытаний (отвал № 12)

No.	Time, days	Particle size P_{80}, mm	Cu_{total}	Phase analysis, %			Fe_{total}	Extraction, %	
				Cu_{prim}	Cu_{ox}	Cu_{sec}		Cu	Fe
1	95	19	0.29	22.3	58.9	18.8	2.35	72.0	6.0
2	95	22	0.37	27.4	29.1	43.5	2.76	54.0	13.0
3	95	25	0.33	24.8	40.2	35.0	2.84	63.7	10.4
4	95	27	0.44	28.7	33.7	37.6	2.47	62.9	10.3
5	95	25	0.55	26.2	46.2	27.6	2.83	65.4	11.8
6	95	29	0.60	23.7	42.1	33.9	3.29	67.3	7.6
7	95	21	0.37	27.9	33.0	38.9	2.74	55.4	8.1
8	95	23	0.27	30.8	40.2	28.9	2.99	60.9	6.0
9	95	19	0.42	25.3	45.2	29.6	2.92	77.4	7.8
10	95	24	0.34	28.4	39.5	32.5	2.59	67.0	9.4
11	95	18	0.45	20.4	50.0	29.6	3.10	60.6	5.8
12	95	21	0.40	22.7	46.3	31.0	2.93	60.9	9.9
13	95	24	0.31	36.5	32.3	31.6	2.21	59.2	9.8
14	95	29	0.42	23.9	35.4	40.7	2.00	67.6	14.8
15	95	21	0.28	32.0	34.5	33.8	2.64	51.8	10.0
16	95	23	0.28	33.9	50.9	15.2	2.57	71.2	9.4
Average values		**23**	**0.38**	**27.1**	**41.1**	**31.8**	**2.70**	**63.6**	**9.4**

grained materials, which have a significant impact on copper extraction rate, may undergo agglomeration to improve solution permeability and enhance copper extraction rate.

6. Based on the pilot column leaching test results conducted on ores from the Erdenetiin Ovoo deposit, it is necessary to develop a mathematical model [22] that defines the relationships between factors affecting copper extraction rate. This model will be used to explore the possibility of achieving efficient copper extraction through heap leaching in a shorter time frame.

References

1. Purevdash M. Prospects for hydrometallurgical processing of oxidized copper ores and sulfide copper concentrates as an integral part of the new technology for complex processing of the Erdenetiin Ovoo deposit. *Zapiski Gornogo Instituta*. 2011;189:313—316. (In Russ.).
Пурэвдаш М. Перспективы гидрометаллургической переработки окисленных медных руд и сульфидных медных концентратов как составная часть новой технологии комплексной переработки месторождения «Эрдэнэтийн Овоо». *Записки Горного института*. 2011;189:313—316.
2. Bartos P.J. SX-EW copper and the technology cycle. *Resources Policy*. 2002;28(3-4):85—94. https://doi.org/10.1016/S0301-4207(03)00025-4
3. Ansah E.O., Jyoti A., Black J.R., Haese R.R. The importance of reaction mechanisms and coupled dissolution with reprecipitation (CDR) reactions when modelling copper leaching in heap systems. *Minerals Engineering*. 2023;203:108357. https://doi.org/10.1016/j.mineng.2023.108357
4. Trujillo J.Y., Cisternas L.A., Galves E.D., Mellado M.E. Optimal design and planning of heap leaching process. Application to copper oxide leaching. *Chemical Engineering Research and Design*. 2014;92(2):308—317. https://doi.org/10.1016/j.cherd.2013.07.027
5. Mortazavi A., Abbasloo Z., Ebrahimi L., Keshavars A., Masoomi A. Geotechnical investigation and design of leaching heap No. 2, Meydook copper mine, Iran. *Minerals Engineering*. 2015;79:185—195. https://doi.org/10.1016/j.mineng.2015.06.010
6. Robertson S.W., Staden P.J., Cherkaev A., Petersen J. Properties governing the flow of solution through crushed ore for heap leaching. *Hydrometallurgy*. 2022; 208:105811. https://doi.org/10.1016/j.hydromet.2021.105811
7. Lizama H.M. In-situ leaching of copper from spent heaps. *Hydrometallurgy*. 2023;215:105997. https://doi.org/10.1016/j.hydromet.2022.105997
8. Damdinzhav Zh., Sizyakov V.M., Brichkin V.P., Andreev E.E., Boduen A.Ya. Practice of heap leaching of refractory ores of the Erdenetiin Ovoo deposit. *Obogashchenie rud*. 2009;(5):3—5. (In Russ.).
Дамдинжав Ж., Сизяков В.М., Бричкин В.П., Андреев Е.Е., Бодуэн А.Я. Практика применения кучного выщелачивания труднообогатимых руд месторождения «Эрдэнэтийн Овоо». *Обогащение руд*. 2009;(5):3—5.
9. Khalezov B.D. Heap leachingof copper-zinc ores. Ekaterinburg: Ural Branch of the RAS, 2013. 346 p. (In Russ.).
Халезов Б.Д. Кучное выщелачивание медных и медно-цинковых руд. Екатеринбург: УрО РАН, 2013. 346 с.
10. Column Leaching Procedure. https://www.911metallurgist.com/hydrometallurgy-testing/ (accessed: 01.03.2024).
11. Staden P.J., Kolesnikov A.V., Petersen J. Comparative assessment of heap leach production data — 1. A procedure for deriving the batch leach curve. *Minerals Engineering*. 2017;101:47—57. https://doi.org/10.1016/j.mineng.2016.11.009
12. Robertson S.W. Development of an integrated heap leach solution flow and mineral leaching model. *Hydrometallurgy*. 2017;169:79—88. https://doi.org/10.1016/j.hydromet.2016.12.010
13. Wang L., Yin S., Wu A. Ore agglomeration behavior and its key controlling factors in heap leaching of low-grade copper minerals. *Journal of Cleaner Production*. 2021;279:123705. https://doi.org/10.1016/j.jclepro.2020.123705
14. Apua M.C., Mapilane S. Leaching kinetics and predictive models for elements extraction from copper oxide ore in sulphuric acid. *Journal of the Taiwan Institute of Chemical Engineers*. 2021;121:313—320. https://doi.org/10.1016/j.jtice.2021.04.005
15. Liu W., Hashemzadeh M. Solution flow behavior in response to key operating parameters in heap leaching. *Hydrometallurgy*. 2017;169:183—191. https://doi.org/10.1016/j.hydromet.2017.01.007
16. Kimball B.E., Rimstidt J.D., Brantley S.L., Chalcopyrite dissolution rate laws. *Applied Geochemistry*. 2010;25(7):972—983. https://doi.org/10.1016/j.apgeochem.2010.03.010
17. Cerqueira B., Covelo E.F., Rúa-Díaz S. Contrasting mobility of arsenic and copper in a mining soil: A comparative column leaching and pot testing approach. *Journal of Environmental Management*. 2022;318:115530. https://doi.org/10.1016/j.jenvman.2022.115530
18. Lizama H.M. How copper dump leaching works. *Minerals Engineering*. 2021;171:107075. https://doi.org/10.1016/j.mineng.2021.107075
19. Ansah E.O., Jyoti A., Black J.R., Haese R.R. The importance of reaction mechanisms and coupled dissolution with reprecipitation (CDR) reactions when modelling copper leaching in heap systems. *Minerals Engineering*. 2023;203:108357. https://doi.org/10.1016/j.mineng.2023/108357
20. Lichtner P.C. The quasi-stationary state approximation to coupled mass transport and fluid-rock interaction in a porous medium. *Geochimica et Cosmochimica Acta*. 1988;52:143—165. https://doi.org/10.1016/0016-7037(88)90063-4

21. Dzhartaeva I., Massakbayeva S. Investigation of factors affecting the process of heap leaching of copper ores. *Polish Journal of Science*. 2021;40:13—16.
22. Jamsa-Jounela S.L., Cziprian Z. Heap leaching simulation. In: *IFAC Symposium on Automation in Mining, Mineral and Metal Processing*. Cologne, Germany, 1998. P. 43—48. https://doi.org/10.1016/S1474-6670(17)35854-8

Information about the authors

Sambuu Gantulga – Master of science in engineering, Senior Engineer of the Technological park project unit, SOE "Erdenet Enterprise".
E-mail: gantulga.s@erdenetmc.mn

Tserendagva Tsend-Ayush – Ph.D, Head of the Development Department, SOE "Erdenet Enterprise".
E-mail: ts.tsendayush@erdenetmc.mn

Byambasuren Altantuyaa – Ph.D, Professor, Lecturer of the Institute of geology and mining engineering, Mongolian University of Science and Technology.
https://orcid.org/0000-0002-8414-9114?lang=en
E-mail: altantuya@must.edu.mn

Sergey V. Mamyachenkov – Dr. Sci. (Eng.), Head of the Department of metallurgy of non-ferrous metals, Ural Federal University n.a. the First President of Russia B.N. Eltsin.
https://orcid.org/0000-0002-4458-3792
E-mail: svmamyachenkov@yandex.ru

Информация об авторах

Самбуу Гантулга – магистр технических наук, ведущий инженер Проектной единицы, Производственно-технологический парк, ПГС «Предприятие Эрдэнэт».
E-mail: gantulga.s@erdenetmc.mn

Цэрэндагва Цэнд-Аюуш – к.т.н, начальник отдела развития ПГС «Предприятие Эрдэнэт».
E-mail: ts.tsendayush@erdenetmc.mn

Бямбасурэн Алтантуяа – к.т.н., профессор, преподаватель кафедры геологии и горной промышленности, Монгольский университет науки и технологии.
https://orcid.org/0000-0002-8414-9114?lang=en
E-mail: altantuya@must.edu.mn

Сергей Владимирович Мамяченков – д.т.н., заведующий кафедрой металлургии цветных металлов Уральского федерального университета им. первого Президента России Б.Н. Ельцина.
https://orcid.org/0000-0002-4458-3792
E-mail: svmamyachenkov@yandex.ru

Contribution of the authors

S. Gantulga – conducted experiments, prepared initial samples, participated in the discussion of results, drafted the manuscript, and formulated the conclusions.

Ts. Tsend-Ayush – defined the research objectives and participated in the discussion of results.

B. Altantuyaa – participated in the discussion of results and contributed to writing the manuscript.

S.V. Mamyachenkov – processed the results and edited the manuscript.

Вклад авторов

С. Гантулга – проведение экспериментов, приготовление исходных образцов, участие в обсуждении результатов, подготовка текста, формулировка выводов.

Ц. Цэнд-Аюуш – определение цели работы, участие в обсуждении результатов.

Б. Алтантуяа – участие в обсуждении результатов, написание статьи.

С.В. Мамяченков – обработка результатов, редактирование текста статьи.

The article was submitted 26.02.2024, revised 28.08.2024, accepted for publication 20.11.2024

Статья поступила в редакцию 26.02.2024, доработана 28.08.2024, подписана в печать 20.11.2024

METALLURGY OF NON-FERROUS METALS / МЕТАЛЛУРГИЯ ЦВЕТНЫХ МЕТАЛЛОВ

UDC 662.7.662.242
https://doi.org/10.17073/0021-3438-2025-1-14-26

Research article
Научная статья

Investigation of gold dissolution in cyanide solutions using cyclic voltammetry methods

A.N. Baranov[1], **V.V. Elshin**[1], **A.A. Kolodin**[1], **E.V. Filippova**[2]

[1] **Irkutsk National Research Technical University**
83 Lermontov Str., Irkutsk 664074, Russia

[2] **Federal Service for Environmental, Industrial and Nuclear Supervision**
1 Bld, 34 Taganskaya Str., Moscow 125993, Russia

✉ Anatoly N. Baranov (baranov@istu.edu)

Abstract: The study presents the results of gold dissolution in cyanide solutions using the cyclic voltammetry method. A methodology was developed to investigate the mechanism of gold leaching in cyanide solutions by determining the relationship between current and potential under varying cyanide and oxygen concentrations. It is known that as the electrode potential increases, the gold dissolution current rises until the passivation potential is reached, after which it sharply decreases due to the formation of an oxide film, resulting in gold passivation. It was established that the maximum passivation current is achieved at oxygen and sodium cyanide concentrations of 7.5 mg/dm^3 and 300–400 mg/dm^3, respectively. Mathematical relationships for the passivation potential and current as functions of sodium cyanide and oxygen concentrations were determined, described by polynomial equations with approximation coefficients $R_2 > 0.7$. When the polarization direction is reversed, the current polarity changes, producing a cathodic curve with a peak at the depassivation potential, corresponding to the dissolution of the passive gold film. The depassivation potential and current show weak dependence on sodium cyanide concentration. The cyclic voltammetric curve terminates at the initial point with the same current and potential values, indicating the complete removal of the oxide film from the gold surface. The oxide film thickness, calculated based on the amount of passed charge, was found to be 0.007 μm. Metallographic studies demonstrated that the film thickness could not be determined by this method. A gold surface diffractogram revealed that the passive film formed after heating to 125 °C has the crystallochemical formula $Na_{0.66}Au_{2.66}O_4$. The study highlights the potential for enhancing gold recovery from refractory ores through electrochemical treatment in alkaline conditions.

Keywords: gold, cyanidation, oxygen, electrochemistry, potentiostat, passivation, depassivation, current, potential, electron microscope, cyclic voltammetry, XRD patterns, redox potential.

For citation: Baranov A.N., Elshin V.V., Kolodin A.A., Filippova E.V. Investigation of gold dissolution in cyanide solutions using cyclic voltammetry methods. *Izvestiya. Non-Ferrous Metallurgy.* 2025;31(1):14–26. https://doi.org/10.17073/0021-3438-2025-1-14-26

Исследование растворения золота в цианистых растворах методами циклической вольтамперометрии

А.Н. Баранов[1], **В.В. Ёлшин**[1], **А.А. Колодин**[1], **Е.В. Филиппова**[2]

[1] **Иркутский национальный исследовательский технический университет**
Россия, 664074, г. Иркутск, ул. Лермонтова, 83

[2] **Федеральная служба по экологическому, технологическому и атомному надзору**
Россия, 125993, г. Москва, ул. Таганская, 34, стр. 1

✉ Анатолий Никитич Баранов (baranov@istu.edu)

Аннотация: Представлены результаты исследования растворения золота в цианистых растворах с применением метода циклической вольтамперометрии. Разработана методика исследования механизма выщелачивания золота в цианистых растворах путем

определения зависимости силы тока от потенциала при различных концентрациях цианида натрия и кислорода. Известно, что с повышением электродного потенциала ток растворения золота возрастает до потенциала пассивации, а затем резко снижается в связи с образованием оксидной пленки, и происходит пассивация золота. Установлено, что максимальное значение тока пассивации достигается при концентрациях кислорода и цианида натрия в растворе 7,5 и 300–400 мг/дм^3 соответственно. Определены математические зависимости потенциала и тока пассивации от концентраций цианида натрия и кислорода, которые описываются полиномиальными уравнениями с коэффициентами аппроксимации $R^2 > 0{,}7$. При смене направления поляризации полярность тока меняется, и образуется катодная кривая с максимумом при потенциале депассивации, которая связана с растворением пассивной пленки золота. Потенциал и ток депассивации слабо зависят от концентрации цианида натрия. Циклическая вольт-амперная кривая заканчивается в начальной точке при том же значении тока и потенциала, что свидетельствует об удалении оксидной пленки с поверхности золота. Толщина оксидной пленки установлена расчетными методами с учетом количества пропущенного электричества и составляет 0,007 мкм. Металлографические исследования показали, что толщина пленки этим методом не определяется. Дифрактограмма поверхности золота свидетельствует о том, что образующаяся пассивная пленка после нагрева до температуры 125 °С имеет кристаллохимическую формулу $Na_{0,66}Au_{2,66}O_4$. Показана возможность повышения извлечения золота из упорных руд путем электрохимической обработки щелочи.

Ключевые слова: золото, цианирование, кислород, электрохимия, потенциостат, пассивация, депассивация, ток, потенциал, электронный микроскоп, циклическая вольтамперометрия, дифрактограммы, окислительно-востановительный потенциал.

Для цитирования: Баранов А.Н., Ёлшин В.В., Колодин А.А., Филиппова Е.В. Исследование растворения золота в цианистых растворах методами циклической вольтамперометрии. *Известия вузов. Цветная металлургия.* 2025;31(1):14–26.
https://doi.org/10.17073/0021-3438-2025-1-14-26

Introduction

At present, cyanidation remains the primary method for extracting gold from ore. This process involves leaching precious metals using dilute solutions of cyanide salts in the presence of atmospheric oxygen, as shown in the reaction [1]:

$$2Au + 4NaCN + 0.5O_2 + H_2O = \\ = 2NaAu(CN)_2 + 2NaOH. \quad (1)$$

Gold dissolution follows an electrochemical mechanism, in which the ionization of metal atoms depends on the electrode potential. Electrochemical studies on the dissolution of gold in cyanide solutions at varying oxygen concentrations have been conducted in studies [2—4]. It is known that increasing the anodic potential raises the current intensity, thereby enhancing gold dissolution according to Faraday's law. Once a certain potential is reached, the current intensity sharply decreases due to gold passivation. This potential is defined as the passivation potential (E_{pas}). The passive state is attributed to the formation of a protective layer on the metal surface under specific conditions due to interactions with the environment. Corrosion studies of metals have shown that the dissolution rate increases as acid concentrations rise but then drops sharply and abruptly once a specific oxidant concentration is reached. This phenomenon has been extensively documented for iron, aluminum, chromium, and other metals in acidic solutions [5]. This behavior has also been observed for gold using potentiostatic polarization measurements [6]. Cyclic voltammetry (CV) is currently employed for more detailed investigations into corrosion mechanisms [7—11]. CV methods have been used to study the electrochemical behavior of electrodes made from various materials, such as glassy carbon and graphene/glassy carbon with deposited Au nanoparticles [12]. However, data on gold dissolution in cyanide solutions using these methods are lacking.

Enhancing the efficiency of the cyanidation process is of great importance, and various methods have been employed, including hydroacoustic [12], autoclave [13—15], electrochemical [16], photochemical [14], and other treatments to influence gold dissolution processes [17—22]. These methods, to varying degrees, alter the electrode potential of the noble metal. Therefore, studying the mechanism of gold electrochemical dissolution under different conditions using CV is highly relevant. The aim of this work is to investigate the kinetics of gold dissolution in cyanide solutions through CV measurements to elucidate the dissolution mechanism and the formation of passive films on the gold surface at different oxygen and sodium cyanide concentrations.

Methodology of experiments

Electrochemical studies were conducted by recording CV dependencies in cyanide solutions using a PI-50-PRO potentiostat-galvanostat. A 0.5 dm^3 cell was

used, containing a working gold electrode with a surface area of 0.567 cm^2, a platinum auxiliary electrode (EPV-1), a silver chloride reference electrode (EVP-08), and a WTW FDO 925 dissolved oxygen sensor. The oxygen concentration in the cell was regulated by supplying either argon or compressed air.

For the experiments, solutions with sodium cyanide (NaCN) concentrations ranging from 20 to 500 mg/dm^3 and a pH of 10—10.5 were prepared. The gold electrode was immersed to its maximum possible depth near a rotating magnetic stirrer. To reduce the diffusion resistance of gold dissolution, the stirrer was set to a high speed of 650 rpm, with a potential sweep rate of 3.74 mV/s. A 0.450 dm^3 solution with a specific NaCN concentration was added to the cell. The initial oxygen concentration in the solution was 7.5 mg/dm^3. Argon was used to adjust the oxygen concentration as needed.

The PI-50-PRO potentiostat was set to a polarization range of 100 to 1000 mV in both forward and reverse directions, with a sweep rate of 3.74 mV/s. After recording CV curves, argon was introduced into the solution to reduce the oxygen concentration to a specified level, and CV measurements were repeated. Thus, the oxygen concentration was gradually reduced from 7.5 to 0.01 mg/dm^3. At the end of each experiment, the solution was drained, and the cell was rinsed. Before and after each experiment, the NaCN concentration was measured using titration. Consequently, CV curves were obtained for all prepared solutions with varying NaCN concentrations and oxygen levels.

Results and discussion

Fig. 1 shows the CV curves with potentials referenced to the silver/silver chloride (Ag/AgCl) reference electrode.

The analysis of the typical CV dependencies in Fig. 1 made it possible to determine the passivation potentials (E_{pas}) corresponding to the maximum anodic current (I_{pas}). During the reverse sweep of the CV curves, from 1000 mV to 100 mV, the current polarity changes, and at the maximum cathodic depassivation current (I_{dep}), the depassivation potential (E_{dep}) can be identified.

It is known [5] that the current density serves as an electrochemical indicator of the mass rate of electrochemical corrosion (K_m), which can be applied to the gold leaching process, as this also proceeds spontaneously in cyanide solutions:

$$K_m = qIt/S. \quad (2)$$

Here, $K_m = m/(St)$ is the corrosion rate, g/(cm^2·s);

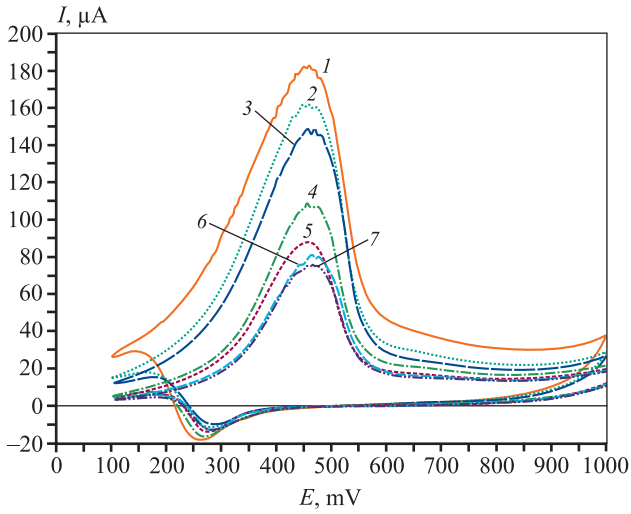

Fig. 1. Example of typical cyclic voltammograms at NaCN concentration of 200 mg/dm^3
C_{O_2}, mg/dm^3: ***1*** – 7.5; ***2*** – 3.0; ***3*** – 2.0; ***4*** – 1.3; ***5*** – 0.8; ***6*** – 0.4; ***7*** – 0.05

Рис. 1. Пример типичных цикличных вольт-амперных зависимостей при концентрации C_{NaCN} = 200 мг/$дм^3$
C_{O_2}, мг/$дм^3$: ***1*** – 7,5; ***2*** – 3,0; ***3*** – 2,0; ***4*** – 1,3; ***5*** – 0,8; ***6*** – 0,4; ***7*** – 0,05

m is the mass of dissolved gold, g; S = 0.567 cm^2 is the electrode area; t is time, s; $i = I/S$ is the current density, A/cm^2; q is the electrochemical equivalent of gold, equal to the atomic mass of gold (A) divided by the number of electrons (n) and Faraday's constant (F): $q = A/(nF)$ = 196.967/(1·96500) = 0.00204 g/(A·s).

At the initial stage of the CV measurements (Fig. 1), the gold corrosion rate was I/S = 29/0.567 = = 51 μA/cm^2, while at the passivation potential, it reached K_m = 180/0.567 = 317.5 μA/cm^2. This indicates that the gold dissolution rate can increase by a factor of 6.2 with a 350 mV positive shift in the gold electrode potential. Further increasing the potential to 600 mV results in reduced gold dissolution due to the formation of a passive film.

Two main theories describe the nature of the passivating layer: the phase and adsorption theories of passivity. According to the phase theory, passivity arises from the formation of a relatively thick phase film on the metal surface, consisting of corrosion products that isolate the metal from the corrosive medium. The phase theory links the determining influence of potential on the transition of the metal into a passive state with changes in the composition and crystalline structure of the corrosion products, and therefore, the protective properties of the films formed as the electrode potential increases. However, an independent phase film is not

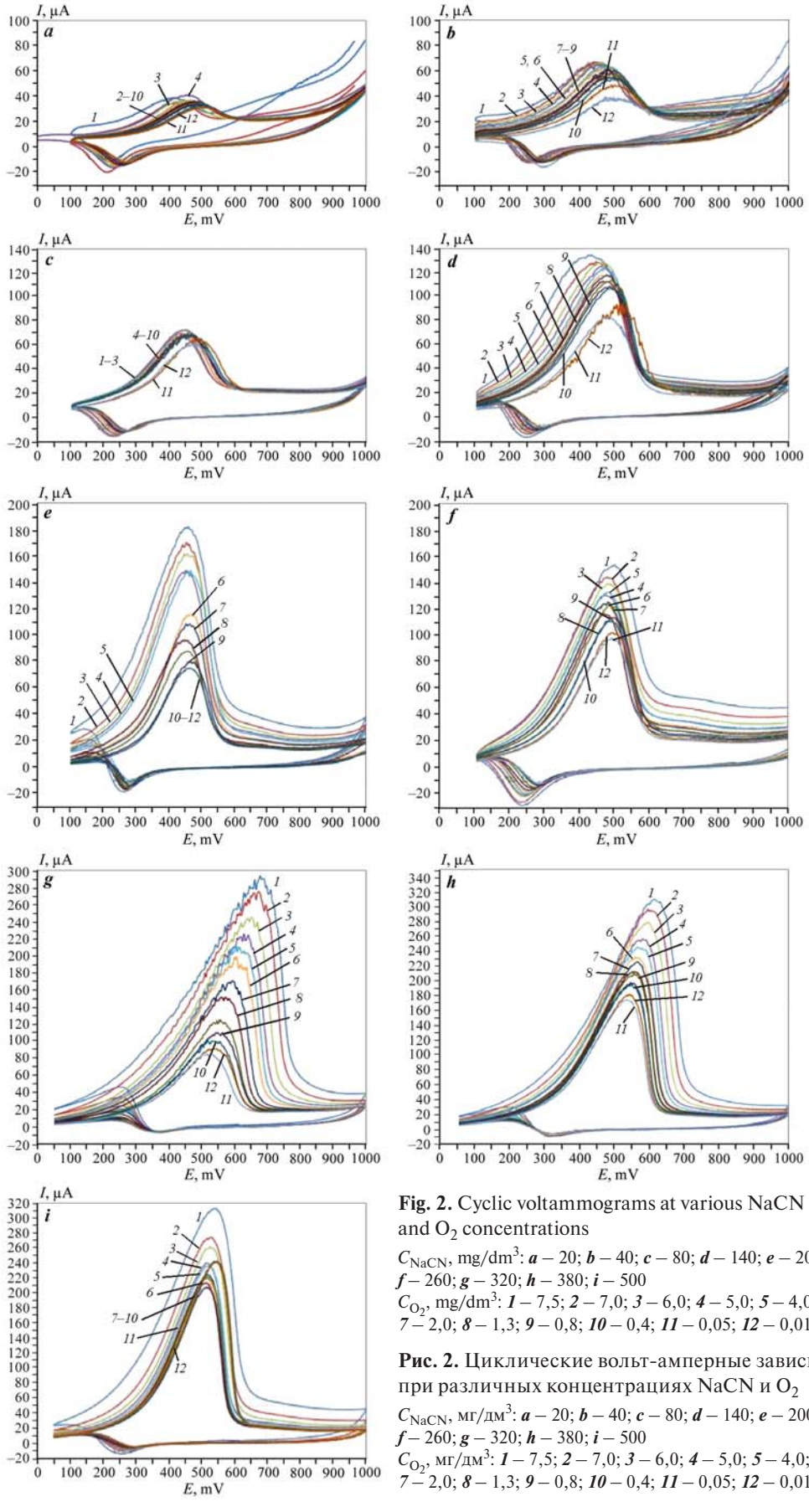

Fig. 2. Cyclic voltammograms at various NaCN and O_2 concentrations

C_{NaCN}, mg/dm^3: ***a*** – 20; ***b*** – 40; ***c*** – 80; ***d*** – 140; ***e*** – 200; ***f*** – 260; ***g*** – 320; ***h*** – 380; ***i*** – 500
C_{O_2}, mg/dm^3: ***1*** – 7,5; ***2*** – 7,0; ***3*** – 6,0; ***4*** – 5,0; ***5*** – 4,0; ***6*** – 3,0; ***7*** – 2,0; ***8*** – 1,3; ***9*** – 0,8; ***10*** – 0,4; ***11*** – 0,05; ***12*** – 0,01

Рис. 2. Циклические вольт-амперные зависимости при различных концентрациях NaCN и O_2

C_{NaCN}, мг/дм^3: ***a*** – 20; ***b*** – 40; ***c*** – 80; ***d*** – 140; ***e*** – 200; ***f*** – 260; ***g*** – 320; ***h*** – 380; ***i*** – 500
C_{O_2}, мг/дм^3: ***1*** – 7,5; ***2*** – 7,0; ***3*** – 6,0; ***4*** – 5,0; ***5*** – 4,0; ***6*** – 3,0; ***7*** – 2,0; ***8*** – 1,3; ***9*** – 0,8; ***10*** – 0,4; ***11*** – 0,05; ***12*** – 0,01

always observed on the surface of a metal in a passive state. The adsorption theory postulates that the metal transitions to a passive state due to the formation of a chemisorbed layer of an oxidant, such as oxygen, on its surface. We believe that both theories are applicable to the gold dissolution process and must be considered during gold leaching.

To establish the mechanism of gold passivation, Fig. 2 presents the CV measurement results in NaCN solutions with various oxygen concentrations (potentials are indicated in mV relative to the Ag/AgCl reference electrode).

According to the analysis of the CV dependencies (see Fig. 2), a current peak corresponding to the passivation potential is observed at various sodium cyanide concentrations. As the potential decreases from 1000 to 100 mV, the current reverses polarity, indicating the dissolution of the passive film. The maximum cathodic current, referred to as the depassivation current (I_{dep}), is reached at the depassivation potential (E_{dep}). Based on the obtained results (Fig. 2), the relationships between the passivation and depassivation currents and potentials with sodium cyanide concentration at an oxygen concentration of 7.5 mg/dm^3 were determined, as shown in Fig. 3. These relationships (Fig. 3) are described by polynomial equations of the following form:

$$E_{pas} = 360.93 + 1.0621C_{NaCN} - 0.0011C^2_{NaCN}, \quad R^2 = 0.6587, \tag{3}$$

$$I_{pas} = 12.637 + 0.9925C_{NaCN} - 0.0012C^2_{NaCN}, \quad R_2 = 0.7342, \tag{4}$$

$$E_{dep} = 229.9 + 0.3791C_{NaCN} + 0.00060012C^2_{NaCN}, \quad R_2 = 0.1954, \tag{5}$$

$$I_{dep} = 13.069 + 0.0723C_{NaCN} + 0.3797C^2_{NaCN}, \quad R^2 = 0.3797. \tag{6}$$

The analysis of the dependencies shown in Fig. 3, *a*, *b* indicates that they can be described by polynomial equations with approximation coefficients around 0.7, making them statistically significant. In contrast, the depassivation processes (Fig. 3, *c*, *d*) have lower approximation coefficients ($R_2 < 0.4$) and are not statistically significant. This suggests that the dissolution of the passive film is independent of the sodium cyanide concentration.

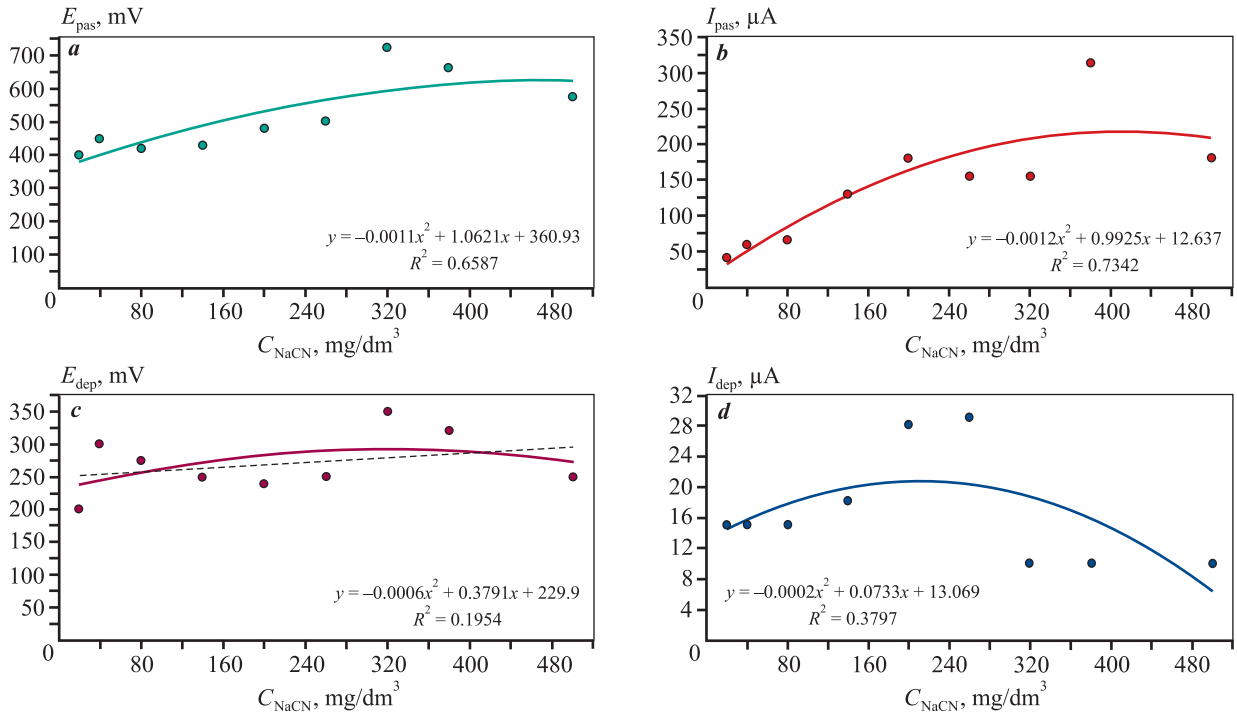

Fig. 3. Dependence of passivation potential (***a***), passivation current (***b***), depassivation potential (***c***), and depassivation current (***d***) on sodium cyanide concentration

Рис. 3. Зависимость потенциала пассивации (***a***), тока пассивации (***b***), потенциала депассивации (***c***), тока депассивации (***d***) от концентрации цианида натрия

The maximum passivation currents, according to equation (4), are reached at C_{NaCN} = 400 mg/dm^3. However, two visual maxima are observed at cyanide concentrations of 200 and 400 mg/dm^3. This could be attributed to the high uncertainty in determining the passivation current, and the application of statistical methods for data processing is necessary to improve reliability.

During the experiments, the sodium cyanide concentration in the solution was monitored before and after recording a series of CV curves at various cyanide concentrations. Fig. 4 presents the results of the reduction in NaCN concentration as a percentage of its initial value during CV measurements, with oxygen levels varying from 7.5 to 0.01 mg/dm^3 as shown in Fig. 2.

The change in sodium cyanide concentration as a function of its initial concentration is described by the following polynomial equation:

$$C_{NaCN} = 0.2776C_{н\,NaCN} - 0.0004C^2_{н\,NaCN} - 28.584, \quad R_2 = 0.9649. \tag{7}$$

The maximum reduction in NaCN concentration is 25.3 % at an initial sodium cyanide concentration of 370 mg/dm^3. Given that 0.45 dm^3 of solution was added to the cell, the maximum NaCN loss amounts to 42 mg during 12 CV measurements at different oxygen concentrations in a sodium cyanide solution with an initial concentration of 370 mg/dm^3.

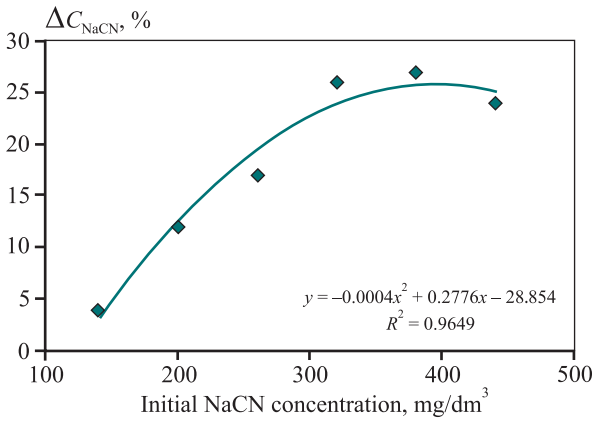

Fig. 4. Reduction in sodium cyanide concentration based on its initial concentration during CV measurements with varying oxygen levels

Рис. 4. Снижение концентрации цианистого натрия в зависимости от начальной его концентрации при снятии серии ЦВА с различной концентрацией кислорода

To provide more comprehensive information for selecting optimal leaching conditions based on oxygen concentration, three-dimensional diagrams were constructed to show the dependence of current or potential on sodium cyanide and oxygen concentrations.

Figures 5 and 6 present three-dimensional diagrams illustrating the dependence of current and potential on sodium cyanide and oxygen concentrations.

According to Fig. 5, the maximum passivation potential reaches 600 mV at a cyanide concentra-

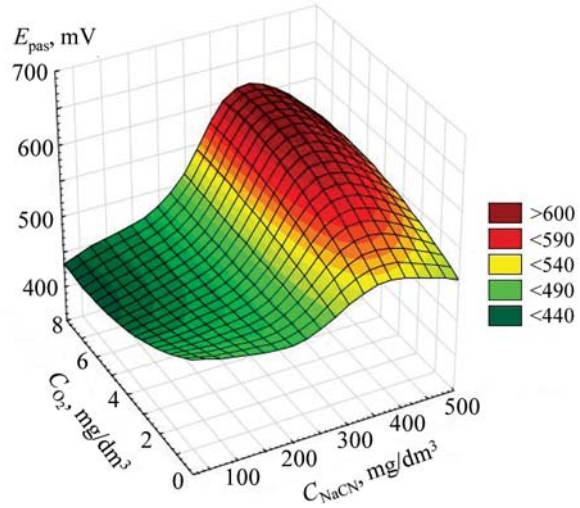

Fig. 5. Dependence of passivation potential on NaCN and O_2 concentration

Рис. 5. Диаграмма зависимости потенциала пассивации от концентраций NaCN и O_2

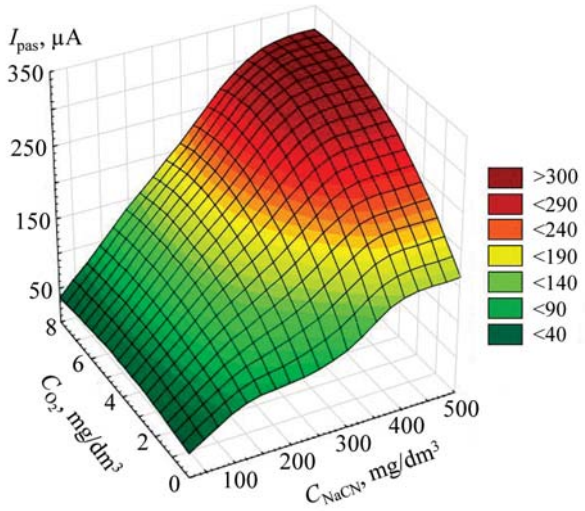

Fig. 6. Dependence of passivation current on NaCN and O_2 concentration

Рис. 6. Диаграмма зависимости тока пассивации от концентраций NaCN и O_2

tion of 400 mg/dm^3 and an oxygen concentration of 7.5 mg/dm^3.

According to Fig. 6, the maximum passivation current of 300 μA is observed at C_{NaCN} = 380 mg/dm^3 and C_{O_2} = 7.5 mg/dm^3. Notably, at an oxygen concentration of 0.05 mg/dm^3, the passivation current, and consequently the gold solubility, is 50 μA. This indicates that gold dissolves in cyanide solutions under anodic polarization even in the absence of oxygen. If oxygen does not participate in gold dissolution via reaction (1), the mechanism of anodic gold dissolution can be represented by the following reactions:

$$Au + 2(CN)^- - 2e = Au(CN)_2^-. \quad (8)$$

At the cathode, in the presence of oxygen, electrons are consumed by oxygen:

$$O_2 + 2H_2O + 2e = 4OH^-. \quad (9)$$

In the absence of oxygen, electrons are consumed during hydrogen evolution at the auxiliary platinum electrode:

$$2H^+ + 2e = H_2. \quad (10)$$

In [1], it was demonstrated that cyanide gold can form during leaching without anodic polarization via the following mechanism:

$$Au^+ + CN^- = AuCN. \quad (11)$$

This is possible considering that gold in the ore is often in contact with metal sulfides (pyrite, galena, etc.) that have high positive potentials. Cyanide gold does not dissolve directly but reacts with excess cyanide to form a complex compound, dicyanoaurate, which is capable of entering the solution:

$$AuCN + NaCN = Na[Au(CN)_2]. \quad (12)$$

Thus, to enhance the electrochemical dissolution of gold, it is recommended to increase the oxygen concentration and the electrode potential up to the passivation potential. When the electrode potential in a cyanide solution of 380 mg/dm^3 exceeds the passivation potential of 450 mV, a passive film forms, leading to a sharp decrease in current and, consequently, in gold dissolution.

To calculate the thickness of the passive gold film during CV measurements, the following electrochemical reaction occurring at the anode was considered: $Au - 1e = Au^+$. The obtained CV curves (see Fig. 2, *e*) show that as the potential increases, the current rises, and the amount of dissolved gold (m) can be calculated using Faraday's law:

$$m = qIt, \quad (13)$$

where I is the current, A; t is the time, s; q is the electrochemical equivalent of gold, equal to 0.002 g/(A·s).

The time can be determined based on the potential sweep rate v = 3.74 mV/s during CV measurements: $t = (E_{pas} - E_n)/v = (450 - 100)/3.74 = 93.58$ s. The current is obtained from the I—E (see Fig. 1) as the average between the initial current and the maximum current: $I = (182 - 27)/2 = 77.5$ μA = $77.5 \cdot 10^{-6}$ A. Let us calculate the amount of dissolved gold during a single CV measurement at a sodium cyanide concentration of 200 mg/dm^3 (see Fig. 1). For one CV measurement, the amount of dissolved gold is: $m = qIt = 0.002 \cdot 77.5 \cdot 10^{-6} \times \times 93.58 = 14.5 \cdot 10^{-6}$ g = 14.5 μg.

During passivation, the current decreases to its initial state, and a passive film forms through the following reactions: $Au - 3e = Au^{3+}$, $Au^{3+} + 3OH^- = = Au(OH)_3$. The amount of dissolved gold, based on equation (13), is $m = qIt = 0.00068 \cdot 77.5 \cdot 10^{-6} \cdot 93.58 = = 4.93 \cdot 10^{-6}$ g, where the electrochemical equivalent for Au^{3+} is 0.00068 g/(A·s). The mass of the passive $Au(OH)_3$ film (molecular mass = 237) can be calculated stoichiometrically as $237 \cdot 4.93 \cdot 10^{-6}/196.97 = = 5.93 \cdot 10^{-6}$ g. The thickness of the film is determined [23] by dividing the film mass by the product of the electrode area and the film density. Since the density of the film is not provided in reference data, it is calculated based on the additive properties of the specific densities. Considering that $Au(OH)_3$ contains 0.784 parts gold (ρ = 19.3 g/cm^3) and 0.215 parts $(OH)_3$ (ρ = 1 g/cm^3), the film density is 14.9 g/cm^3. The film thickness, given the electrode area of 0.567 cm^2, is calculated as $h = 5.93 \cdot 10^{-6}/(0.567 \cdot 14.9) = 0.7 \cdot 10^{-6}$ cm = = 0.007 μm. Table 1 presents the results of the calculations for the mass of dissolved gold, the stoichiometric calculation of cyanide consumption based on reaction (1) considering the mass of dissolved gold, and the calculated thickness of the passive film in the CV region, accounting for the formation of gold hydroxide.

The calculated thickness of the passive film (0.007 μm) is significantly smaller than passive films formed on metals like aluminum (0.01—1 μm). It is likely that the adsorption theory of passivity applies to films on gold, where a sharp decrease in anodic current occurs due to the formation of a chemisorbed oxygen layer, as observed on platinum with 1—6 % monolayer oxygen coverage [23]. Based on sodium cyanide consump-

Table 1. **Results of passive film thickness calculations**

Таблица 1. Результаты расчетов толщины пассивной пленки

CV range, mV (see Fig. 2, *e*)	Mass of dissolved gold, μg	Cyanide consumption per reaction (1), μg	Calculated passive film thickness, μm
100–450 (old dissolution)	4.94	2.54	–
450–700 (passive film formation)	5.96	2.97	0.007
Results of 12 CVs (at various oxygen concentrations)	130.9	66.1	–

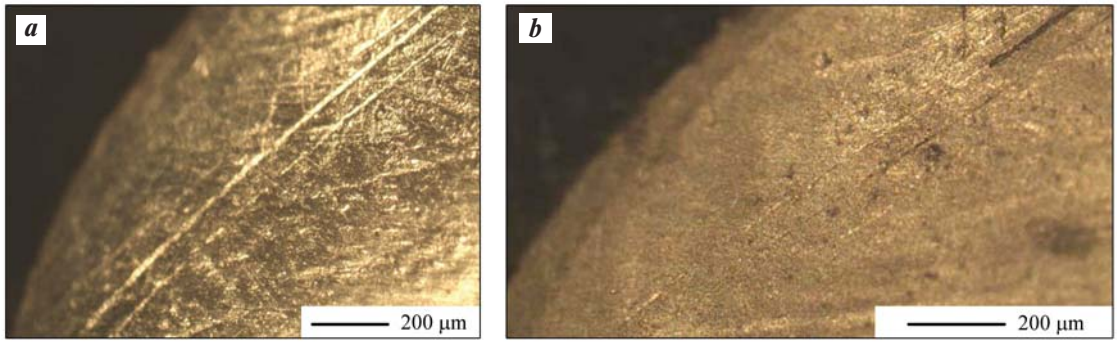

Fig. 7. Microstructures of the gold electrode before passivation (***a***) and after passivation (***b***)

Рис. 7. Микроструктуры золота на электроде до пассивации (***a***) и после пассивации (***b***)

tion, previous calculations showed that during 12 CV measurements, the reduction in cyanide concentration amounted to 42 mg, which greatly exceeds the amount required for the electrochemical dissolution of gold ($66.1 \cdot 10^{-6}$ g). This suggests that sodium cyanide decomposes during CV measurements.

To determine the actual thickness of the films on the obtained gold samples, metallographic studies were conducted. Microstructure imaging was performed using an inverted metallographic microscope (Olympus GX-51). Fig. 7 shows the microstructures of the gold electrode before and after passivation.

In Fig. 7, *a*, the clean gold surface shows visible lines from grinding and polishing. In Fig. 7, *b*, after passivation, the surface appears gray with no signs of roughness—likely due to the formation of a gold oxide film, the thickness of which cannot be determined using this method.

To investigate the composition of the film, a fragment of the Pourbaix diagram for gold is provided in Fig. 8 [24; 25].

The *E*—pH diagram for the Au—H_2O system indicates that gold hydroxide ($Au(OH)_3$) forms at pH = = 2÷11 and $E > 0.8$ V. At pH = 10 and $E > 2.0$ V AuO_2 is expected to form. Accordingly, on the recorded CV dependencies (see Fig. 2) at pH = 10 and $E > 0.8$ V, $Au(OH)_3$ likely forms. However, it is important to note that the Pourbaix diagram pertains to aqueous solutions, whereas the passive film in this study was formed in sodium cyanide solutions. To determine the composition of the passive film, an *X*-ray diffraction (XRD) analysis was performed using a Shimadzu XRD-7000 automatic powder diffractometer. A pure gold sample (1 cm^2) was prepared by grinding, polishing, degreasing in acetone, rinsing with distilled water, and passivating in a sodium cyanide solution (200 mg/dm^3) at $E > 650$ mV for 1 h. After drying at room temperature, the surface of the gold sample exhibited a dark brown coloration. The diffraction pattern of the passivated sample revealed no characteristic peaks corresponding to gold oxides or hydroxides, indicating that the passive film lacks a crystalline structure. According to [26; 27], gold hydroxide undergoes dehydration upon heating to 125 °C, initially forming AuO(OH), followed by sesquioxide (Au_2O_3), which decomposes into Au and O_2 at temperatures exceeding 160 °C. Therefore, in the second stage of the investigation, the gold sample was heated at 125 °C for 1 hour prior to recording the dif-

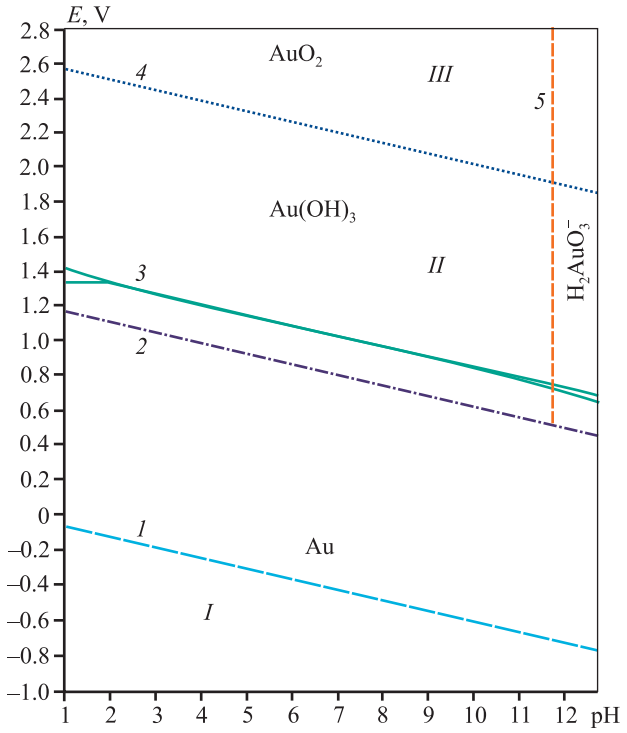

Fig. 8. Pourbet diagram for the Au–H_2O system at 25 °C [24; 25]
1, ***2*** – equilibrium lines of the hydrogen and oxygen electrodes;
3 – equilibrium line Au–$Au(OH)_3$; ***4*** – equilibrium line $Au(OH)_3$–AuO_2;
5 – equilibrium line AuO_2–$H_2AuO_3^-$
I – region of thermodynamic stability of gold; ***II*** – region of gold hydroxide ($Au(OH)_3$) formation; ***III*** – region of gold dioxide (AuO_2) formation

Рис. 8. Диаграмма Пурбе для системы Au–H_2O при температуре 25 °C [24; 25]
1, ***2*** – линии равновесия водородного и кислородного электродов;
3 – равновесная линия Au–$Au(OH)_3$; ***4*** – равновесная линия $Au(OH)_3$–AuO_2; ***5*** – равновесная линия AuO_2–$H_2AuO_3^-$
I – область термодинамической устойчивости золота;
II – область образования гидроксида золота $Au(OH)_3$;
III – область образования диоксида золота AuO_2

fraction pattern to further analyze the composition of the passive film.

Fig. 9 shows the diffraction pattern of the gold sample after passivation and heating, identifying the following compounds and their respective contents: Au (83 %); Au(CN) (0.05 %); $Na_{0.66}Au_{2.66}O_4$ (14 %); Cu (3 %). This indicates that sodium, cyanide, and oxygen participate in forming the passive film on gold. For the first time, a compound with the crystallochemical formula $Na_{0.66}Au_{2.66}O_4$, has been discovered, which can be interpreted as a double salt of the type $m(Na_2O)n(Au_2O_3)$. This compound was likely formed as a result of heating the gold sample. Consequently, the passive film in sodium cyanide solution consists of a hydroxide compound mNa(OH)nAu$(OH)_3$, which exists in an amorphous phase and does not produce diffraction lines. This supports the conclusion that gold passivation aligns with the adsorption theory of passivity.

Analyzing the obtained CV results on gold suggests the following dissolution mechanism. At an initial steady-state potential of 100 mV, the dissolution current ranges from 5 to 25 μA, depending on the oxygen concentration in the solution. During anodic polarization, the current increases exponentially, reaching 70—180 μA, with gold solubility increasing by a factor of 7—14, depending on the oxygen concentration. When the potential reaches 400—450 mV, the current increase stops. As an oxide film, mNa(OH)nAu$(OH)_3$, forms, the current decreases to 5—25 μA (depending on the oxygen concentration) at a complete passivation potential of 600 mV. This well-known property of metal passivation is generally attributed to the formation of an oxide film. Passivation is a well-documented phenomenon associated not only with electrode polarization but also with the oxidative properties of the environment. For example, iron dissolves readily in sulfuric acid solutions but hardly dissolves in concentrated sulfuric acid. This factor should also be considered for gold. In gold extraction plants, setting an electrode potential of 400 mV on gold via electrochemical methods is challenging. However, such tests were conducted in [16], where the pulp was subjected to electrochemical treatment on insoluble electrodes. Although the change in gold potential was not monitored, which prevented theoretical justification of the optimal current and potential during pulp treatment, an increase in gold recovery was observed.

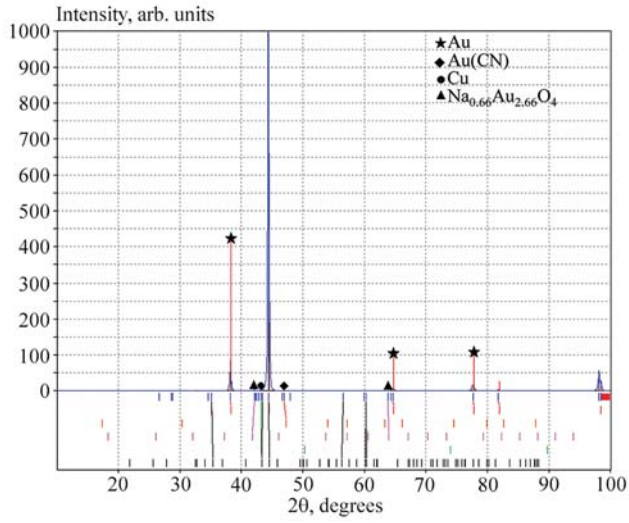

Fig. 9. XRD pattern of the gold sample after passivation and heating at 125 °C

Рис. 9. Дифрактограмма образца золота, подвергнутого пассивации и нагреву при температуре 125 °C

Table 2. **Results of gold leaching in cyanide solutions with electrochemically treated alkali**

Таблица 2. Результаты исследований выщелачивания золота в цианистых растворах с добавкой электрохимически обработанной щелочи

Alkali treatment	Amount, μg/L		Content, mg/L						
	Ag	Au	S	As	Cu	Fe	Mn	Ni	Co
Untreated	0.28	2.2	115.0	0.29	<0.001	<0.05	0.013	0.040	0.023
Electrochemically treated (10 min)	0.31	2.8	130.0	0.34	<0.001	<0.05	0.0043	0.059	0.021

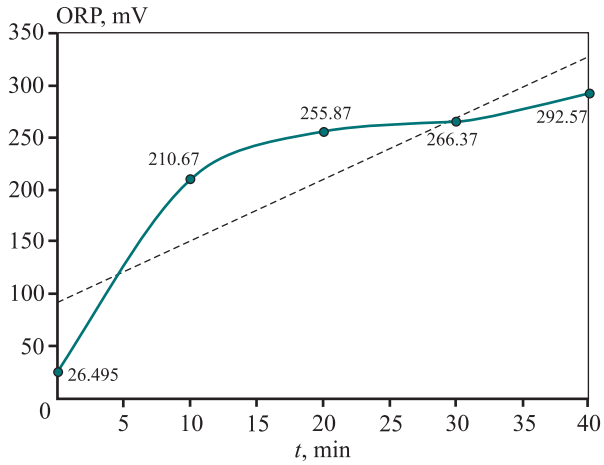

Fig. 10. Dependence of the redox potential of a 0.2 % alkali solution on treatment time on nickel electrodes at a current density of 0.1 A/cm^2

Рис. 10. Зависимость окислительно-восстановительного потенциала раствора 0,2 % щелочи от времени его обработки на никелевых электродах при плотности тока 0,1 А/см^2

Another approach to modifying the gold potential involves the use of oxidants or reductants, which shifts the resulting gold dissolution potential into the passivation and depassivation range. The redox potential (ORP) of the pulp can be increased by introducing oxidants such as oxygen, ozone, or hydrogen peroxide. Electrochemical treatment of reagents, such as an alkali solution, can also increase the ORP. Using such treated alkali in cyanide leaching enhances gold recovery. Laboratory studies on the electrochemical treatment of alkali in an electrolyzer demonstrated the potential for increasing ORP [28]. The dependence of ORP on treatment time is shown in Fig. 10.

Electrochemical treatment of alkali at optimal current and potential values for 10 minutes increases the ORP by a factor of 8.

Table 2 presents the results of gold leaching from refractory ores in cyanide solutions with the addition of electrochemically treated alkali [28].

Table 2 demonstrates that the application of electrochemically treated alkali results in an 18 % and 15 % increase in the extraction of gold and silver into the solution, respectively. Thus, to optimize the gold leaching process at extraction facilities, it is crucial to systematically monitor the electrode potential of gold and regulate it through the addition of oxidizing or reducing agents, or by employing electrochemical treatment of the pulp or reagents.

Conclusion

The cyclic voltammetric measurements on a gold electrode in cyanide solutions at varying oxygen concentrations revealed the relationship between passivation current and potential with sodium cyanide concentration. It was found that increasing the electrode potential leads to a rise in current, and upon reaching the passivation potential, a passive film forms. This results in a significant decrease in current and, consequently, a reduction in gold dissolution. The thickness of the passive film, calculated based on the charge passed during CV measurements, was determined to be 0.007 μm. *X*-ray diffraction analysis of the gold sample's surface indicated that after heating to 125°C, the passive film had the crystallochemical formula $Na_{0,66}Au_{2,66}O_4$. This film likely forms when a gold hydroxide passive film of the type nNa(OH)mAu(OH)$_3$, which is amorphous and undetectable via diffraction, is subjected to heating. The study highlights the potential for enhancing gold recovery from refractory ores through the use of electrochemically treated alkali.

References

1. Leonov S.B., Bubeev P.P., Elshin V.V. Dissolution peculiarities of gold in alkaline oxygen-bearing sodium cyanide solutions. In: *Proc. 5th Southern Hemi-Sphere Meeting Technology.* Buenos Aires, Argentina, 1997. P. 205.

2. Baranov A.N., Elshin V.V., Kolodin A.A. Electrochemical studies of gold dissolution in cyanide solutions at various oxygen concentrations. *Theory and Process Engineering of Metallurgical Production*. 2023;(1):11—17. (In Russ.).
Баранов А.Н., Елшин В.В., Колодин А.А. Электрохимические исследования растворения золота в цианистых растворах при различных концентрациях кислорода. *Теория и технология металлургического производства*. 2023;(1):11—17.
3. Elshin V.V., Kolodin A.A. Optimal control of the gold dissolution process in the gold ore grinding cycle. *Automation in Industry*. 2023;(6):8—13. (In Russ.).
https://doi.org/10.25728/avtprom.2023.06.03
Елшин В.В., Колодин А.А. Оптимальное управление процессом растворения золота в цикле измельчения золотосодержащих руд. *Автоматизация в промышленности*. 2023;(6):8—13.
https://doi.org/10.25728/avtprom.2023.06.03
4. Aleksandrov A.L., Baranov A.N. Corrosion studies of the behavior of gold in cyanide solutions. In: *Processing of natural and man-made raw materials*. Irkutsk: INRTU, 2017. P. 72–75. (In Russ.).
Александров А.Л., Баранов А.Н. Коррозионные исследования поведения золота в цианистых растворах. В сб.: *Переработка природного и техногенного сырья*. Иркутск: Изд-во ИРНИТУ, 2017. С. 72—75.
5. Bastidas D.M. Corrosion and protection of metals. *Metals*. 2020;10(4):458. https://doi.org/10.3390/met10040458
6. Azizi A., Petre C.F., Olsen C., Larachi F. Electrochemical behavior of gold cyanidation in the presence of a sulfide-rich industrial ore versus its major constitutive sulfide minerals. *Hydrometallurgy*. 2010;101:108—119.
https://doi.org/10.1016/j.hydromet.2009.12.004
7. Frankenthal R.P., Thompson D.E. The anodic behavior of gold in sulfuric acid solutions. Effect of chloride and electrode potential. *Journal of the Electrochemical Society*. 1976;123(66):799.
8. Nguyen V.Ch., Astafeva N.A., Balanovsky A.E., Baranov A.N. Study of corrosion resistance of doped surface layer with CuSn—Cr_xC_y composition after plasma hardening. *Uprochnyayushchie tekhnologii i pokrytiya*. 2021;17(5):215—220. (In Russ.).
Нгуен В.Ч., Астафьева Н.А., Балановский А.Е., Баранов А.Н. Исследование коррозионной стойкости легированного поверхностного слоя составом CuSn—Cr_xC_y после плазменного упрочнения. *Упрочняющие технологии и покрытия*. 2021;17(5):215—220.
9. Rybalka K.V., Beketaeva L.A., Davydov A.D. Estimation of AISI 1016 steel corrosion rate by polarization curves analysis and ohmic resistance measurement. *Russian Journal of Electrochemistry*. 2021;57(1):19—24. (In Russ.).
https://doi.org/10.31857/S0424857021010096
Рыбалка К.В., Бекетаева Л.А., Давыдов А.Д. Оценка скорости коррозии стали AISI 1016 анализом поляризационных кривых и методом измерения омического сопротивления. *Электрохимия*. 2021;57(1):19—24.
https://doi.org/10.31857/S0424857021010096
10. Beketaeva L.A., Rybalka K.V., Davydov A.D. Estimation of corrosion rate of cobalt-chromium alloy Starbond-CoS in NaCl solution. *Russian Journal of Electrochemistry*. 2021;57(5):309—315. (In Russ.).
https://doi.org/10.31857/S0424857021040034
Бекетаева Л.А., Рыбалка К.В., Давыдов А.Д. Оценка скорости коррозии кобальт-хромового сплава Starbond-CoS в растворе NaCl. *Электрохимия*. 2021;57(5):309—315.
https://doi.org/10.31857/S0424857021040034
11. Liu M., Lao J., Wang H., Su Z., Liu J., Wen L., Yin Z., Luo K., Peng H. Electrochemical determination of tyrosine on glassy carbon electrode modified with graphene composite and gold nanoparticles. *Russian Journal of Electrochemistry*. 2021;57(1):47—58. (In Russ.).
https://doi.org/10.31857/S0424857020110067
Лиу М., Лао Ж., Ван Х., Су З., Лиу Ж., Вен Л., Йин З., Луо К., Пен Х. Электрохимическое определение тирозина на стеклоуглеродном электроде, модифицированном композитом графена и наночастицами золота. *Электрохимия*. 2021;57(1):47—58.
https://doi.org/10.31857/S0424857020110067
12. Strizhko L.S., Bobozoda Sh.K., Novakovskaya A.O., Boboev I.R. Process control and prediction of raw material leaching using a hydroacoustic emitter. *Systems. Methods. Technologies*. 2014;(4):115—122. (In Russ.).
Стрижко Л.С., Бобозода Ш.К., Новаковская А.О., Бобоев И.Р. Управление процессом и прогнозирование выщелачивания сырья с применением гидроакустического излучателя. *Системы. Методы. Технологии*. 2014;(4):115—122.
13. Elshin V.V., Kolodin A.A., Ovsyukov A.E., Malchikhin A.S. Features of cyanide leaching of gold in the grinding cycle. *Metallurg*. 2013;(7):86—90. (In Russ.).
Елшин В.В., Колодин А.А., Овсюков А.Е. Мальчихин А.С. Особенности цианистого выщелачивания золота в цикле измельчения. *Металлург*. 2013;(7):86—90.
14. Conway M.H., Gale D.C. Sulfur's impact on the size of pressure oxidation autoclaves. *The Journal of the Minerals, Metals & Materials Society*. 1990;42:19—22.
https://doi.org/10.1007/BF03221072
15. Mason P.G. Energy requirements for the pressure oxidation of gold-bearing sulfudes. *The Journal of the Minerals, Metals & Materials Society*. 1990;42(9):15—18.
16. Lavrov A.Yu. The effectiveness rise of developing ore deposits on the basis of innovative geoecological technologies with photo-electrochemical components' activity of technological systems. *Vestnik Zabaikal'skogo Gosudarstvennogo Universiteta*. 2013;(2):31—37. (In Russ.).

Лавров А.Ю. Повышение эффективности освоения рудных месторождений на основе использования инновационных геотехнологий с фотоэлектрохимической активацией компонентов технологических систем. *Вестник Забайкальского государственного университета*. 2013;(2):31—37.

17. Bellec S., Hodouin D., Bazin C., Khalesi M.R., Duchesne C. Modelling and simulation of gold ore leaching. In: *World Gold Conference 2009*. The Southern African Institute of Mining and Metallurgy, 2009. P. 51—59.
18. Nikoloski A.N., Nicol M.J. The electrochemistry of the leaching reactions in the Caron process. II. Cathodic processes. *Hydrometallurgy*. 2010;(105):54—59.
19. Robertson S., Jeffrey M., Zhang H., Ho E. An introductory electrochemical approach to studying hydrometallurgical reactions. *Metallurgical and Materials Transactions B*. 2005;36:313—325.
20. Shchadov I.M., Filippova E.V. Prospects for the use of new environmental protection technology in the processing of gold-bearing technogenic formations. *Ecology and Industry of Russia*. 2017;21(12):24—27. (In Russ.).
https://doi.org/10.18412/1816-0395-2017-12-24-27
Щадов И.М., Филиппова Е.В. Перспективы применения новой экологозащитной технологии при переработке золотосодержащих техногенных образований. *Экология и промышленность России*. 2017;21(12):24—27.
https://doi.org/10.18412/1816-0395-2017-12-24-27
21. Filippova E.V. New integrated technology for processing industrial wastes which allows to increase ecological safety. *Systems. Methods. Technologies*. 2016;(3):192—197. (In Russ.).
https://doi.org/10.18324/2077-5415-2016-3-192-197
Филиппова Е.В. Новая комплексная технология отработки техногенных отходов, позволяющая повысить экологическую безопасность. *Системы. Методы. Технологии*. 2016;(3):192—197.
https://doi.org/10.18324/2077-5415-2016-3-192-197
22. Syed S. Recovery of gold from secondary sources. *Hydrometallurgy*. 2012;115:31—51.
23. Baranov A.N. Corrosion and protection of metals. Irkutsk: INRTU, 2015. 178 p. (In Russ.).
Баранов А.Н. Коррозия и защита металлов: Учеб. пос. Иркутск: ИРНИТУ, 2015. 178 с.
24. Chemist's handbook. 2 nd ed. Vol. 3. Moscow: Khimya, 1964, 1025 p. (In Russ.).
Справочник химика. 2-е изд. Т. 3. М.: Химия, 1964. 1025 с.
25. Chemical encyclopedia. Vol. 2. Ed. I.A. Kiuyants. Moscow: Sovetskaya Entsiklopediya, 1990. 617 p. (In Russ.).
Химическая энциклопедия в 5 т. Т. 2. Под ред. И.А. Киуянц. М.: Советская энциклопедия, 1990. 617 с.
26. Takeno Naoto. Atlas of Eh—pH diagrams (Intercomparison of thermodynamic databases): Geological Survey of Japan Open File Report No. 419. Tsukuba, Ibaraki, Japan: National Institute of Advanced Industrial Science and Technology, Research Center for Deep Geological Environments, 2005.
27. Fenge Lin, David Vera Anaya, Shu Gong, Lim Wei Yap, Yan Lu, Zijun Yong, Wenlong Cheng. Gold nanowire sponge electrochemistry for permeable wearable sweat analysis comfortably and wirelessly. *ACS Sensors*. 2024;9(10):5414—5424.
https://doi.org/10.1021/acssensors.4c01635
28. Sidorov D.S., Baranov A.N. Intensification of leaching of non-ferrous metals using electrochemical treatment of alkali. In: *Prospects for the development of technology for processing hydrocarbon mineral resources:* Materials of the 10th All-Russ. Scientific and Practical Conf. with International Participation (Irkutsk, 22–24 April 2020). Irkutsk: INRTU, 2020. P. 51–53. (In Russ.).
Сидоров Д.С., Баранов А.Н. Интенсификация выщелачивания цветных металлов с применением электрохимической обработки щелочи. В сб.: *Перспективы развития технологии переработки углеводородных минеральных ресурсов:* Материалы X Всерос. науч.-практ. конференции с междунар. участием. Иркутск: ИРНИТУ, 2020. С. 51—53.

Information about the authors

Anatoly N. Baranov – Dr. Sci. (Eng.), Prof., Department of metallurgy of non-ferrous metals, Irkutsk National Research Technical University (INRTU).
https://orcid.org/0000-0001-5336-6522
E-mail: baranov@istu.edu

Viktor V. Elshin – Dr. Sci. (Eng.), Prof., Head of the Department of automation and control, INRTU.
https://orcid.org/0000-0002-04447-4831
E-mail: dean_zvf@.istu.edu

Alexey A. Kolodin – Senior Lecturer, Department of automation and control, INRTU.
https://orcid.org/0000-0003-4451-4014
E-mail: kolodin@istu.edu

Elena V. Filippova – Cand. Sci. (Eng.), Associate Prof., Deputy Head of the Department of assessments, licensing and inspections of nuclear fuel cycle facilities, Federal Service for Environmental, Industrial and Nuclear Supervision.
https://orcid.org/0009-0003-0872-314X
E-mail: filena78@mail.ru

Информация об авторах

Анатолий Никитич Баранов – д.т.н., профессор кафедры металлургии цветных металлов Иркутского национального исследовательского технического университета (ИРНИТУ).
https://orcid.org/0000-0001-5336-6522
E-mail: baranov@istu.edu

Виктор Владимирович Ёлшин – д.т.н., профессор, заведующий кафедрой автоматизации и управления ИРНИТУ.
https://orcid.org/0000-0002-04447-4831
E-mail: dean_zvf@.istu.edu

Алексей Александрович Колодин – ст. преподаватель кафедры автоматизации и управления ИРНИТУ.
https://orcid.org/0000-0003-4451-4014
E-mail: kolodin@istu.edu

Елена Владимировна Филиппова – к.т.н., доцент, зам. начальника отдела оценок, лицензирования и инспекций объектов ядерного топливного цикла Федеральной службы по экологическому, технологическому и атомному надзору.
https://orcid.org/0009-0003-0872-314X
E-mail: filena78@mail.ru

Contribution of the authors

A.N. Baranov – development of the main concept, formulation of the study's goal and objectives, preparation of the manuscript, and formulation of conclusions.

V.V. Elshin – scientific supervision, provision of resources, text revision, and refinement of conclusions.

A.A. Kolodin – calculations, sample testing, and manuscript preparation.

E.V. Filippova – experiment preparation, conducting experiments, manuscript drafting, and conclusion formulation.

Вклад авторов

А.Н. Баранов – формирование основной концепции, постановка цели и задачи исследования, подготовка текста статьи, формулировка выводов.

В.В. Ёлшин – научное руководство, обеспечение ресурсами, корректировка текста статьи, корректировка выводов.

А.А. Колодин – осуществление расчетов, проведение испытаний образцов, подготовка текста статьи.

Е.В. Филиппова – подготовка экспериментов и их проведение, подготовка текста статьи, формулировка выводов.

The article was submitted 20.02.2024, revised 06.09.2024, accepted for publication 19.09.2024

Статья поступила в редакцию 20.02.2024, доработана 06.09.2024, подписана в печать 19.09.2024

FOUNDRY / ЛИТЕЙНОЕ ПРОИЗВОДСТВО

UDC 546.06, 538.91, 539.8
https://doi.org/10.17073/0021-3438-2025-1-27-40

Research article
Научная статья

Production of cast master alloys with high chromium content using centrifugal SHS metallurgy

A.N. Kubanova[1,2], **D.M. Ikornikov**[1], **V.N. Sanin**[1], **D.A. Martynov**[3]

[1] **Merzhanov Institute of Structural Macrokinetics and Materials Science of the Russian Academy of Sciences**
8 Academician Osipyan Str., Chernogolovka, Moscow Region 142432, Russia

[2] **Tula State Pedagogical University n.a. L.N. Tolstoy**
125 Lenin Prosp., Tula 300026, Russia

[3] **LLC "Research, Design and Technology Center"**
4 Bld, 102 Lenin Prosp., Tula 300025, Russia

✉ Anastasiya N. Kubanova (kubanovaan@tsput.ru)

Abstract: Cast master alloys of the Mo–Cr, W–Cr, and Cr–Al systems with high chromium content were produced using the methods of centrifugal SHS metallurgy. A thermodynamic analysis was performed to evaluate the combustion temperature and the equilibrium composition of the reaction products depending on the ratios of the initial components in the mixture. Based on this analysis, optimal compositions were identified for further experimental studies. The effectiveness of functional additives, namely calcium fluoride CaF_2 (fluorspar) and sodium hexafluoroaluminate $Na_3[AlF_6]$ (cryolite), was experimentally confirmed. These additives were shown to lower the melting point of the slag phase (reducing its viscosity), which facilitated phase separation during the production of cast master alloys from refractory metals using centrifugal SHS metallurgy. The experiments demonstrated the need to introduce excess amounts of MoO_3 and WO_3 during the production of Mo–Cr and W–Cr master alloys, respectively, due to incomplete reduction of molybdenum and tungsten from their oxides. Microstructural analysis of the obtained master alloys revealed a dendritic structure, which is typical for cast materials. EDS microanalysis showed that the chemical compositions of all synthesized alloys closely matched their calculated and target compositions. Composition analysis at different locations within the ingots revealed no significant variations in composition. *X*-ray phase analysis confirmed the presence of solid solution phases formed from the target elements. The results of inductively coupled plasma mass spectrometry (ICP-MS) confirmed that the chemical compositions of the synthesized Cr–W, Cr–Mo, and Cr–Al alloys fully comply with the permissible concentrations of both target elements and impurities.

Keywords: master alloy, chromium, molybdenum, tungsten, aluminum, self-propagating high-temperature synthesis, centrifugal SHS metallurgy.

For citation: Kubanova A.N., Ikornikov D.M., Sanin V.N., Martynov D.A. Production of cast master alloys with high chromium content using centrifugal SHS metallurgy. *Izvestiya. Non-Ferrous Metallurgy.* 2025;31(1):27–40. https://doi.org/10.17073/0021-3438-2025-1-27-40

Получение литых лигатур с высоким содержанием Cr методами центробежной СВС-металлургии

А.Н. Кубанова[1,2], **Д.М. Икорников**[1], **В.Н. Санин**[1], **Д.А. Мартынов**[3]

[1] **Институт структурной макрокинетики и проблем материаловедения им. А.Г. Мержанова РАН**
Россия, 142432, Московская обл., г. Черноголовка, ул. Академика Осипьяна, 8

[2] **Тульский государственный педагогический университет им. Л.Н. Толстого**
Россия, 300026, г. Тула, пр-т Ленина, 125

[3] **ООО «Центр исследований, дизайна и технологий»**
Россия, 300025, г. Тула, пр-т Ленина, 102, к. 4

✉ Анастасия Николаевна Кубанова (kubanovaan@tsput.ru)

Аннотация: Методами центробежной СВС-металлургии получены литые лигатуры Mo–Cr, W–Cr и Cr–Al с высоким содержанием Cr. Выполнен термодинамический анализ температуры горения и состава равновесных продуктов в зависимости от соотно-

шения исходных компонентов смеси. На основе анализа определены оптимальные составы для проведения экспериментальных исследований. Экспериментально установлена эффективность применения функциональных добавок CaF_2 (плавиковый шпат) и гексафтороалюмината натрия $Na_3[AlF_6]$ (криолит) с целью снижения температуры плавления шлаковой фазы (уменьшения ее вязкости) и облегчения процесса фазоразделения при производстве литых лигатур из тугоплавких металлов методом центробежной СВС-металлургии. Анализ экспериментов показал необходимость ввода избыточного содержания MoO_3 и WO_3 при производстве лигатур Mo–Cr и W–Cr соответственно ввиду неполного восстановления Mo и W из их оксидов. Анализ микроструктуры полученных лигатур свидетельствует о наличии дендритной структуры, что типично для литого состояния сплавов. По результатам микроанализов (EDS), все полученные лигатуры близки к своим расчетным и целевым значениям химических составов. Микроанализ состава разных участков слитков не выявил заметных различий по составу сплава. Проведенные рентгенофазовые анализы синтезируемых лигатур показали наличие пиков твердых растворов, сформированных на основе соответствующих целевых элементов. Анализ данных химического состава, полученного с помощью метода масс-спектроскопии с индуктивно-связанной плазмой, для синтезированных сплавов систем Cr–W, Cr–Mo и Cr–Al выявил их полное соответствие значениям по допустимым концентрациям как целевых элементов, так и примесных компонентов.

Ключевые слова: лигатура, хром, молибден, вольфрам, алюминий, самораспространяющийся высокотемпературный синтез, центробежная СВС-металлургия.

Для цитирования: Кубанова А.Н., Икорников Д.М., Санин В.Н., Мартынов Д.А. Получение литых лигатур с высоким содержанием Cr методами центробежной СВС-металлургии. *Известия вузов. Цветная металлургия*. 2025;31(1):27–40.
https://doi.org/10.17073/0021-3438-2025-1-27-40

Introduction

Alloying technologies for modern industrial alloys have become widely used across various industries. The optimal selection of alloying component compositions and alloying methods enables the resolution of complex challenges in the design and manufacturing of diverse products, achieving the desired combination of performance characteristics [1; 2]. The introduction of master alloys with a specified composition allows for precise control of alloying element concentrations and ensures the efficient introduction of easily oxidizable or volatile components into the melt at high temperatures, as these components are supplied in a stable cast (prealloyed) form.

Currently, the primary industrial method for producing most master alloys involves the direct melting of metals using electrometallurgical techniques. This method is associated with high energy and material costs, largely due to the need for high-purity starting materials. Moreover, when using components with significantly different melting points, losses of volatile elements increase, which negatively affects both the quality of the master alloy and the final production cost of industrial alloys.

Cast chromium-based master alloys of various compositions (Cr—Al, Cr—Cu, Cr—Fe, Cr—Ti, Cr—V—Al, etc.) have already become well-established in the metallurgical industry as alloying additives in the production of high-alloy steels, heat-resistant nickel alloys, aluminum alloys, and others [3; 4]. Since chromium has a melting point of approximately 1900 °C, it cannot be melted in a vacuum due to sublimation (direct transition from solid to gas) [3]. Therefore, the production of high-chromium master alloys requires melting the starting metals in an inert gas atmosphere at pressures exceeding 760 mmHg, which significantly complicates the technological process.

As a result, the production of chromium-containing master alloys, where components have significantly different melting points, presents several challenges when using conventional metallurgical methods [5]. The large difference in melting points between aluminum and chromium makes the production of Cr—Al master alloys particularly costly due to the significant evaporation of aluminum during melting, or it necessitates the use of multi-stage powder metallurgy techniques requiring extremely pure starting materials [5]. The high melting points of tungsten, molybdenum, and chromium make it impossible to produce these alloys using traditional melting of charge materials. Due to this characteristic, the conventional production of Mo—Cr and W—Cr alloys relies on two main technological approaches:

— expensive vacuum arc and electron beam remelting processes, which result in significant material losses due to evaporation at high temperatures;

— powder metallurgy methods, which involve multi-stage pressing of high-purity metal powders, usually followed by sintering in inert or reactive gas atmospheres (nitrogen, argon, or hydrogen).

Therefore, there is a clear need to improve the energy efficiency of master alloy production for systems with significantly different melting points, while reducing

production costs without compromising material properties and quality.

One of the relatively recent methods for producing cast and powder materials based on metals and their compounds is Self-Propagating High-Temperature Synthesis (SHS) [6; 7], which has already been applied in the production of master alloys used to develop new high-strength structural alloys, including those intended for service in Arctic conditions [8—10]. One important technological branch of SHS processes is centrifugal SHS metallurgy [11—13], which combines SHS with metallothermy [14]. The key feature of SHS metallurgy lies in conducting highly exothermic reduction reactions while applying additional physical forces (centrifugal forces), which enables the production of high-quality cast combustion products. This approach also serves as an additional tool for controlling the formation of composition and structure in the resulting cast SHS materials [11; 15; 16—18].

The objective of this study was to develop the chemical and technological foundations for the synthesis of high-chromium alloys (Cr—Mo, Cr—W, Cr—Al) by means of centrifugal SHS metallurgy.

Research materials and methods

The process used to produce the alloys under investigation is based on an exothermic reaction between the oxides of the target metals (Cr, W, and Mo) and aluminum (acting as a metallic reducing agent), which proceeds in a self-propagating combustion (SHS) mode. This reaction is accompanied by the melting (casting) of the final products, followed by their phase separation under the influence of centrifugal forces generated in the centrifugal SHS setup.

The overall chemical equations describing the synthesis of the studied alloys can be represented as follows:

$$Cr_2O_3 + MoO_3 + \alpha Al + FA \rightarrow \rightarrow Cr—Mo\ (Al) + Al_2O_3, \quad (1)$$

$$Cr_2O_3 + WO_3 + \alpha Al + FA \rightarrow \rightarrow Cr—W\ (Al) + Al_2O_3, \quad (2)$$

$$[Cr_2O_3\ /CrO_3] + \alpha Al + FA \rightarrow \rightarrow Cr—Al + Al_2O_3, \quad (3)$$

where FA denotes a functional additive based on fluorite CaF_2 (fluorspar) and cryolite $Na_3[AlF_6]$ (sodium hexafluoroaluminate).

Table 1 presents the grades and selected characteristics of the raw materials reagents used in the study. The functional additives were introduced into the reaction mixture as a combination of these two compounds (cryolite and fluorspar) to facilitate phase separation of the reaction products.

The target compositions of the Mo—Cr, W—Cr, and Cr—Al master alloys were selected based on actual chemical compositions used at leading metallurgical enterprises in Russia (Table 2). The permissible concentration ranges for the elements in this group of alloys were provided by a potential end user of the research results — Electrostal Metallurgical Plant JSC (Electrostal, Moscow Region).

Table 1. **Selected characteristics of raw materials and functional additives**

Таблица 1. Некоторые характеристики исходных веществ и ФД

Material	Grade	Standard (GOST/TU)	Particle size, μm	Purity, %
Main components for synthesis				
Cr_2O_3	Ch	TU 6-09-4272-84	<20	99.00
WO_3	ChDA	TU 48-4205-122-2019	<20	99.90
MoO_3	ChDA	TU 6-09-4471-77	<50	99.00
Al	PA-4	GOST 6058-73	<140	98.00
Functional additives (FA)				
CaO	Pure	GOST 8677-76	<150	96.0
$Na_3[AlF_6]$	KP	GOST 10561-80	<150	97.0
CaF_2	FF-97	GOST 29219-91	<100	97.2

Table 2. **Permissible element concentrations in the chemical compositions of the studied alloys**

Таблица 2. Допустимые концентрации элементов по химическому составу для исследуемых сплавов

Element, wt. %	Alloy system		
	Cr–W (Al)	Cr–Mo (Al)	Cr–Al
Cr	Balance	Balance	Balance
Mo	1.0	50–65	–
W	40–60	–	–
Al	–	–	10–25
Impurities, not more than			
Al	5.0	5.0	–
C	0.05	0.05	0.04
Si	0.3	0.3	0.5
S	0.01	0.01	0.01
P	0.01	0.01	0.01
Fe	1.0	1.0	0.7
Cu	0.05	0.05	0.2
Co	0.1	0.1	–
O	0.04	0.05	0.04
N	0.04	0.04	0.04
Mg	–	–	0.5
Ti	–	–	0.1
Ni	–	–	0.2
Mn	–	–	0.4
Zn	–	–	0.2

Before being introduced into the technological process, all oxide powder components were dried to remove adsorbed moisture in a SNOL-type drying oven (t = = 90 °C, τ = 1 h). After dosing the components to achieve the target alloy composition, the reagents were mixed in an MP4/5.0 planetary ball mill with a drum volume of up to 5 L for 15—20 min, with a ball-to-powder mass ratio of 1:10.

To prepare the reaction mold, a pre-dried (for at least 1 h at 90 °C) refractory mold made of electrolytic corundum (Al_2O_3) produced by NTC Bakor (Shcherbinka, Moscow Region) was used. The mold was placed on a vibration table, where the mixture was loaded and compacted. Depending on the mold volume, the batch weight during different stages of the experiments ranged from 0.5 to 2.6 kg.

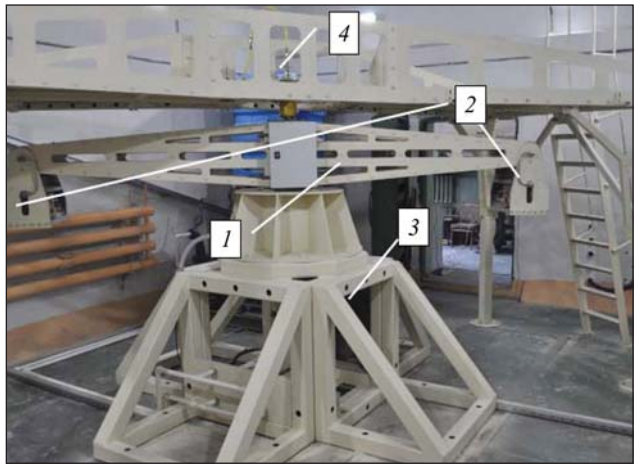

Fig. 1. External view of the centrifugal setup for producing cast materials using centrifugal SHS casting

1 – rotor of the centrifugal setup, ***2*** – reaction chamber, ***3*** – electric drive, ***4*** – laser initiation system

Рис. 1. Внешний вид центробежной установки для получения литых материалов методом центробежного СВС-литья

1 – ротор центробежной установки, ***2*** – реакционный блок, ***3*** – электропривод, ***4*** – система подачи лазерного инициирования

The prepared mold containing the mixture was installed on the rotor of the centrifugal SHS setup, an external view of which is shown in Fig. 1. The design of the SHS setup is proprietary [6; 7; 13] and includes the following systems: laser initiation; automatic rotor speed control to maintain the specified overload level (g); water cooling of the reaction (melting) chamber; and video monitoring with real-time recording of the combustion process.

The synthesis of the target alloy was carried out in an open-type reaction mold at atmospheric pressure and a steady rotor speed corresponding to an overload of 55 ± 5g. The combustion temperature exceeded 3000 K, which was higher than the melting point of the final products. After the combustion process was completed, phase separation and crystallization of the reaction products took place under the action of centrifugal forces and due to the mutual immiscibility of the phases. Cooling of the reaction mass was carried out by forced cooling through a water-cooled jacket of the reaction chamber. The combustion products formed an ingot consisting of two distinct layers with a clearly defined interface: the upper (slag) layer composed of corundum, and the lower layer containing the target alloy.

Analysis of the alloys. The quantitative analysis of major elements and impurities was performed using an iCAP 6300 inductively coupled plasma atomic emission spectrometer (Thermo Fisher Scientific, USA), equipped with a double-focusing Nier—Johnson geometry mass analyzer. Carbon and sulfur contents were measured using an SC844 analyzer (LECO, USA), while oxygen, nitrogen, and hydrogen contents were determined using an ONH836 analyzer (LECO, USA).

The phase composition was analyzed by *X*-ray diffraction (XRD) using a DRON 3M diffractometer (ARL X'TRA, Switzerland). Microstructural studies were carried out using a Zeiss Ultra Plus Field Emission Scanning Electron Microscope (Ultra 55 platform, Zeiss, Germany).

Thermodynamic analysis. To estimate the maximum achievable adiabatic synthesis temperature for different initial component ratios, a preliminary thermodynamic analysis was performed using the Thermo software package. Functional additives were excluded from the thermodynamic calculations due to their low concentrations. The calculations provided the equilibrium composition of both condensed and gaseous products, along with the adiabatic reaction temperature.

Results and discussion

The thermodynamic calculation results obtained using the Thermo software package are shown in Fig. 2—4.

Analysis of the obtained data, including adiabatic temperature and component concentrations under conditions of thermodynamic equilibrium, showed that in the Mo—Cr system, the combustion temperature of the exothermic mixture can reach up to 3500 °C. It should be noted that in the molybdenum concentration range of 50—65 wt. %, the temperature ranges from 2800 to 3200 °C, which exceeds the melting points of the components. These conditions are sufficient for obtaining cast materials during the combustion of the investigated mixtures, with the concentration of gaseous products remaining relatively low (less than 0.1 wt. %).

Analysis of the data for the W—Cr system revealed a similar qualitative trend. In the tungsten concentration range of 40—60 wt. %, the combustion temperature exceeds 3000 °C, which ensures complete dissolution of W in molten Cr. At the same time, the content of gaseous products is negligible (less than 0.05 wt. %).

Based on these results, it can be concluded that for the production of cast materials in the studied Mo—Cr and W—Cr systems, at molybdenum oxide (αMoO_3) and tungsten oxide (αWO_3) concentrations exceeding $\alpha = 0.3$, there are no thermodynamic barriers to synthesis. In other words, the calculated combustion temperatures are sufficient to produce cast materials with the target compositions.

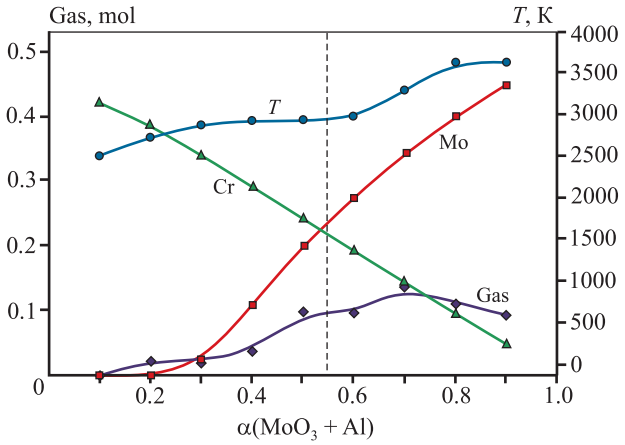

Fig. 2. Results of thermodynamic analysis for the Cr–Mo system at varying composition ratios $(1 - \alpha)(Cr_2O_3 + Al) + \alpha(MoO_3 + Al)$

Рис. 2. Результаты термодинамического анализа системы Cr–Mo при варьировании соотношения составов $(1 - \alpha)(Cr_2O_3 + Al) + \alpha(MoO_3 + Al)$

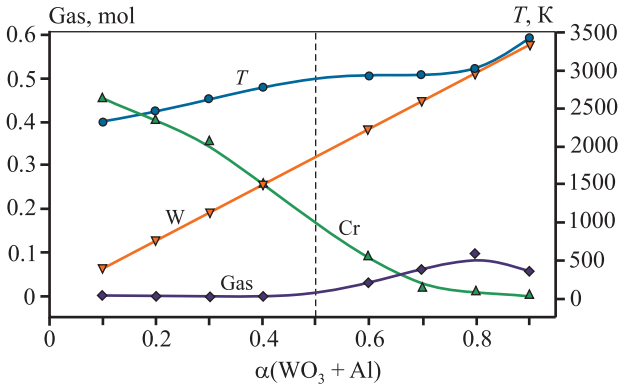

Fig. 3. Results of thermodynamic analysis for the Cr–Mo system at varying composition ratios $(1 - \alpha)(Cr_2O_3 + Al) + \alpha(WO_3 + Al)$

Рис. 3. Результаты термодинамического анализа системы Cr–W при варьировании соотношения составов $(1 - \alpha)(Cr_2O_3 + Al) + \alpha(WO_3 + Al)$

The thermodynamic analysis of the Al—Cr system was carried out considering the use of either chromium (VI) oxide (Fig. 4, *a*) or chromium (III) oxide (Fig. 4, *b*) as the initial component. The results showed that within the target concentration range of 10—25 wt. % Al in the master alloy, the adiabatic combustion temperature reaches approximately 2300 °C for the Cr_2O_3—Al system and around 3000 °C for the CrO_3—Al system. Based on these results, and considering the melting point of chromium, it was decided to use a combined chromium oxide mixture [Cr_2O_3 + CrO_3] in a 50/50 ratio during synthesis.

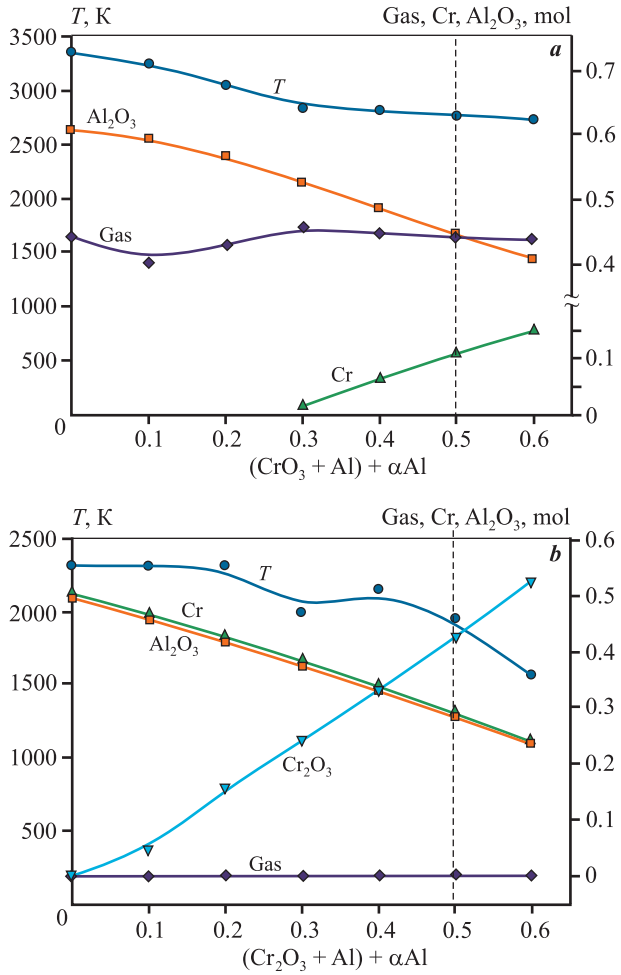

Fig. 4. Results of thermodynamic analysis for the Al–Cr system performed in the "Thermo" software package, considering the use of CrO_3 (***a***) and Cr_2O_3 (***b***)

Рис. 4. Результаты термодинамического анализа системы Al–Cr в программном пакете «Thermo» с учетом применения CrO_3 (***a***) и Cr_2O_3 (***b***)

This approach was justified by the resulting increase in adiabatic temperature to approximately 2500—2700 °C, as well as the formation of pure chromium (complete reduction of chromium oxide) in the reaction products.

When developing the charge compositions and selecting process parameters to obtain alloys with the target compositions, it is essential to have general data on the interaction characteristics of the studied materials as a function of temperature under equilibrium conditions. Such data can be extracted from the analysis of phase diagrams. The phase diagrams used in this study are provided in sources [19—24].

Analysis of the Mo—Cr system [19; 20; 22] showed that both components exhibit unlimited mutual solubility, which will naturally contribute to a more uniform distribution of components within the ingot during synthesis.

A similar interaction pattern was found for the W—Cr system [23], where both components also have unlimited mutual solubility. It should be noted that within the specified component ratio range, the melting point is approximately 2100 °C.

Analysis of the Al—Cr system [24] showed that the general interaction characteristics of the main components favor the formation of various phases (AlCr, $AlCr_2$, αAl_8Cr_5, βAl_8Cr_5, etc.) during cooling and crystallization. It is important to emphasize that within the specified composition range, the melting point is ~1650÷1700 °C.

Effect of FAs on phase separation efficiency

The effect of functional additives on the formation of the sample's macrostructure and the efficiency of phase separation was evaluated using the Cr—Mo alloy system as an example. Two compounds were introduced into the mixture as functional additives: fluorite CaF_2 (fluorspar) and sodium hexafluoroaluminate $Na_3[AlF_6]$ (cryolite). The primary role of these additives is to lower the melting point of the slag phase and, consequently, to reduce its viscosity. This creates favorable conditions for more complete phase separation between the metallic (target) phase and the oxide (slag) phase, ensuring the formation of a clearer phase boundary.

Fig. 5 shows the external appearance of a Cr—Mo alloy sample produced without the use of functional additives in the initial composition. It can be seen that the phase separation process was incomplete, as no distinct phase boundary is observed across the entire cross-section of the ingot. This results in reduced recovery of the target product and significantly complicates phase separation after crystallization and cooling. The loss of the target alloy can reach up to 25 wt. %, which is unacceptable. According to the literature [25; 26], the introduction of calcium oxide (CaO) into an aluminum oxide melt leads to a reduction in melting temperature. Analysis of the CaO—Al_2O_3 phase diagram indicates that even a minor CaO addition (less than 10 %) reduces the melting temperature by approximately 150 °C.

Both the combined FA and a specified amount of calcium fluoride (CaF_2) mixture were used in the experiments. This made it possible to lower the melting temperature of the slag phase by 100—120 °C and to solve two additional problems. At temperatures above its melting point (CaF_2 melts at 1360 °C), this compound decomposes into Ca and F. Each of these elements plays a distinct role when entering the high-temperature melt of combustion products. Fluorine, being highly reactive, interacts with harmful impurities, helping to remove

Fig. 5. Cr–Mo alloy sample produced without functional additives

a – external view of the sample (cross-sectional fracture) after combustion of the mixture); ***b*** – ceramic mold

Рис. 5. Полученный образец системы Cr–Mo без использования функциональной добавки

a – внешний вид образца (поперечный скол) после сжигания смеси; ***b*** – керамическая форма

Fig. 6. External view of the macrostructure of ingots (mass 1–1.45 kg) synthesized for the Cr–Mo (Al) (***a***), Cr–W (Al) (***b***), and Cr–Al (***c***) alloys

Рис. 6. Внешний вид макроструктуры слитков (массой 1–1,45 кг) синтезированных сплавов Cr–Mo (Al) (***a***), Cr–W (Al) (***b***) и Cr–Al (***c***)

them. In particular, fluorine reacts with sulfur according to the reaction $S + 3F_2 \rightarrow SF_6$ forming a colorless, odorless gas. The beneficial effect of elemental calcium is twofold. In the initial stage, calcium acts as a getter in the melt and actively participates in the deoxidation reaction ($Ca + O \rightarrow CaO$) of the melt by reacting with residual (dissolved) oxygen in the alloy, thereby reducing its concentration. In the second stage, calcium oxide (CaO), acting as part of the slag phase, floats to the surface and interacts with molten aluminum oxide, reducing the melting point of the slag phase. This increases the time the melt remains in the liquid state, thus improving the efficiency of phase separation between the metallic and oxide layers.

The phase diagram of the Na_3AlF_6—Al_2O_3 system is relatively simple, with a low eutectic temperature of 961 °C, which further promotes more complete phase separation of the reaction products.

Therefore, the introduction of FAs positively influences phase separation, ensuring a sharply defined boundary, which simplifies the separation of phases after minimal mechanical impact (e.g., tapping).

The optimized concentrations of the mixture components and FA (total content in the initial mixture) are not disclosed, as they constitute proprietary know-how.

All subsequent synthesis experiments for the studied alloys were performed with FA added. The external appearance of the ingot macrostructures obtained for each of the studied alloy systems is shown in Fig. 6.

Cr–Mo (Al) system

The synthesis reaction for this alloy was calculated to achieve the target composition of Cr40Mo56Al4 (wt. %). It is worth noting that the calculated concentrations of the main components for the studied alloys fit well within the permissible ranges specified in Table 2.

As established during the preliminary stage of the study, the ingots produced in the Cr—Mo (Al) alloy initially showed a slight (1—2 %) deficiency in molybdenum content, indicating incomplete reduction. Consi-

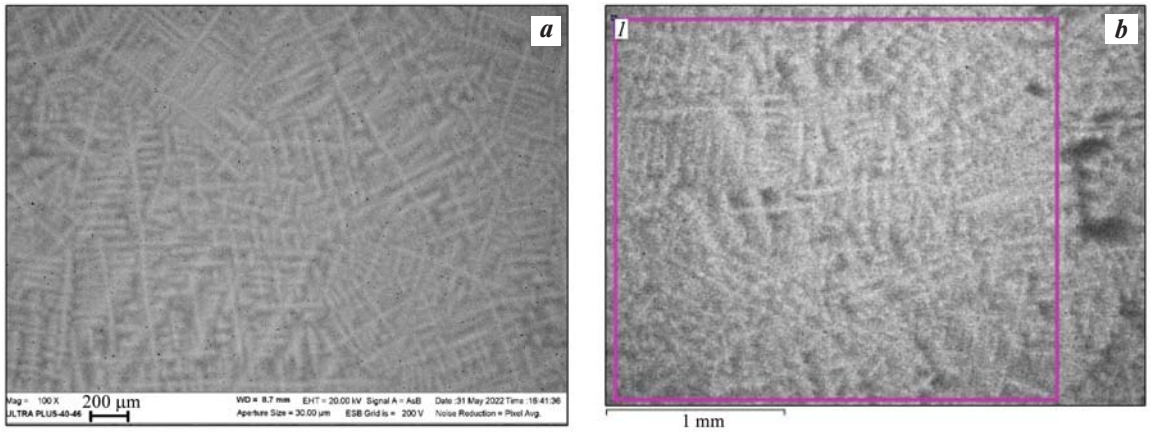

c

Spectrum	Content, wt. %			
	Al	Cr	Mo	Σ
1	3.38	38.00	58.62	100.00

Fig. 7. Microstructure (***a***, ***b***) and EDS composition analysis (***b***, ***c***) of the Cr–Mo (Al) alloy sample (from a polished cross-section)

Рис. 7. Микроструктура (***a***, ***b***) и микроанализ (EDS) состава (***b***, ***c***) полученного образца сплава на основе системы Cr–Mo (Al) (со шлифа)

dering this, a minor adjustment was made in the following experiments, slightly increasing the proportion of molybdenum oxide in the initial mixture compared to the calculated composition.

Fig. 7 presents micrographs of the synthesized cast Cr—Mo (Al) alloy produced under optimized conditions (55*g*, batch weight 1.7 kg, with functional additives). Structural analysis of the obtained material showed a dendritic structure (Fig. 7, *a*), which is characteristic of cast alloys. According to EDS microanalysis performed on a polished cross-section (Fig. 7, *b*), the alloy composition closely matches the calculated target composition (Fig. 7, *c*) in terms of the concentrations of the key elements (see Table 2). This confirms that the selected ratios of the initial components in the mixture were appropriate. Microanalysis of the composition at different locations (top, bottom, and center) of the Cr—Mo (Al) alloy ingot revealed no significant variation in elemental composition across the ingot.

X-ray phase analysis of the synthesized alloy detected only peaks corresponding to the target alloy (a solid solution of Cr in Mo), as shown in Fig. 8. The main XRD parameters for the obtained Cr—Mo (Al) master alloy were: anode — Cu, start angle — 20°, end angle — 100°, step size = 0.02°, scan speed — 0.5 °/s, maximum count — 2063.

The obtained data indicate that no interaction products were formed between the ceramic mold material and the high-temperature melt of the synthesis products,

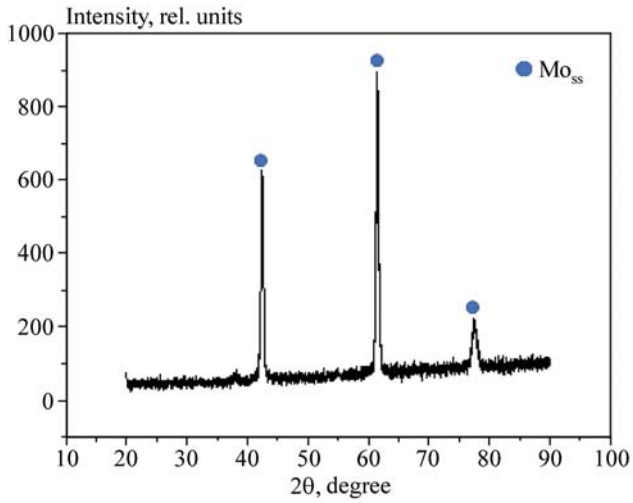

Fig. 8. *X*-ray diffraction analysis of the Cr–Mo (Al) alloy ingot
Mo_{ss} – Mo-based solid solution

Рис. 8. Рентгенофазовый анализ полученного слитка системы Cr–Mo (Al)
Mo_{ss} – твердый раствор на основе Mo

despite the elevated melt temperature. The resulting alloy composition falls within the permissible concentration range specified for the studied alloys (see Table 2).

Cr–W (Al) system

Due to the higher melting point of tungsten, it was decided to slightly reduce the concentration of this refractory component compared to the base composition

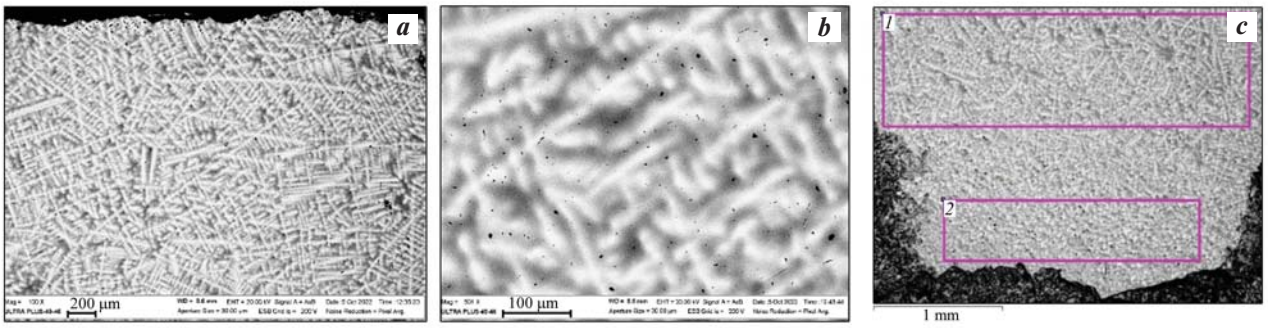

d

Spectrum	Content, wt. %			
	Al	Cr	W	Σ
1	2.91	46.73	50.36	100.00
2	3.85	46.13	50.02	100.00

Fig. 9. Microstructure (***a***, ***b***) and EDS composition analysis (***c***, ***d***) of the Cr–W (Al) alloy sample (from a polished cross-section)

Рис. 9. Микроструктура (***a***, ***b***) и микроанализ (EDS) состава (***c***, ***d***) полученного образца сплава на основе системы Cr–W (Al) (со шлифа)

calculated for the first system (Cr—Mo (Al)). As a result, the Cr43W53Al4 (wt. %) composition was selected as the base composition for the experiments.

Micrographs of the structure and structural components of the synthesized cast Cr—W (Al) alloy samples are shown in Fig. 9, *a*—*c*. Structural analysis confirmed that the obtained alloy also exhibits a well-defined dendritic structure. At higher magnification (Fig. 9, *b*), contrast variations reveal dendritic redistribution of the target alloying elements. The central part of the dendrite arms is enriched in W, while the peripheral region is enriched in Cr. This allowed for detailed point chemical analysis using the INCA Energy 350 XT microanalysis system, installed on the ultra-high-resolution field emission scanning electron microscope. However, this redistribution occurs at the microscale and does not affect the overall quality of the produced alloy.

Microanalysis of the composition at different locations (top, bottom, and center) of the Cr—W (Al) alloy sample showed no significant variations in composition. This is primarily explained by the specific features of SHS metallurgy and the action of centrifugal forces, which promote thorough mixing of the melt components prior to crystallization. The most representative composition data for the obtained alloy are presented in Fig. 9, *c*, *d*. It can be seen that the alloy composition meets the target element concentration requirements (see Table 2), confirming the correct selection of the initial component ratios in the starting mixture.

X-ray phase analysis of the synthesized Cr—W (Al) alloy revealed the presence of peaks corresponding to

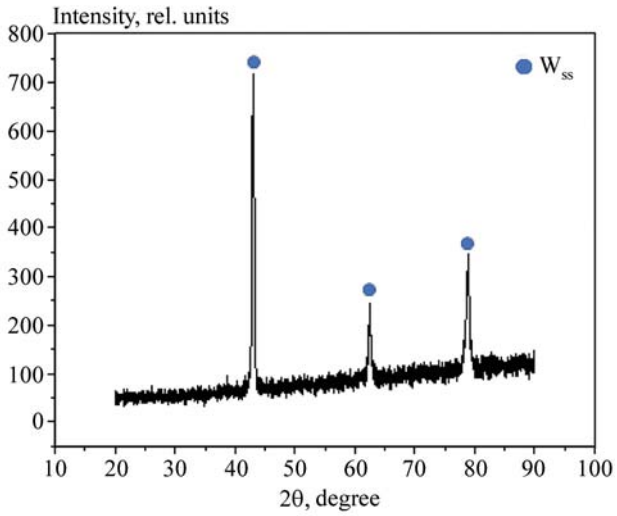

Fig. 10. *X*-ray diffraction analysis of the Cr–W (Al) alloy ingot
W_{ss} – W-based solid solution

Рис. 10. Рентгенофазовый анализ полученного слитка системы Cr–W (Al)
W_{ss} – твердый раствор на основе W

a solid solution formed based on the target elements (a solid solution of Cr in W), as shown in Fig. 10. The main XRD parameters for the Cr—W master alloy were: anode — Cu, start angle — 20°, end angle — 100°, step size — 0.02°, scan speed — 0.5 °/s, maximum count — 1780.

As shown, no unwanted secondary phases were detected in the obtained alloy. Even at this stage of research, it can already be confidently concluded that

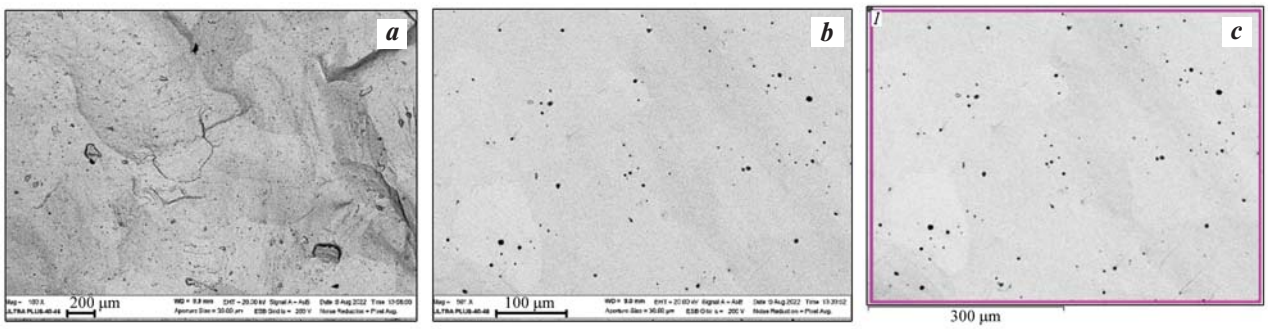

d

Spectrum	Content, wt. %			
	Cr	Al	O	Σ
1	87.71	11.42	0.87	100.00

Fig. 11. Microstructure (***a***, ***b***) and EDS composition analysis (***c***, ***d***) of the Cr–Al alloy sample (from a polished cross-section)

Рис. 11. Микроструктура (***a***, ***b***) и микроанализ (EDS) состава (***c***, ***d***) полученного образца сплава на основе системы Cr–Al (со шлифа)

the use of alundum molds is justified for producing the studied alloys via centrifugal SHS metallurgy.

Cr–Al system

Micrographs of the synthesized cast Cr—Al alloy sample at different magnifications are shown in Fig. 11, *a*, *b*. At higher magnification (Fig. 11, *b*), non-metallic inclusions (slag phase) can be seen in the ingot, which is an expected result at this stage of research (preliminary series of experiments). This is because the reactive mixture mass for this system was insufficient, not exceeding 550 g. During combustion, due to intense heat transfer, the sample cools rapidly, resulting in incomplete phase separation of the synthesis products. This issue is typically resolved by increasing the reactive mixture mass, which is planned for future experiments.

EDS microanalysis performed on the fracture surface (Fig. 11, *c*, *d*) confirms that the alloy composition meets the target element concentration requirements (see Table 2). The residual oxygen content indicates the presence of non-metallic inclusions, resulting from the short "lifetime" of the liquid phase (melt). This limited time prevented the complete reduction of the chromium oxide and did not allow the formed Al_2O_3 to fully transition into the slag phase.

X-ray phase analysis of the synthesized Cr—Al alloy detected only peaks corresponding to the target alloy formed from the main elements (Fig. 12). The main XRD parameters for the Cr—Al master alloy were: anode — Cu, start angle — 20°, end angle — 100°, step size — 0.02°, scan speed — 0.5 °/s, maximum count — 1570.

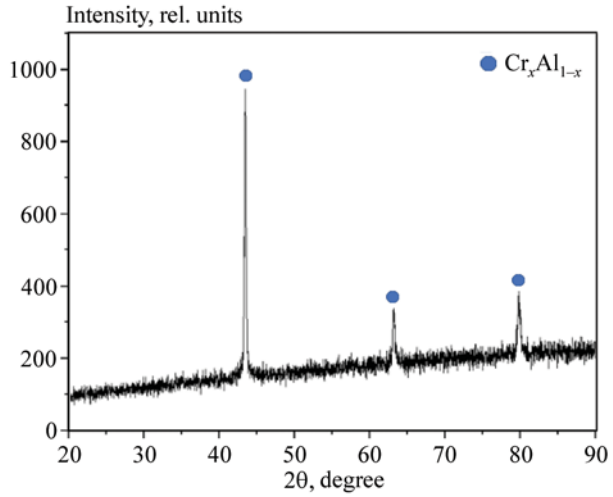

Fig. 12. *X*-ray diffraction analysis of the Cr–Al alloy ingot

Рис. 12. Рентгенофазовый анализ полученного слитка системы Cr–Al

Chemical analysis of the synthesized alloys

When developing chemical methods for alloy production, such as SHS metallurgy, the composition of the reaction mixture is one of the most critical parameters. This composition determines key process conditions, including temperature, reduction efficiency (completeness of reduction of the initial components), and the separation of the slag and metallic phases. In addition to ensuring that the alloy meets the target chemical composition in terms of the main elements, it is also important to monitor the presence and concentrations of impurities. Comprehensive composition control, including all trace elements, is essential for achieving stable and

reproducible physical and mechanical properties in advanced high-strength metallic materials.

Tables 3—5 present the full chemical analysis of the synthesized alloys, performed using inductively coupled plasma mass spectrometry (ICP-MS). This method combines an inductively coupled plasma ion source with a mass spectrometer for ion separation and detection and is considered one of the most advanced techniques in modern materials analysis.

In modern metallurgical production, considerable attention is given to the mass fraction of various gases present in metals. The key gases that influence alloy properties are nitrogen, oxygen, and hydrogen. The most commonly used method for determining gas content in metals is combustion analysis, which enables the detection of gas impurities with an accuracy of up to 0.00001 %. Table 6 presents the results of the analysis of the synthesized Cr—Mo and Cr—W alloys for carbon, sulfur, and gas impurities.

Table 3. **Chemical composition of the synthesized Cr–Mo (Al) alloy**

Таблица 3. Результаты химического анализа синтезированного сплава системы Cr–Mo (Al)

Element	Mass fraction, wt. %	Element	Mass fraction, wt. %	Element	Mass fraction, wt. %
Li	<0.0005	Zn	<0.0005	Sm	<0.0003
Be	<0.0003	As	<0.0005	Eu	<0.0003
B	<0.0002	V	<0.0003	Gd	<0.0004
Al	4.27	Rb	<0.0005	Tb	<0.0003
Na	0.0018	Sr	<0.0002	Dy	<0.0007
Mg	<0.0003	Y	<0.0002	Ho	<0.0003
Si	0.4271	Ga	<0.0007	Er	<0.0003
Ca	<0.0003	Ge	<0.0008	Tm	<0.0001
P	0.0010	Zr	0.0005	Yb	<0.0002
K	0.0020	Nb	<0.001	Lu	<0.0005
Sc	<0.0003	Mo	53.02	Hf	<0.0001
Ti	0.0025	Sn	<0.001	Pt-e	<0.002
Cr	42.51	Sb	<0.0003	Re	<0.0002
Fe	0.2110	Ba	<0.0001	W	0.0564
Mn	<0.0002	La	<0.0003	Pb	<0.0003
Co	<0.0005	Ce	<0.0006	Th	<0.0002
Ni	0.0043	Pr	<0.0005	U	<0.0005
Cu	<0.001	Nd	<0.0007	Ta	0.0011

Table 4. **Chemical composition of the synthesized Cr–W (Al) alloy**

Таблица 4. Результаты химического анализа синтезированного сплава системы Cr–W (Al)

Element	Mass fraction, wt. %	Element	Mass fraction, wt. %	Element	Mass fraction, wt. %
Li	<0.0005	Zn	0.0010	Sm	<0.0003
Be	<0.0003	As	<0.0005	Eu	<0.0003
B	<0.0002	V	<0.0003	Gd	<0.0004
Al	4.82	Rb	<0.0005	Tb	<0.0003
Na	0.0019	Sr	0.0006	Dy	<0.0007
Mg	<0.0003	Y	<0.0002	Ho	<0.0003
Si	0.4509	Ga	<0.0007	Er	<0.0003
Ca	<0.0003	Ge	<0.0008	Tm	<0.0001
P	0.0011	Zr	0.0020	Yb	<0.0002
K	0.0062	Nb	<0.001	Lu	<0.0005
Sc	<0.0003	Mo	<0.0006	Hf	<0.0001
Ti	0.0218	Sn	<0.001	Pt-e	<0.002
Cr	42.17	Sb	<0.0003	Re	<0.0002
Fe	0.2131	Ba	<0.0001	W	52.61
Mn	0.0036	La	<0.0003	Pb	0.0019
Co	<0.0005	Ce	<0.0006	Th	<0.0002
Ni	0.0061	Pr	<0.0005	U	<0.0005
Cu	<0.001	Nd	<0.0007	Ta	<0.0005

Table 5. **Chemical composition of the synthesized Cr–Al alloy**

Таблица 5. Результаты химического анализа синтезированного сплава системы Cr–Al

Element	Mass fraction, wt. %	Element	Mass fraction, wt. %	Element	Mass fraction, wt. %
C	0.015	Ni	0.02	Pb	<0.0005
Si	0.15	W	0.06	Sn	<0.001
S	0.002	Fe	0.17	As	0.0006
P	0.012	N	0.0076	Sb	0.001
Cr	85.2	O	0.0017	Bi	<0.0001
Al	12.43	H	0.0021	Zn	0.002
Mo	0.02	Cu	<0.001	Cd	<0.0001

Table 6. **Results of chemical analysis of the synthesized Cr–Mo (Al) and Cr–W (Al) alloys for carbon, sulfur, and gas impurities**

Таблица 6. Результаты химического анализа синтезированных сплавов Cr–Mo (Al) и Cr–W (Al) на наличие углерода, серы и газовых примесей

Alloy	Mass fraction, wt. %				
	C	S	O	N	H
Cr–Mo (Al)	0,011	0,0028	0,042	0,019	0,0014
Cr–W (Al)	0,0091	0,00078	0,12	0,0072	0,0012

Analysis of the obtained chemical composition data allows us to conclude that the synthesized alloys meet all key requirements for permissible concentrations of both target elements and impurities. It is particularly worth noting the low content of harmful impurities such as sulfur and hydrogen.

Conclusion

This study included thermodynamic analyses of combustion temperatures for the investigated exothermic systems Mo—Cr, W—Cr, Cr_2O_3—Al, and CrO_3—Al. These analyses confirmed that there are no thermodynamic barriers to the synthesis of the target materials using SHS metallurgy.

The main conclusions drawn from this work are as follow:

1. A comprehensive series of experiments demonstrated that in the production of master alloys based on refractory elements (Mo—Cr and W—Cr), as well as systems with a significant difference in melting points (Cr—Al), the mass of the reaction mixture should be increased to 1.5—2.0 kg in order to extend the time the melt remains in the liquid state (the melt "lifetime").

2. The centrifugal acceleration applied should be at least 50 *g*.

3. To increase the synthesis temperature when producing ingots in the Cr—Al system, a combined oxidizer should be used, consisting of a mixture of chromium (III) oxide and chromium (VI) oxide, with the Cr_2O_3 /CrO_3 ratio ranging from 70/30 to 40/60.

4. The experiments confirmed the necessity of introducing functional additives at 3 % of the oxidizer mass. These additives should be a combination of cryolite and fluorite, to lower the melting temperature of the slag phase and thereby improve the phase separation between the metallic and oxide phases.

5. Analysis of the Cr—Mo (Al) and Cr—W (Al) master alloys demonstrated the need to introduce an excess amount of MoO_3 and WO_3, respectively, due to the incomplete reduction of Mo and W from their oxides.

6. Microstructural analysis of the obtained master alloys revealed the presence of a dendritic structure, which is typical for cast alloys.

7. *X*-ray phase analysis results highlighted the importance of using a ceramic mold to ensure uniformity of the material's phase composition.

8. The chemical composition analysis of the synthesized Mo—Cr (Al), W—Cr (Al), and Cr—Al alloys, performed using ICP-MS, confirmed that the target compositions were achieved and fully met the permissible concentration requirements for both target elements and impurities. Particularly noteworthy is the low content of harmful impurities such as sulfur and hydrogen.

References

1. Goldshtein M.I., Grachev S.V., Veksler Yu.G. Special steels. Moscow: MISIS, 1999. 408 p. (In Russ.).
Гольдштейн М.И., Грачев С.В., Векслер Ю.Г. Специальные стали. М: МИСИС, 1999. 408 с.
2. Solntsev Yu.P., Pryakhin E.I., Pirainen V.Yu. Special materials in mechanical engineering. Saint Petersburg: Khimizdat, 2004. 640 p. (In Russ.).
Солнцев Ю.П., Пряхин Е.И., Пирайнен В.Ю. Специальные материалы в машиностроении. СПб.: Химиздат, 2004. 640 с.
3. Lyakishev N.P., Gasik M.I. Metallurgy of chromium. Moscow: Eliz, 1999. 581 p. (In Russ.)
Лякишев Н.П., Гасик М.И. Металлургия хрома. М.: Элиз, 1999. 581 с.
4. Yukhvid V.I., Gorshkov V.A., Sanin V.N., Andreev D.E., Vdovin Yu.S. SHS metallurgy of refractory materials based on molybdenum. In: *Explosive production of new materials: science, technology, business, and innovations:* 14th International Symposium (Saint Petersburg, 14—18 May 2018). Ed. M.I. Alymov, O.A. Golosova. Moscow: Torus Press, 2018. P. 294—297.
5. Structural chromium alloys. Ed. V.I. Trefilov. Kyiv: Naukova Dumka, 1986. 216 p. (In Russ.).
Конструкционные сплавы хрома: Сб. науч. трудов. Отв. ред. В.И. Трефилов. Киев: Наукова думка, 1986. 216 с.
6. Kolobov Yu.R., Manokhin S.S., Kudymova Yu.E., Klimenko D.N., Sanin V.N., Ikornikov D.M., Andreev D.E. SHS-produced cast Ni—Cr—W alloy: structural characterization and mechanical properties. In: *Book of abstracts of XIV International Symposium on Self-Propagating High Temperature Synthesis (SHS-2017)* (Tbilisi, Georgia, 25—28 September 2017). 2017. P. 230—231.

7. Yukhvid V.I., Andreev D.E., Sanin V.N., Sachkova N.V. SHS metallurgy of composite materials based on the Nb—Si system. *Russian Journal of Non-Ferrous Metals.* 2018;59(1):42—49.
8. Ziatdinov M.Kh., Shatokhin I.M., Leont'ev L.I. SHS technology of composition ferroalloys Part I. Metallurgical SHS process. Synthesis of ferrovanadium and ferrochromium nitrides. *Izvestiya. Ferrous Metallurgy.* 2018;61(5):339—347. (In Russ.).
https://doi.org/10.17073/0368-0797-2018-5-339-347
Зиатдинов М.Х., Шатохин И.М., Леонтьев Л.И. Технология СВС композиционных ферросплавов. Часть I. Металлургический СВС процесс. Синтез нитридов феррованадия и феррохрома. *Известия вузов. Черная металлургия.* 2018;61(5):339—347.
https://doi.org/10.17073/0368-0797-2018-5-339-347
9. Ziatdinov M.Kh., Shatokhin I.M., Leont'ev L.I. SHS technology of composition ferroalloys Part II. Synthesis of ferrosilicon nitride and ferrotitanium boride. *Izvestiya. Ferrous Metallurgy.* 2018;61(7):527—535. (In Russ.).
https://doi.org/10.17073/0368-0797-2018-7-527-535
Зиатдинов М.Х., Шатохин И.М., Леонтьев Л.И. Технология СВС композиционных ферросплавов. Часть II. Синтез нитрида ферросилиция и борида ферротитана. *Известия вузов. Черная металлургия.* 2018;61(7):527—535.
https://doi.org/10.17073/0368-0797-2018-7-527-535
10. Ziatdinov M.Kh. Metallurgical SHS processes as a route to industrial-scale implementation: An autoreview. *Internationsl Journal of Self-Propagating High-Temperature Synthesis.* 2018;27(1):1—13.
https://doi.org/10.3103/S1061386218010132
11. Sanin V.N., Yukhvid V.I., Andreev D.E., Alymov M.I. Centrifugal SHS metallurgy. Solving practical problems. In: *Material-forming highly exothermic processes: metallothermy and combustion of thermite-type systems*. Ed. M.I. Alymov. Moscow: RAS, 2021. Chapter 7. P. 321—372. (In Russ.).
Санин В.Н., Юхвид В.И., Андреев Д.Е., Алымов М.И. Центробежная СВС-металлургия. Решение практических задач. В кн. *Материалообразующие высокоэкзотермические процессы: металлотермия и горение систем термитного типа*. Под общ. ред. М.И. Алымова. М.: РАН, 2021. Глава 7. С. 321—372.
12. Yukhvid V.I., Ikornikov D.M., Andreev D.E., Sanin V.N., Alymov M.I., Sachkova N.V., Semenova V.N., Kovalev I.D. Centrifugal SHS-metallurgy of nitrogen steels. *Letters on Materials.* 2018;8(4(32)):499—503.
13. Yukhvid V.I., Gorshkov V.A., Sanin V.N. Production of new ceramic and composite materials using SHS metallurgy methods. In: *Technological combustion*. Eds. S.M. Aldoshin, M.I. Alymov. Moscow: Institute of Problems of Chemical Physics of the RAS, 2018. Chapter 14. P. 350—371. (In Russ.).
https://doi.org/10.31857/S9785907036383000014
Юхвид В.И., Горшков В.А., Санин В.Н. Получение новых керамических и композиционных материалов методами СВС-металлургии. В кн. *Технологическое горение.* Под общ. ред. С.М. Алдошина, М.И. Алымова. М.: ИПХФ РАН, 2018. Глава 14. С. 350—371.
https://doi.org/10.31857/S9785907036383000014
14. Sanin V., Andreev D., Ikornikov D., Yukhvid V. Cast intermetallic alloys and composites based on them by combined centrifugal casting — SHS process. *Open Journal of Metal.* 2013;3(2B):12—24.
https://doi.org/10.4236/ojmetal.2013.32A2003
15. Lyakishev N.P., Gasik M.I., Dashevsky V.Ya. Metallurgy of ferroalloys. Part 1. Metallurgy of silicon, manganese and chromium alloys. Moscow: MISIS, 2006. 117 p. (In Russ.).
Лякишев Н.П., Гасик М.И., Дашевский В.Я. Металлургия ферросплавов. Ч. 1. Металлургия сплавов кремния, марганца и хрома: Учеб. пос. М.: МИСИС, 2006. 117 с.
16. Yukhvid V.I., Andreev D.E., Sanin V.N., Gorshkov V.A., Alymov M.I. Synthesis of cast composite materials by SHS metallurgy methods. *Key Engineering Materials.* 2017;(746):219—232.
https://doi.org/10.4028/www.scientific.net/KEM.746.219
17. Sanin V.N., Ikornikov D.M., Golosova O.A., Andreev D.E., Yukhvid V.I. Centrifugal SHS metallurgy of cast Co—Cr—Fe—Ni—Mn high-entropy alloys strengthened by precipitates based on Mo and Nb borides and silicides. *Physical Mesomechanics.* 2021;24(6):692—700.
https://doi.org/10.1134/S1029959921060072
18. Sanin V.N., Yukhvid V.I., Andreev D.E., Ikornikov D.M., Levashov E.A., Pogozhev Yu.S. SHS of cast refractory alloys for reprocessing into micro granules used in 3D additive technologies. In: *Book of abstracts of XIV International Symposium on Self-Propagating High Temperature Synthesis (SHS-2017)* (Tbilisi, Georgia, 25—28 September 2017). 2017. P. 224—226.
19. Bannykh O.A., Budberg P.B., Alisova S.P. State diagrams of binary and multicomponent iron-based systems. Moscow: Metallurgiya, 1986. 440 p. (In Russ.).
Банных О.А., Будберг П.Б., Алисова С.П. Диаграммы состояния двойных и многокомпонентных систем на основе железа. М.: Металлургия, 1986. 440 с.
20. Lyakishev N.P. Phase diagrams of binary metal systems. Moscow: Mashinostroenie, 1997. Vol. 2. 1023 p. (In Russ.).

Лякишев Н.П. Диаграммы состояния двойных металлических систем. М.: Машиностроение, 1997. Т. 2. 1023 с.

21. Kocherzhinskii Yu.A., Vasilenko V.I. Fusibility diagrams of the systems Mo—Nb (V, Cr), V—Nb (Cr), and Mo—V—Nb (Cr). *Russian Metallurgy (Metally).* 1985;(2):186—190.
22. Kocherzhinskii Yu.A., Vasilenko V.I. Fusibility diagram of molybdenum—chromium. *Russian Metallurgy (Metally).* 1979;(4):205—207.
23. Nagender Naidu S.V., Sriramamurthy A.M., Rama Rao P. The Cr—W (chromium—tungsten) system. *Bulletin of Alloy Phase Diagrams.* 1984;5(3):289—307.
24. Alisova S.P., Budberg P.B., Ageev N.V. Phase diagrams of metallic systems. Moscow: VINITI, 1975. 268 p. (In Russ).
Алисова С.П., Будберг П.Б., Агеев Н.В. Диаграммы состояния металлических систем. М.: ВИНИТИ, 1975. 268 с.
25. Nurse R.W., Welch J.H., Majumdar A.J. The CaO—Al_2O_3 system in a moisture-free atmosphere. *Transactions of the British Ceramic Society.* 1965;64:409—418.
26. Nurse R.W., Welch J.H., Majumdar A.J. The $12CaO{\cdot}7Al_2O_3$ phase in the CaO—Al_2O_3 system. *Transactions of the British Ceramic Society.* 1965;64:323—382.

Information about the authors

Anastasiya N. Kubanova – Graduate Student of the Merzhanov Institute of Structural Macrokinetics and Materials Science of the Russian Academy of Sciences (ISMAN), Junior Research Scientist of Tula State Pedagogical University n.a. L.N. Tolstoy.
https://orcid.org/0000-0001-6685-1447
E-mail: kubanovaan@tsput.ru

Denis M. Ikornikov – Research Scientist, ISMAN.
https://orcid.org/0000-0002-8082-4442
E-mail: denis-ikornikov@yndex.ru

Vladimir N. Sanin – Dr. Sci. (Eng.), Senior Research Scientist, ISMAN.
https://orcid.org/0000-0001-8402-4605
E-mail: svn@ism.ac.ru

Dmitry A. Martynov – General Manager of LLC "Research, Design and Technology Center".
E-mail: martynov@rdtcenter.com

Информация об авторах

Анастасия Николаевна Кубанова – аспирант Института структурной макрокинетики и проблем материаловедения им. А.Г. Мержанова РАН (ИСМАН), мл. науч. сотрудник Тульского государственного педагогического университета им. Л.Н. Толстого.
https://orcid.org/0000-0001-6685-1447
E-mail: kubanovaan@tsput.ru

Денис Михайлович Икорников – науч. сотрудник ИСМАН.
https://orcid.org/0000-0002-8082-4442
E-mail: denis-ikornikov@yndex.ru

Владимир Николаевич Санин – д.т.н., ст. науч. сотрудник ИСМАН.
https://orcid.org/0000-0001-8402-4605
E-mail: svn@ism.ac.ru

Дмитрий Александрович Мартынов – ген. директор ООО «Центр исследований, дизайна и технологий».
E-mail: martynov@rdtcenter.com

Contribution of the authors

A.N. Kubanova – literature review, analysis of experimental data, manuscript writing.

D.M. Ikornikov – preparation of mixtures and raw materials, experimental work, participation in result discussions.

V.N. Sanin – definition of the research objective, experimental work, participation in result discussions, manuscript editing.

D.A. Martynov – problem formulation and definition of the research objective, participation in result discussions.

Вклад авторов

А.Н. Кубанова – анализ литературных данных, работа с экспериментальными данными, написание статьи.

Д.М. Икорников – подготовка материалов для экспериментов, проведение экспериментов, участие в обсуждении результатов.

В.Н. Санин – определение цели работы, проведение экспериментов, участие в обсуждении результатов, редактирование статьи.

Д.А. Мартынов – описание проблемы и определение цели работы, участие в обсуждении результатов.

The article was submitted 08.04.2024, revised 18.07.2024, accepted for publication 22.07.2024

Статья поступила в редакцию 08.04.2024, доработана 18.07.2024, подписана в печать 22.07.2024

FOUNDRY / ЛИТЕЙНОЕ ПРОИЗВОДСТВО

UDC 621.74.045
https://doi.org/10.17073/0021-3438-2025-1-41-57

Research article
Научная статья

Influence of coatings for urea-based patterns on the quality of shell molds produced using colloidal silica binders

V.E. Bazhenov[1], E.P. Kovyshkina[1], A.A. Nikitina[1], Yu.V. Tselovalnik[1], A.A. Belova[1], A.V. Koltygin[1], V.D. Belov[1], B.E. Hvatskov[2]

[1] **National University of Science and Technology "MISIS"**
1 Bld, 4 Leninskiy Prosp., Moscow 119049, Russia

[2] **PJSC "UEC-Kuznetsov"**
29 Zavodskoe Shosse, Samara 443009, Russia

✉ Viacheslav E. Bazhenov (V.E.Bagenov@gmail.com)

Abstract: In the investment casting process, in addition to wax patterns, water-soluble salt patterns made of urea are also used. It is known that urea-based patterns provide high strength and allow the patterns to maintain their shape even if the temperature in the foundry increases. However, due to environmental and production-related reasons, there is currently a growing demand for transitioning to a technological process involving colloidal silica binder. This transition presents challenges related to the manufacturing of ceramic shell molds due to the interaction between the pattern compound and the colloidal silica binder slurry. This study examines the effectiveness of protective coatings based on repair wax, varnish (AK 593), and varnish with rosin, applied to water-soluble urea-based patterns containing additives such as magnesium sulfate, potassium nitrate, polyvinyl alcohol, and dimethylglyoxime. The degree of interaction was assessed by measuring the wetting angle and the spreading area of the colloidal silica binder over the surface of pattern samples with various coatings. It was found that all coatings contributed to an increase in the wetting angle and a reduction in the spreading area. Additionally, ceramic molds and castings made of nickel superalloy were produced using a series of pattern compounds with protective coatings. The surface roughness and dimensional accuracy of the castings were evaluated. It was demonstrated that the protective properties of the repair wax-based coating were insufficient, leading to the formation of cracks and sagging in the mold. This resulted in penetration defects in the castings and a significant decrease in dimensional accuracy. In contrast, when using coatings based on varnish and varnish with rosin, no defects were observed in the mold or castings, making these coatings recommended as protective solutions for urea-based pattern compounds in contact with colloidal silica binder slurries.

Keywords: urea-based pattern compounds, water-soluble salt patterns, colloidal silica binders, protective coatings, wetting angle.

Acknowledgments: This research received financial support from the Ministry of Science and Higher Education in the Russian Federation (Agreement No. 075-11-2022-023 from 06 April 2022) under the program "Scientific and technological development of the Russian Federation" according to governmental decree No. 218 dated 09 April 2010.

For citation: Bazhenov V.E., Kovyshkina E.P., Nikitina A.A., Tselovalnik Yu.V., Belova A.A., Koltygin A.V., Belov V.D., Hvatskov B.E. Influence of coatings for urea-based patterns on the quality of shell molds produced using colloidal silica binders. *Izvestiya. Non-Ferrous Metallurgy.* 2025;31(1):41–57. https://doi.org/10.17073/0021-3438-2025-1-41-57

Влияние покрытий для карбамидных моделей на качество оболочковых форм, полученных с применением водных связующих

В.Е. Баженов[1], **Е.П. Ковышкина**[1], **А.А. Никитина**[1], **Ю.В. Целовальник**[1], **А.А. Белова**[1], **А.В. Колтыгин**[1], **В.Д. Белов**[1], **Б.Е. Хвацков**[2]

[1] **Национальный исследовательский технологический университет «МИСИС»**
Россия, 119049, г. Москва, Ленинский пр-т, 4, стр. 1

[2] **ПАО «ОДК-Кузнецов»**
Россия, 443009, г. Самара, Заводское шоссе, 29

✉ Вячеслав Евгеньевич Баженов (V.E.Bagenov@gmail.com)

Аннотация: При изготовлении отливок методом литья по выплавляемым моделям наряду с восковыми выплавляемыми используют и водорастворимые солевые модели на основе карбамида. Известно, что карбамидные модельные массы обеспечивают высокую прочность и позволяют сохранять форму моделей даже в случае повышения температуры в цехе. Тем не менее в силу экологических и производственных причин в настоящее время актуальным является переход на технологический процесс с применением готовых водных связующих на основе силиказоля. При этом возникают проблемы, связанные с изготовлением керамической оболочковой формы, из-за взаимодействия модельной массы и суспензии на водном связующем. В работе рассмотрена эффективность защитных покрытий на основе ремонтного воска, лака (АК 593) и лака с канифолью, нанесенных на водорастворимые модели на основе карбамида с добавками сульфата магния, нитрата калия, поливинилового спирта и диметилглиоксима. Степень взаимодействия оценивали по краевому углу смачивания и площади растекания водного связующего по поверхности образцов модельных масс с различными покрытиями. Было установлено, что все покрытия обеспечивают увеличение краевого угла смачивания и уменьшение площади растекания. Также с использованием ряда модельных составов с защитными покрытиями были получены керамические формы и отливки из никелевого жаропрочного сплава, для которых оценивали шероховатость и размерную точность. Было показано, что в случае нанесения покрытия на основе ремонтного воска защитные свойства недостаточны, что приводит к появлению трещин и наплывов в форме. В отливке это выражается в образовании механического пригара и значительном снижении размерной точности. В случае применения покрытий на основе лака и лака с канифолью каких-либо дефектов в форме или отливке не наблюдается, и именно эти покрытия можно рекомендовать в качестве защитных при использовании модельных составов на основе карбамида и суспензий на основе водных связующих.

Ключевые слова: литье по выплавляемым моделям, карбамидные модельные массы, растворимые солевые модели, водные связующие, защитные покрытия, краевой угол смачивания.

Благодарности: Работа выполнена при финансовой поддержке Министерства науки и высшего образования Российской Федерации в рамках Постановления Правительства РФ № 218 от 09.04.2010 г. по соглашению о предоставлении субсидии № 075-11-2022-023 от 06.04.2022 г. «Создание технологии изготовления уникальных крупногабаритных отливок из жаропрочных сплавов для газотурбинных двигателей, ориентированной на использование отечественного оборудования и организацию современного ресурсоэффективного, компьютероориентированного литейного производства».

Для цитирования: Баженов В.Е., Ковышкина Е.П., Никитина А.А., Целовальник Ю.В., Белова А.А., Колтыгин А.В., Белов В.Д., Хвацков Б.Е. Влияние покрытий для карбамидных моделей на качество оболочковых форм, полученных с применением водных связующих. *Известия вузов. Цветная металлургия.* 2025;31(1):41–57. https://doi.org/10.17073/0021-3438-2025-1-41-57

Introduction

Among the currently applied foundry technologies for the production of large thin-walled castings from nickel superalloys, the investment casting method is predominantly used [1—2]. This method is based on obtaining a pattern of the future casting in a metallic die, most often from pattern compounds based on waxes [3]. However, wax-based pattern compounds have several drawbacks, prompting aerospace enterprises to continue using water-soluble salt patterns made of urea (CH_4N_2O) for the production of large shell castings [4—9]. The advantages of water-soluble salt patterns include high strength, hardness, low linear shrinkage, and low ash content [10; 11]. In addition to minimal shrinkage, the absence of softening and creep of the water-soluble salt pattern at elevated temperatures, which is typical for wax patterns, contributes to the

high dimensional accuracy of the resulting castings [12]. Urea is also used in the production of foamed materials by the investment casting method [13—15]. Alongside the conventional method of producing water-soluble salt patterns in dies, additive manufacturing technologies can also be employed [16].

Since salt-based patterns are water-soluble, it is necessary to prevent their dissolution during the formation of the ceramic shell [17]. One of the solutions to this problem is the use of slurries that do not contain chemically free water, such as those based on hydrolyzed ethyl silicate solution (ETS) [18]. However, several issues arise with the use of ETS in production. It is known that the curing of ETS-based slurry occurs in an acidic environment, while urea has a nearly neutral to alkaline pH [17]. As a result, contact between the pattern and the slurry leads to a deterioration of the inner mold layer quality and its weakening, which affects the quality of the castings [10]. At the same time, the use of ETS-based slurries in modern production is environmentally unfriendly due to the requirement for ammonia vapor to dry the investment shell layers, and the ETS-based mold manufacturing process cannot be automated [18].

Currently, slurries with colloidal silica binders are gradually replacing ETS-based slurries. Unlike the latter, they are non-flammable and cure by air drying, making them suitable for automated or robotic foundry production. However, the issue of dissolution and subsequent interaction with salt patterns is even more acute for colloidal silica binder-based slurries compared to hydrolyzed ethyl silicate-based slurries [17].

One way to reduce the intensity of interaction between salt patterns and shell molds is to modify the composition of the pattern compound, for example, by adding components that reduce the dissolution rate of the patterns. The main additives to urea in salt pattern compounds include magnesium sulfate, potassium nitrate, polyvinyl alcohol, ethylene vinyl acetate, and wax [19; 20]. In [12], the addition of dimethylglyoxime to the pattern compound was proposed to reduce hygroscopicity. The analysis of the wetting angle when applying an colloidal silica binder to pattern compounds containing magnesium sulfate, polyvinyl alcohol, potassium nitrate, and dimethylglyoxime showed that polyvinyl alcohol and dimethylglyoxime contribute to an increase in the wetting angle and a decrease in the interaction of the binder with the pattern compound [21].

A more preferable approach to preventing the interaction of the pattern compound with the colloidal silica binder slurry is to protect the salt-based patterns by applying water-resistant protective coatings to their surface. For example, urea-based patterns can be briefly immersed in liquid paraffin or another wax-based pattern compound to form a hydrophobic film on their surface [10]. According to [22], a protective coating formed by dissolving 3 wt. % of mixture of stearine and paraffin (1/1) in 100 mL of rubber solvent petrol provides the maximum wetting angle and the smallest spreading area of the slurry on the pattern surface. The use of such a protective coating allowed for the production of ceramic shells with low surface roughness. In [23], the use of bituminous and perchlorovinyl varnishes with mixed solvents is proposed as protective coatings. Depending on the degree of dilution, these varnishes allow for protective film thicknesses ranging from 4 to 10 μm, which does not significantly affect the dimensional accuracy of the resulting castings.

Another interesting method for reducing the interaction between urea-based patterns and colloidal silica binders is the application of a mixed mold-making technology. In studies [24; 25], it is proposed to apply a layer of slurry based on hydrolyzed ethyl silicate solution first, followed by a layer of slurry with a colloidal silica binder. This approach partially protects the water-soluble pattern from interacting with the colloidal silica binder; however, it introduces additional technological operations and does not fully resolve the issue associated with the use of hazardous components in production.

Thus, there are two main ways to limit the interaction between the pattern compound and the slurry: modifying the composition of the pattern compound and applying a hydrophobic coating to the pattern surface. Their combined study presents both scientific and practical interest. In this regard, the aim of this study was to investigate the interaction of various pattern compounds after applying protective coatings with colloidal silica binders.

Materials and methods

Five urea-based pattern compounds with additives of magnesium sulfate, polyvinyl alcohol, potassium nitrate, and dimethylglyoxime were selected as materials for the study (Table 1). Their primary properties having been previously investigated in [21]. It was shown that the additives of polyvinyl alcohol and dimethylglyoxime contribute to an increase in the wetting angle between the colloidal silica binder and the pattern compound [21].

Water-soluble patterns, featuring a sprue with attached parallelepiped elements measuring $10 \times 25 \times 25$ mm (Fig. 1), were produced using an aluminum alloy die.

Protective coatings based on repair wax and varnish AK 593 were examined (see Table 2). The varnish is based on a copolymer of methacrylic acid and methacrylic acid butyl ester. It is uncertain whether the slurry will remain on the pattern surface after applying varnish AK 593, as it may run off due to an excessively high wetting angle. Therefore, an additional coating option was considered, where a layer of rosin was applied over the varnish to improve surface wettability [26].

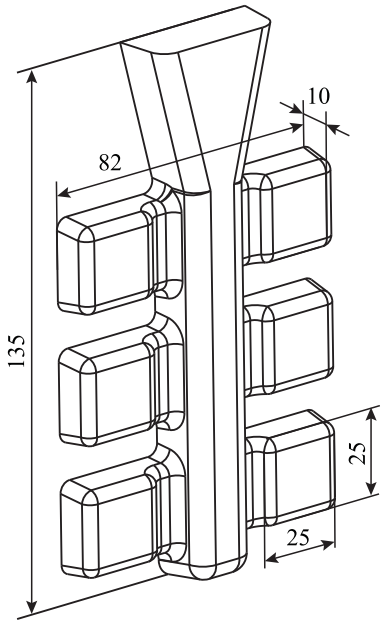

Fig. 1. Schematic representation of the water-soluble pattern

Рис. 1. Схематичное изображение растворимой модели

Three protective coatings were applied to the water-soluble patterns produced using each of the five pattern compound variants. The composition of the coatings and the sequence of their application are presented in Table 2. The coatings used include wax-based (#W), varnish AK 593-based (#V), and varnish with rosin (#V + R).

To assess the degree of interaction between the pattern compounds and the colloidal silica binder, as well as the protective effectiveness of the coatings, the wetting angle and the spreading area of the colloidal silica binder on the surface of the coated pattern compounds samples were determined. The lower the wetting angle and the larger the spreading area, the more intensive the interaction between the liquid and the substrate.

To determine the wetting angle using the sessile drop method and to measure the spreading area, three drops (0.08—0.09 mL) of the binder UltraCast One+ were

Table 1. **Composition of pattern compounds**

Таблица 1. Состав модельных масс

Compound	Components of the pattern compound and their content, wt. %				
	Urea CH_4N_2O	Magnesium sulfate $MgSO_4$	Polyvinyl alcohol $(C_2H_4O)_x$	Potassium nitrate KNO_3	Dimethylglyoxime $C_4H_8N_2O_2$
#1	98	2	–	–	–
#2	96	2	2	–	–
#3	90	–	–	10	–
#4	88	–	2	10	–
#5	88	–	–	10	2

Table 2. **Investigated protective coatings**

Таблица 2. Исследуемые защитные покрытия

Coating type	Composition and application sequence
#W	3 g of repair wax (a mixture of ceresin and petrolatum) in 100 mL of rubber solvent, applied in 2 layers using a sponge
#V	Varnish AK 593, applied in 1 layer by dipping
#V + R	Varnish AK 593, applied in 1 layer by dipping, followed by 5 g of pine rosin in 100 mL of ethanol, applied in 2 layers using a sponge

applied to the surface of pattern samples using a plastic pipette. The droplet behavior was recorded from the side using a SONY NEX EA50H video camera in macro mode with a Sony E PZ 18-200 mm F3.5—6.3 macro lens and Meike MK-S-AF3A macro rings. Frames were extracted from the video at the moment of droplet application and subsequently every 10 s during the first minute. From the second minute onwards, the frame extraction interval was increased to 1 min. The final frame corresponded to a 6-min hold time. After the experiment, a top-view image of the droplet was captured to determine the spreading area. For each pattern composition and type of coating, the experiment to determine the wetting angle and spreading area was conducted on three samples. The wetting angle and spreading area were measured from the extracted frames using the image analysis software ImageJ 1.52a (National Institutes of Health, USA).

To assess the quality of the castings obtained using the experimental pattern compounds and coatings, ceramic molds were produced and used to cast samples from the nickel superalloy. This alloy is widely used in domestic aerospace applications for the production of large shell castings employed in structural elements of combustion chambers. For this reason, the alloy is often cast into ceramic molds made using fused quartz as a filler.

Patterns produced from compounds #2 and #5 with all coating variants were used to fabricate ceramic molds. Various properties of colloidal silica binders, slurries, and ceramic samples obtained with their use were previously investigated in [27]. The ceramic mold fabrication technology and materials described below were selected based on the results of that study.

The slurry was prepared by mixing 5 L of binder with 10 kg of fine fused quartz with fraction 0.045 mm (supplied by LLC “Kefron”, Yekaterinburg). The first and second ceramic layers were made using the binder UltraCast One+, while the subsequent layers were made using UltraCast Prime (both produced by LLC “Technopark”, Moscow). After mixing, the slurry was left to stand for 24 h to ensure proper wetting of the micropowder with the binder and to remove air bubbles. Before use, the slurry was thoroughly mixed again. Its viscosity was determined using a DIN flow cup viscometer. If the viscosity did not meet the target values (60 s for the slurry used in the first and second layers, and 40 s for the third and subsequent layers), additional binder was added, the slurry was remixed, and viscosity measurements were repeated until the required values were achieved. The slurry was applied to the pattern by dipping, followed by stuccoing with fused quartz of varying particle sizes: 0.25—0.4 mm (for layers 1—2), 0.4—0.6 mm (for layers 3—4), and 0.5—1.0 mm (for layers 5—7), all supplied by LLC “Kefron”. The final 8^{th} layer of slurry was applied without subsequent stuccoing (as a finishing layer). The first layer was dried in air at a temperature of 21—22 °C and relative humidity of 55—72 % for 2 h, while each subsequent layer was dried with air circulation at 21—22 °C and relative humidity of 64—85 % for 2 h.

The pattern was removed 24 h after applying the final layer by dissolving it in hot water at a temperature of 95 ± 5 °C.

The prepared molds were placed in a container and externally filled with a supporting refractory—coarse quartz sand. The molds were then subjected to burnout processing, during which they were heated to a temperature of 900 °C over 2 h, followed by a 4-hour holding period. Before pouring, the container with the molds was transferred to the pouring area. A ready-made nickel-based superalloy (wt. %: Ni — base; C — up to 0.08; Cr — up to 20.0; Mo — up to 5.0; Al — up to 1.5; Ti — up to 2.9; Nb — up to 2.8; Fe — up to 10), produced by VIAM (Moscow), was used as the charge. The melting was carried out in an induction furnace (SPE “RELEK”, Ekaterinburg) using a periclase crucible (STC “Bakor”, Shcherbinka). The mass of the melted alloy was 8 kg. The melt was protected by a covering flux of crushed silicate glass. The metal was poured into the ceramic molds at a temperature of approximately 1500 °C.

A distinctive feature of the investment casting method is the high dimensional accuracy and low surface roughness of the produced castings. Therefore, for the castings obtained using different pattern compounds and coatings, surface roughness and dimensional deviations were assessed. Additionally, shrinkage was calculated based on the measured dimensions, as it is an important parameter to consider when developing casting technologies.

The surface roughness of the cast samples was measured using an M300C profilometer (MarSurf, Germany). The average value was obtained from seven measurements.

To determine the dimensions of the cast samples and their linear shrinkage, laser scanning of the castings was performed using a handheld 3D scanner KScan Magic (ScanTech, China). The device’s measurement accuracy was ± 20 μm. The cloud of points was processed using Geomagic Design X software (3D Systems, USA). The width of the casting (l_c) was measured at three points. Knowing the width of the mold cavity used to produce the pattern (l_p = 82 mm), the total linear shrinkage of the

pattern, ceramic mold, and alloy was calculated using the following equation: $\varepsilon = [(l_p - l_c)/l_p] \cdot 100$ %.

Since high-temperature alloys are prone to interaction with mold materials, the structure of the surface layers of the mold and castings was examined. The microstructure and phase composition of the surface layer of the castings and molds were analyzed using a scanning electron microscope (SEM) Vega SBH3 (Tescan, Czech Republic) equipped with an energy-dispersive microanalysis attachment (Oxford, UK), as well as an optical microscope (OM) Axio Observer. D1m (Carl Zeiss, Germany).

Results and discussion

Fig. 2 illustrates the dependence of the wetting angle (θ) on the holding time (τ) of the binder droplet on the surface of the tested pattern samples, both with and without protective coatings. In the absence of a coating (Fig. 2, *a*), the initial wetting angle upon application of the binder ranged from 20° to 40°, while after a 5-minute holding period, it decreased to θ = 2÷13° [21]. The presence of polyvinyl alcohol and dimethylglyoxime additives in the pattern composition resulted in higher values of θ.

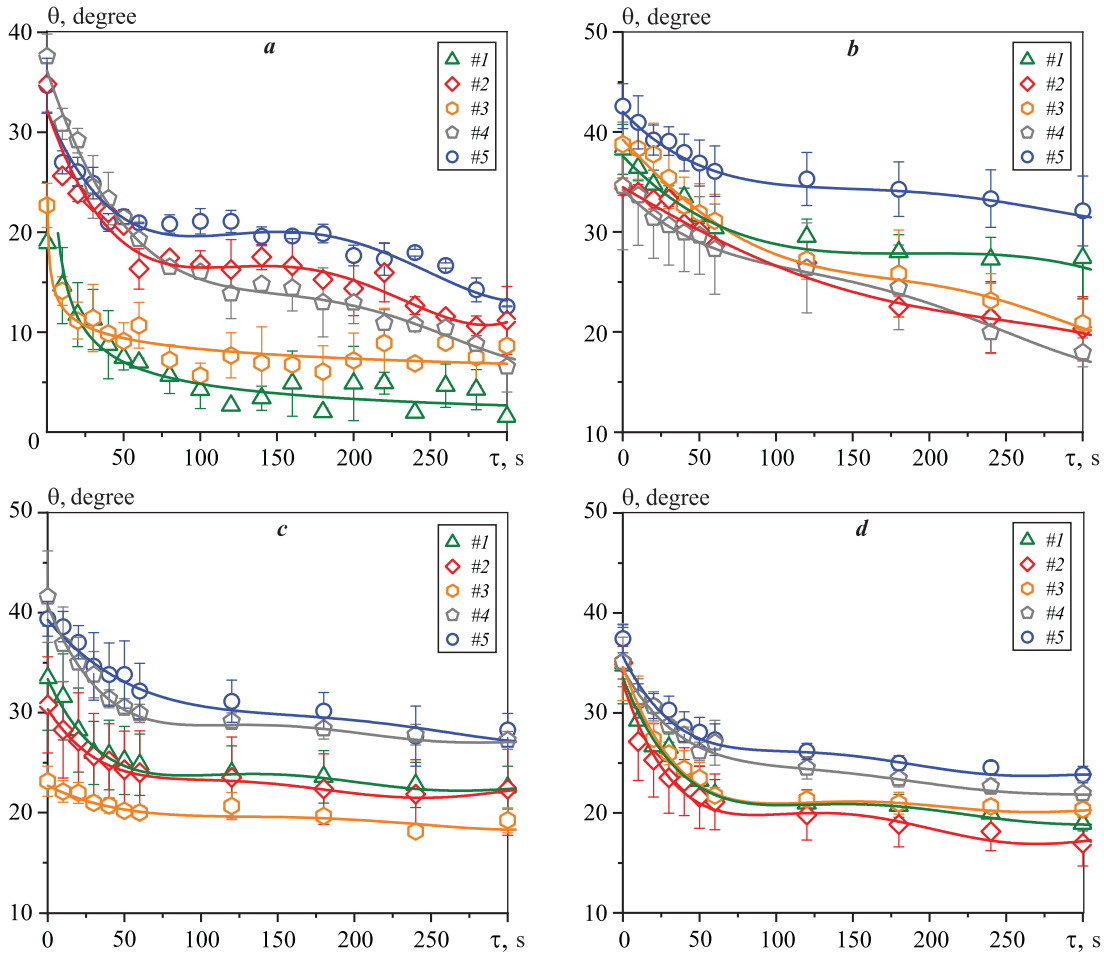

Fig. 2. Wetting angle with colloidal silica binder of the surface of pattern samples without coating (***a***) [21] and with coatings #Wax (***b***), #Varnish (***c***) and #Varnish + Rosin (***d***) (Table 2) as a function of time for pattern compounds *#1–#5*

#1 – 98 % urea + 2 % magnesium sulfate; *#2* – 96 % urea + 2 % magnesium sulfate + 2 % polyvinyl alcohol;
#3 – 90 % urea + 10 % potassium nitrate; *#4* – 88 % urea + 10 % potassium nitrate + 2 % polyvinyl alcohol;
#5 – 88 % urea + 10 % potassium nitrate + 2 % dimethylglyoxime

Рис. 2. Краевой угол смачивания (θ) водным связующим поверхности образцов модельных масс без покрытия (***a***) [21] и с покрытиями #В (***b***), #Л (***c***), #Л + К (***d***) (см. табл. 2) в зависимости от времени (τ) для модельных составов *#1–#5*

#1 – 98 % карбамида + 2 % сульфата магния; *#2* – 96 % карбамида + 2 % сульфата магния + 2 % поливинилового спирта;
#3 – 90 % карбамида + 10 % нитрата калия; *#4* – 88 % карбамида + 10 % нитрата калия + 2 % поливинилового спирта;
#5 – 88 % карбамида + 10 % нитрата калия + 2 % диметилглиоксима

Fig. 2, *b* presents the wetting angle values for the same pattern compositions but after the application of the wax-based protective coating. The initial values of θ immediately after applying the binder drop to samples coated with #W ranged from 35° to 43°, which is quite close to the values obtained for uncoated pattern compounds. However, it can be observed that during further holding of the droplet on the sample surface, the reduction in the wetting angle is not as significant compared to the case without a coating. Similar results were previously reported in [22], indicating that the intensity of interaction between the pattern compound and the binder decreases after the application of wax-based coatings. It is likely that when coating #W is applied and the solvent subsequently evaporates, the coating does not fully cover the sample surface, leading to localized dissolution of the pattern material. It should be noted that the composition of the pattern compound also affects the wetting angle, with the highest values of θ observed for the composition containing dimethylglyoxime. This additive reduces the hygroscopicity of the pattern compound and thus increases the wetting angle. Regarding other compositions, the values of θ after the application of coating #W range from 17° to 27°, which is fairly consistent across different formulations. In this case, no significant effect of polyvinyl alcohol on increasing the wetting angle was detected.

Fig. 2, *c* presents the wetting angle values after applying the varnish coating on the pattern samples. It can be observed that the initial values immediately after applying the binder drop are approximately 41° for compositions *#4* and *#5*, around 32° for compositions *#1* and *#2*, and about 23° for composition *#3*. Thus, the lowest wetting angle is observed for the pattern compound that contains only potassium nitrate. Compounds containing magnesium sulfate exhibit slightly higher θ values, and addition of polyvinyl alcohol having no significant impact on the wetting angle. The highest wetting angle is achieved for compounds containing potassium nitrate, polyvinyl alcohol, and dimethylglyoxime. The influence of polyvinyl alcohol on the wetting angle is attributed to its ability to reduce the hygroscopicity of the pattern compound. Previous studies have shown that samples made from pattern compound *#3* exhibit the highest surface roughness [21]. This is likely due to differences in the structure of the pattern compounds after solidification, which can lead to variations in the formation of the coating layer on their surface. In the case of varnish coating application, the wetting angle changes slightly over the holding period, decreasing by 4—15° after a 5-minute exposure. The slight reduction in wetting angle over time, as well as the influence of the pattern composition on its value, may indicate both coating integrity issues and interactions between the coating and the binder. The application of an additional rosin layer on top of the varnish coating (Fig. 2, *d*) results in an initial wetting angle that is independent of the pattern compound composition, with an average value of approximately 35°. Over time, the wetting angle values exhibit a trend similar to that observed for varnish coatings alone. This behavior can be attributed to the fact that, at the initial stage after the binder droplet is applied, the wetting angle is primarily determined by the interaction between the binder and the rosin layer. Over time, degradation of the rosin layer occurs, leading to interaction between the binder and the underlying varnish coating. On average, for all pattern compounds, the wetting angle values range from 17° to 23°.

In addition to the wetting angle, the spreading area (*S*) of the binder on the surface of the pattern samples can be used to evaluate the protective properties of the coatings. Fig. 3 presents the spreading area of the binder on the surfaces of the tested pattern compounds with different coating options after 2 h (once the binder had fully dried). The maximum spreading area of 170—180 mm^2 was observed for urea-based pattern compounds with polyvinyl alcohol additives (*#2* and *#4*) coated with the repair wax-based protective coating. A relatively high spreading area of $S = 140$ mm^2 was also obtained for the pattern compound containing magnesium sulfate (*#1*) with the wax-based coating. Considering the high values of error bars, it can be stated that for all pattern compounds coated with varnish or varnish with rosin, the spreading area of the binder ranged from 90 to 130 mm^2. Overall, the obtained *S* values confirm the conclusions drawn from the analysis of wetting angles, indicating that varnish-based coatings, unlike wax-based coatings, provide better protective properties. The wetting angle values and spreading areas are primarily determined by the protective properties of the coatings themselves rather than the pattern compositions.

It should also be noted that when examining the influence of various coatings on the spreading area of the binder across different pattern compounds, the minimum *S* values (along with the maximum wetting angle values θ) were observed for samples containing dimethylglyoxime (compound *#5*). As previously mentioned, this additive significantly reduces the hygroscopicity of the pattern compound.

Based on the results of wetting angle and spreading area measurements of the binders, two pattern

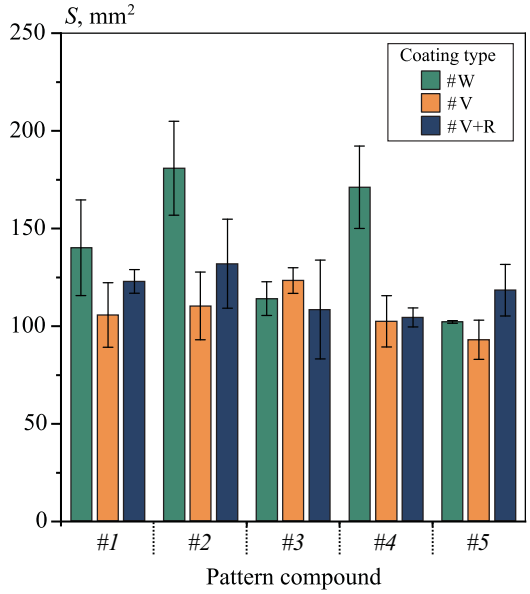

Fig. 3. Spreading area of the colloidal silica binder on the surface of pattern compound samples with coatings #W, #V and #V + R (see Table 2) after a 2-hour holding period for pattern compounds *#1–#5*

#1 – 98 % urea + 2 % magnesium sulfate;
#2 – 96% urea + 2 % magnesium sulfate + 2 % polyvinyl alcohol;
#3 – 90 % urea + 10 % potassium nitrate;
#4 – 88 % urea + 10 % potassium nitrate + 2 % polyvinyl alcohol;
#5 – 88 % urea + 10 % potassium nitrate + 2 % dimethylglyoxime

Рис. 3. Площадь растекания водного связующего на поверхности образцов модельных масс с покрытиями #В, #Л и #Л + К (см. табл. 2) после выдержки 2 ч для модельных составов *#1–#5*

#1 – 98 % карбамида + 2 % сульфата магния;
#2 – 96 % карбамида + 2 % сульфата магния + 2 % поливинилового спирта;
#3 – 90 % карбамида + 10 % нитрата калия;
#4 – 88 % карбамида + 10 % нитрата калия + 2 % поливинилового спирта;
#5 – 88 % карбамида + 10 % нитрата калия + 2 % диметилглиоксима

compounds were selected for further investigation: *#2* (96 % urea + 2 % magnesium sulfate + 2 % polyvinyl alcohol) and *#5* (88 % urea + 10 % potassium nitrate + + 2 % dimethylglyoxime). Fig. 4 presents photographs of ceramic molds produced using pattern compounds *#2* and *#5* with repair wax-based and varnish-based coatings at different stages of production.

When applying the first two ceramic layers to the pattern made from compound *#2* with the repair wax-based coating, minor sagging was observed (Fig. 4, *a*). The study of the wetting angle and spreading area of the binder on the pattern composition revealed that in cases of significant interaction between the binder and the pattern compound, simultaneous dissolution of the pattern occurs, forming indentations in the sample, while binder crystals grow at the pattern—binder in-

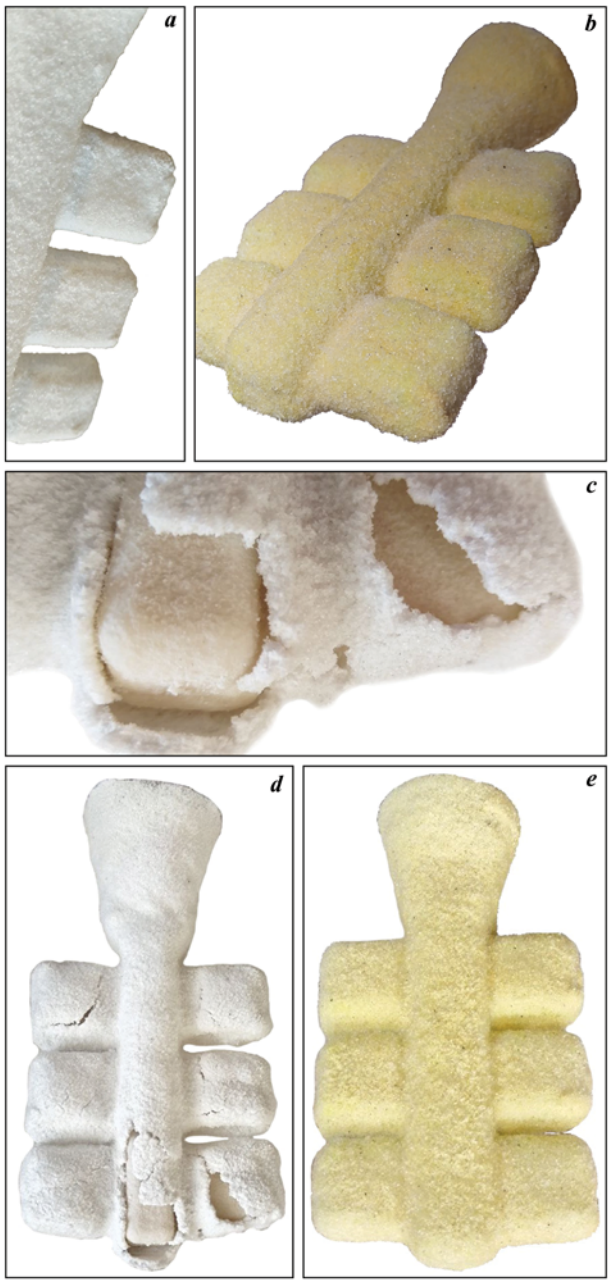

Fig. 4. Photographs of ceramic molds produced using various pattern compounds and protective coatings

a, ***b*** – pattern compound #2 (96 % urea + 2 % magnesium sulfate + + 2 % polyvinyl alcohol) repair wax-based coating #W, 2 layers (***a***) and 7 layers (***b***);
c–e – pattern compound #5 (88 % urea + 10 % potassium nitrate + + 2 % dimethylglyoxime) with a repair wax-based coating #W, 2 layers (***c***, ***d***), and varnish-based coating #V, 7 layers (***e***)

Рис. 4. Фотографии керамических форм, полученных с использованием различных модельных масс и защитных покрытий

a, ***b*** – модельный состав *#2* (96 % карбамида + 2 % сульфата магния + 2 % поливинилового спирта) с покрытием на основе ремонтного воска (#В) в 2 слоя (***a***) и 7 слоев (***b***);
c–e – модельный состав *#5* (88 % карбамида + 10 % нитрата калия + 2 % диметилглиоксима) с покрытием на основе ремонтного воска (#В) в 2 слоя (***c***, ***d***) и лака (#Л) в 7 слоев (***e***)

terface. Large crystals of the pattern compound extend beyond the original sample boundaries, likely contributing to sagging formation due to the insufficient protective properties of the coating. This partial dissolution of the pattern compound, accompanied by crystal growth, pushes the ceramic layer outward. Despite this issue, all seven ceramic layers were successfully applied to the pattern. The final appearance of the mold is shown in Fig. 4, *b*.

In the case of pattern compound *#5* containing dimethylglyoxime and coated with a repair wax-based protective layer (#W), the application of the first cera-

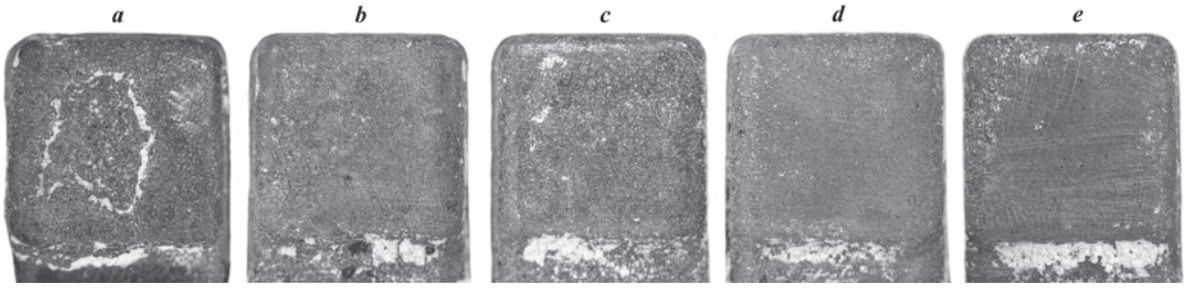

Fig. 5. Surface photographs of cast samples produced in ceramic molds using pattern compounds *#2* (***a***–***c***) and *#5* (***d***, ***e***) with protective coatings based on repair wax #W (***a***), varnish #V (***b***, ***d***), and varnish with rosin #V + R (***c***, ***e***)

#2 – 96 % urea + 2 % magnesium sulfate + 2 % polyvinyl alcohol;
#5 – 88 % urea + 10 % potassium nitrate + 2 % dimethylglyoxime

Рис. 5. Фотографии поверхности отлитых образцов, полученных в керамических формах с использованием модельных масс *#2* (***a***–***c***) и *#5* (***d***, **e**) с защитными покрытиями на основе ремонтного воска #В (***a***), лака #Л (***b***, ***d***) и лака с канифолью #Л + К (***c***, ***e***)

#2 – 96 % карбамида + 2 % сульфата магния + 2 % поливинилового спирта;
#5 – 88 % карбамида + 10 % нитрата калия + 2 % диметилглиоксима

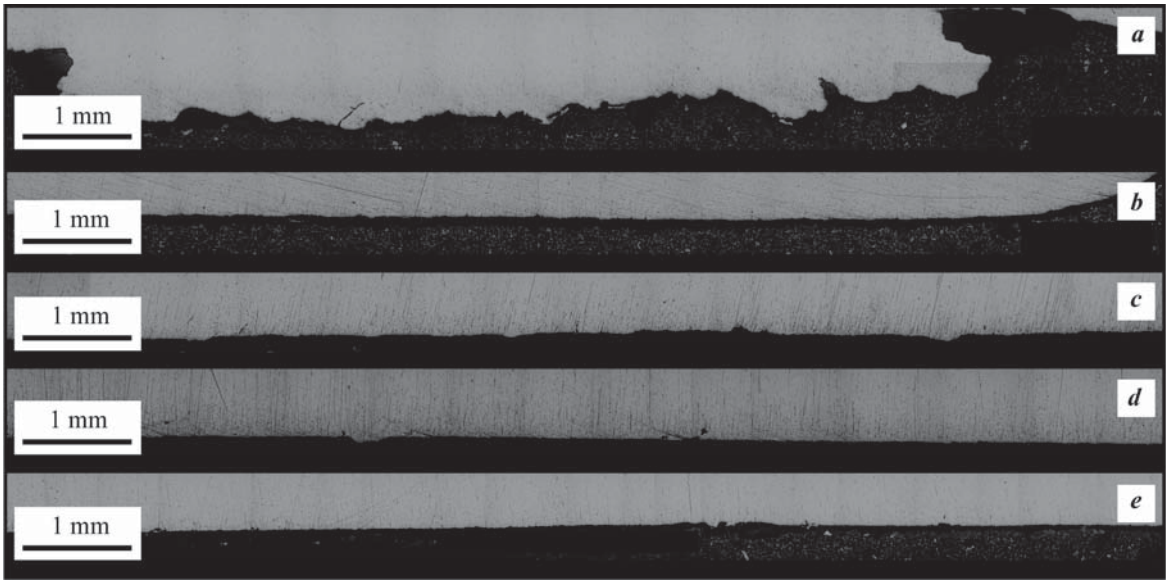

Fig. 6. Microstructure (OM) of cross-sectioned as-cast samples produced in ceramic molds using pattern compounds *#2* (***a***–***c***) and *#5* (***d***, ***e***) with protective coatings based on repair wax #W (***a***), Varnish #V (***b***, ***d***), and Varnish with Rosin #V + R (***c***, ***e***)

#2 – 96 % urea + 2 % magnesium sulfate + 2 % polyvinyl alcohol;
#5 – 88 % urea + 10 % potassium nitrate + 2 % dimethylglyoxime

Рис. 6. Микроструктура (ОМ) шлифов (поперечное сечение) отлитых образцов, полученных в керамических формах с использованием модельных масс *#2* (***a***–***c***) и *#5* (***d***, ***e***) с защитными покрытиями на основе ремонтного воска #В (***a***), лака #Л (***b***, ***d***) и лака с канифолью #Л + К (***c***, ***e***)

#2 – 96 % карбамида + 2 % сульфата магния + 2 % поливинилового спирта;
#5 – 88 % карбамида + 10 % нитрата калия + 2 % диметилглиоксима

mic layers resulted in cracking and destruction. Figs. 4, *c* and 4, *d* clearly show that under the cracked ceramic layer, the pattern surface exhibits significant roughness, which was not present before the ceramic application—indicating interaction between the pattern and the binder. The causes of destruction in this case are similar to those previously described for the pattern compound *#2* with the repair wax-based coating. Regarding varnish-based coatings (#V) and varnish with rosin (#V + R), no sagging was observed in any case, and high-quality ceramic molds were successfully obtained for both pattern compounds *#2* and *#5*. An example of a high-quality mold produced using the pattern compound with dimethylglyoxime (*#5*) and coated with varnish (#V) is shown in Fig. 4, *e*.

Fig. 5 presents photographs of cast samples made of nickel superalloy poured into ceramic molds produced using pattern compounds *#2* and *#5* with protective coatings based on repair wax, varnish, and varnish with rosin. As previously mentioned, it was not possible to produce a mold using pattern compound *#5* containing dimethylglyoxime and a repair wax-based coating (#W). Although the mold produced with pattern compound *#2*, containing magnesium sulfate and polyvinyl alcohol, and coated with repair wax did not fail structurally, the surface of the cast samples exhibited penetration defects (Fig. 5, *a*). These defects formed due to the destruction of the ceramic surface layer and infiltration of the molten alloy into the damaged layer. Previous observations (see Fig. 4, *a*) showed the presence of localized bulging of the shell during mold layer formation. Regarding the samples coated with varnish (#V) and varnish with rosin (#V + R) (Fig. 5, *b*—*e*), it can be observed that all sample surfaces are free of defects, confirming the high protective properties of the varnish coatings.

Fig. 6 shows cross-sectional micrographs of the samples presented in Fig. 5. It can be observed that the thickness of the burn-on defect in the sample produced using pattern compound *#2*, coated with a repair wax-based protective layer (Fig. 6, *a*), is approximately 1 mm. The other samples, in which varnish-based coatings (#V) and varnish with rosin (#V + R) were used on the pattern compounds (Fig. 6, *b*—*e*), exhibit a minimal number of surface defects.

Fig. 7 presents the surface roughness values of the cast samples produced in ceramic molds using pattern compounds with magnesium sulfate and polyvinyl alcohol additives (*#2*), as well as potassium nitrate and dimethylglyoxime additives (*#5*), coated with protective coatings based on repair wax, varnish, and varnish with rosin. The minimum surface roughness value

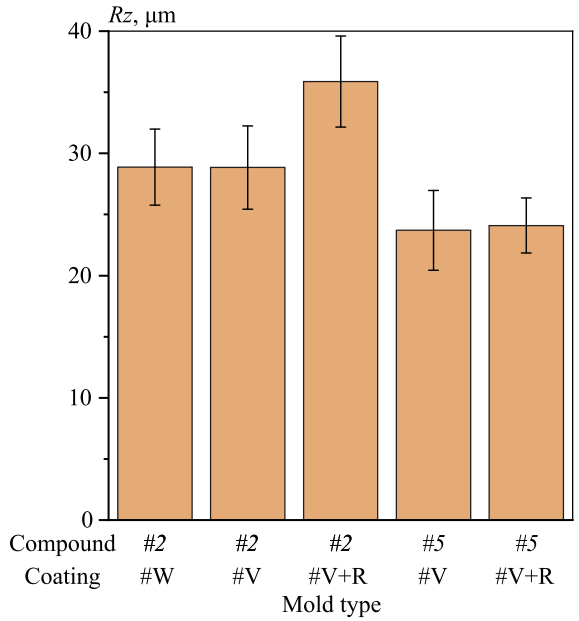

Fig. 7. Surface roughness of as-cast samples produced in ceramic molds using pattern compounds *#2* and *#5* with protective coatings based on repair wax (#W), varnish (#V) and varnish with rosin (#V + R)

#2 – 96 % urea + 2 % magnesium sulfate + 2 % polyvinyl alcohol;
#5 – 88 % urea + 10 % potassium nitrate + 2 % dimethylglyoxime

Рис. 7. Шероховатость поверхности отлитых образцов, полученных в керамических формах с использованием модельных масс *#2* и *#5* с защитными покрытиями на основе ремонтного воска (#В), лака (#Л) и лака с канифолью (#Л + К)

#2 – 96 % карбамида + 2 % сульфата магния + 2 % поливинилового спирта;
#5 – 88 % карбамида + 10 % нитрата калия + 2 % диметилглиоксима

(Rz = 24 μm) was obtained for the cast samples produced using pattern compound *#5* (with potassium nitrate and dimethylglyoxime) and the varnish-based coating. The use of the same coatings on pattern compound *#2*, containing magnesium sulfate and polyvinyl alcohol, resulted in slightly higher roughness values (Rz = 29÷36 μm). The cast sample produced using pattern compound *#2* with a repair wax-based coating demonstrated similar roughness, with Rz = 29 μm. In this case, the surface roughness was measured in areas free of burn-on defects. Thus, all protective coatings provide comparable surface roughness values in the range of Rz = 24÷36 μm. This is likely due to the fact that after pattern removal and mold burnout, no traces of the coating remain, and the surface roughness is entirely determined by the characteristics of the slurry and stucco used in ceramic mold production.

Fig. 8, *a* presents the SEM microstructure of a sample cast in a ceramic mold produced using pattern

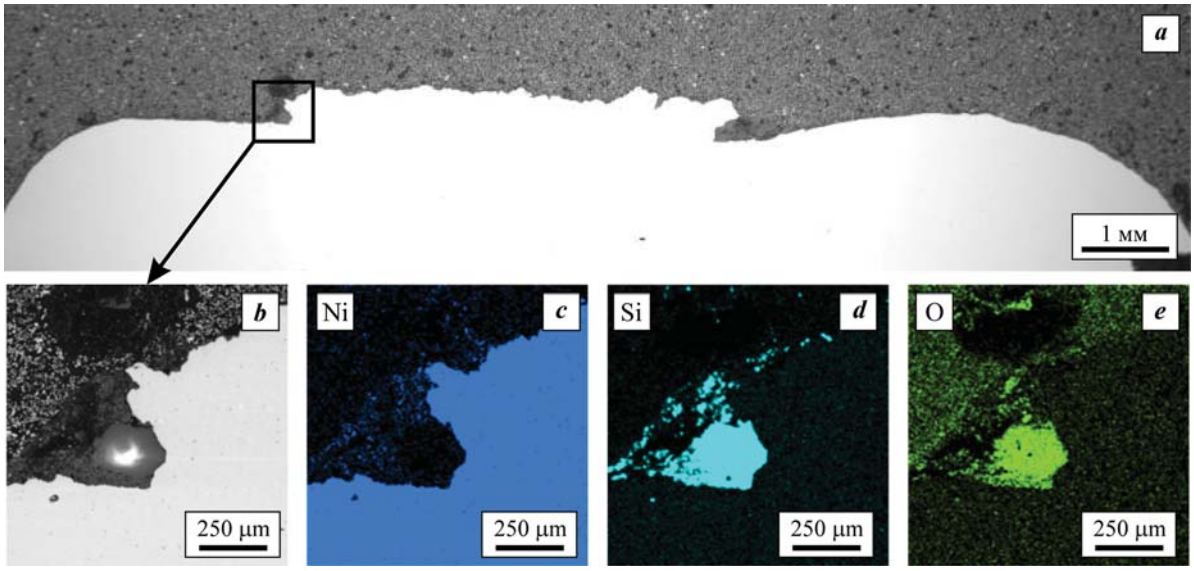

Fig. 8. Microstructure of the sample cast in a ceramic mold produced using pattern compound *#2* with a repair wax-based coating (#W) (***a***), magnified microstructure area (***b***), and elemental distribution maps of Ni (***c***), Si (***d***), and O (***e***)

Pattern composition *#2* – 96 % urea + 2 % magnesium sulfate + 2 % polyvinyl alcohol

Рис. 8. Микроструктура образца, отлитого в керамическую форму, полученную с использованием модельной массы *#2* с покрытием на основе ремонтного воска (#B) (***a***), увеличенный участок микроструктуры (***b***) и карты распределения Ni (***c***), Si (***d***), O (***e***)

Модельный состав *#2* – 96 % карбамида + 2 % сульфата магния + 2 % поливинилового спирта

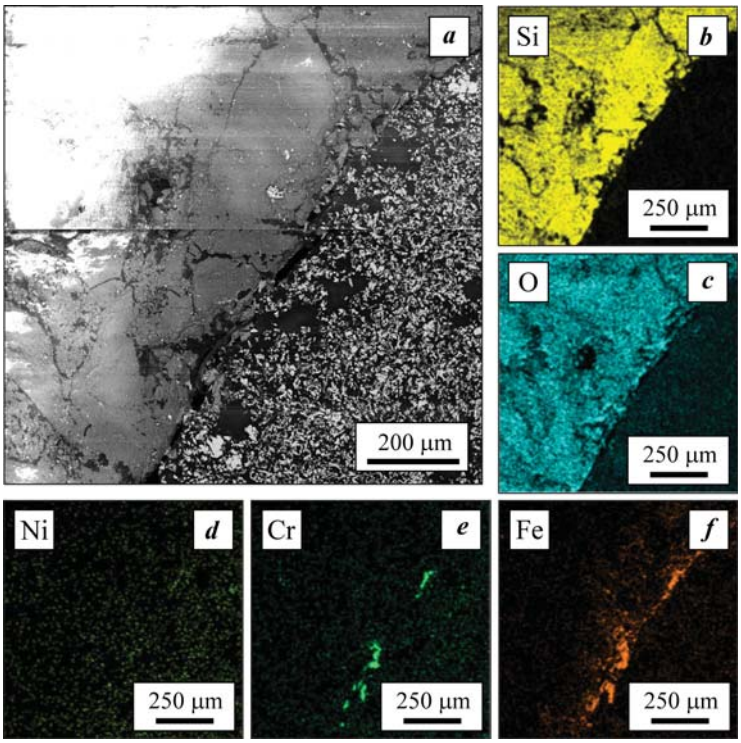

Fig. 9. Microstructure of the contact layer of the ceramic mold produced using pattern compound *#5* coated with varnish (#V) after alloy pouring (***a***) and EDS maps of Si (***b***), O (***c***), Ni (***d***), Cr (***e***), Fe (***f***)

Pattern composition *#5* – 88 % urea + 10 % potassium nitrate + 2 % dimethylglyoxime

Рис. 9. Микроструктура контактного слоя керамической формы, полученной с использованием модельной массы *#5* с покрытием на основе лака (#Л), после заливки сплава (***a***) и карты распределения Si (***b***), O (***c***), Ni (***d***), Cr (***e***), Fe (***f***)

Модельный состав *#5* – 88 % карбамида + 10 % нитрата калия + 2 % диметилглиоксима

compound *#2* (96 % urea + 2 % magnesium sulfate + + 2 % polyvinyl alcohol) with a repair wax-based coating. It can be observed that at the transition zone between the high-quality surface and the burn-on defect, undercuts are present. The microstructure of such an undercut at a higher magnification, along with the EDS maps for this area, is shown in Fig. 8, *b*—*e*. The results of EDS analysis reveal the presence of particles containing Si and O within the undercuts. Thus, it can be assumed that these are stucco particles from the ceramic mold that detached from the mold during the casting removal process. This confirms the assumption that the previously observed sagging during mold formation occurs due to the delamination of ceramic layers.

For chemically active melts, it is essential to evaluate their interaction with mold materials. Fig. 9, *a* presents the microstructure of the contact layer in a cross-section of the ceramic mold surface produced using pattern compound *#5* (88 % urea + + 10 % potassium nitrate + 2 % dimethylglyoxime) with a varnish-based coating (#V). According to the elemental distribution maps of Si and O (Fig. 9, *b* and *c*), the ceramic mold has a well-defined boundary. A layer enriched with Cr and Fe (Fig. 9, *e* and *f*), with a thickness of no more than 50 μm, is present on its surface. It should be noted that this layer is not continuous, which may be attributed to its insufficient strength and partial destruction during the preparation of the metallographic specimen. It is known that chromium has high vapor elasticity and, upon pouring, deposits on the mold surface while interacting with atmospheric oxygen. Thus, no signs of interaction between the melt and the mold have been detected. As previously mentioned, the applied coatings are completely removed during the burnout of the ceramic mold.

The results of laser scanning of the cast samples produced in ceramic molds using pattern compounds with magnesium sulfate and polyvinyl alcohol additives (*#2*), as well as potassium nitrate and dimethylglyoxime additives (*#5*), coated with protective coatings based on repair wax, varnish, and varnish with rosin, are presented in Fig. 10. It is evident that when using the repair wax-based coating (#W), the dimensional deviations in the positive direction reach up to 2.5 mm (Fig. 10, *a*). These deviations are attributed to the formation of sagging, which resulted from changes in the mold geometry during the application of the initial ceramic layers.

Unfortunately, it is not possible to determine the effect of the coating on dimensional accuracy, as producing a mold using a urea-based pattern compound and a colloidal silica binder slurry without a protective coating is not feasible. However, considering the thin protective layer (less than 100 μm), it is unlikely that the coating significantly affects the dimensional accuracy of the castings.

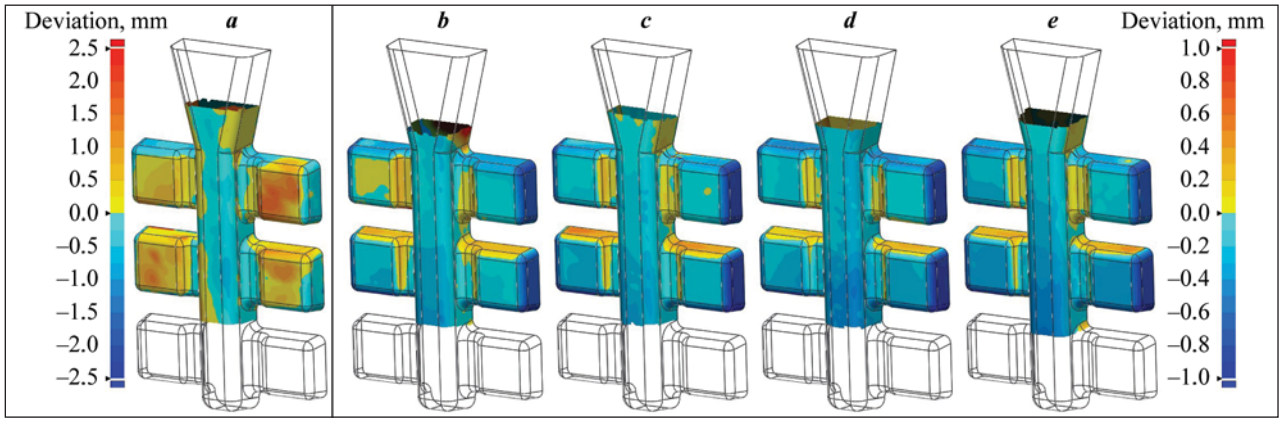

Fig. 10. Dimensional deviations of as-cast samples produced in ceramic molds using pattern compounds *#2* (***a***—***c***) and *#5* (***d***, ***e***) with coatings based on repair wax #W (***a***), varnish #V (***b***, ***d***), and varnish with rosin #V + R (***c***, ***e***)

#2 – 96 % urea + 2 % magnesium sulfate + 2 % polyvinyl alcohol;
#5 – 88 % urea + 10 % potassium nitrate + 2 % dimethylglyoxime

Рис. 10. Отклонения размеров отлитых образцов, полученных в керамических формах с использованием модельных масс *#2* (***a***—***c***) и *#5* (***d***, ***e***) с защитными покрытиями на основе ремонтного воска #В (***a***), лака #Л (***b***, ***d***) и лака с канифолью #Л + К (***c***, ***e***)

#2 – 96 % карбамида + 2 % сульфата магния + 2 % поливинилового спирта;
#5 – 88 % карбамида + 10 % нитрата калия + 2 % диметилглиоксима

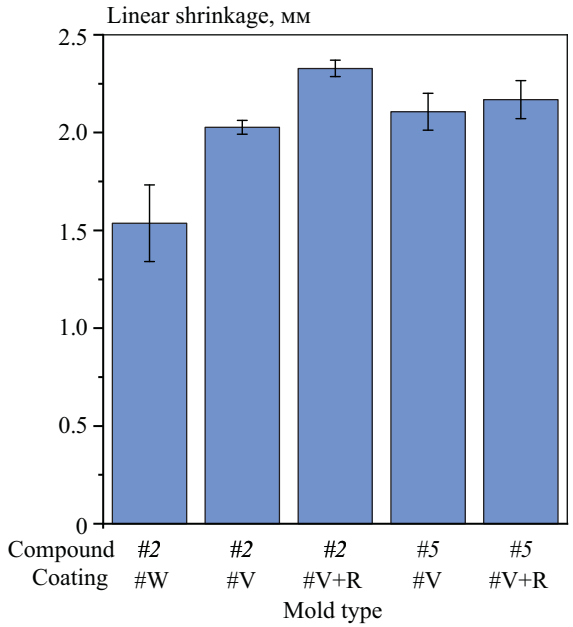

Fig. 11. Linear shrinkage of as-cast samples produced in ceramic molds using pattern compounds *#2* and *#5* with protective coatings based on repair wax (#W), varnish (#V), and varnish with rosin (#V + R)

#2 – 96 % urea + 2 % magnesium sulfate + 2 % polyvinyl alcohol;
#5 – 88 % urea + 10 % potassium nitrate + 2 % dimethylglyoxime

Рис. 11. Линейная усадка отлитых образцов, полученных в керамических формах с использованием модельных масс *#2* и *#5* с защитными покрытиями на основе ремонтного воска (#В), лака (#Л) и лака с канифолью (#Л + К)

#2 – 96 % карбамида + 2 % сульфата магния + 2 % поливинилового спирта;
#5 – 88 % карбамида + 10 % нитрата калия + 2 % диметилглиоксима

The results of laser scanning of the cast samples were used to determine their linear shrinkage. Fig. 11 presents the results of the linear shrinkage measurements for the cast samples produced in ceramic molds using pattern compounds with magnesium sulfate and polyvinyl alcohol additives (*#2*), as well as potassium nitrate and dimethylglyoxime additives (*#5*), coated with protective coatings based on repair wax, varnish, and varnish with rosin. When using the repair wax-based coating (#W), the linear shrinkage was only 1.5 %, whereas for the varnish-based coatings (#V and #V + R), the shrinkage ranged from 2.0 % to 2.3 %. The low shrinkage observed with the repair wax coating (#W) is attributed to delamination and sagging that occurred during the application of the initial mold layers. In [21], it was shown that the linear shrinkage of pattern compounds *#2* and *#5* is 0.55 % and 0.3 %, respectively. However, it is challenging to observe a significant difference in the total shrinkage of the cast samples depending on the applied pattern compound composition. Overall, it can be concluded that the total shrinkage of the ceramic mold and the alloy itself is, on average, ~1.7 %, which is almost identical to the shrinkage characteristic of ceramic molds produced using hydrolyzed ethyl silicate solution, as well as colloidal silica binders, but with wax patterns.

Large-sized castings of the “Outer Casing” and “Inner Casing” components made of the heat-resistant nickel alloy were produced under industrial conditions at PJSC “UEC-Kuznetsov” (Samara, Russia). Water-soluble patterns made of a urea-based pattern compound with a hydrophobic protective coating based on varnish with rosin were used for the production of the castings. The maximum overall dimension of the produced castings reached 1136 mm. The use of the protective coating #V + R made it possible to produce shell molds using a slurry prepared with a colloidal silica binder, achieving results comparable to those obtained using the traditional technology based on hydrolyzed ethyl silicate as the binder. The resulting castings met the technical requirements in terms of dimensional accuracy and mechanical properties.

Conclusions

1. The wetting angle of the colloidal silica binder on the surface of the tested pattern compounds increased from 3—15° to 20—30° when applying protective coatings based on repair wax, varnish, and varnish with rosin. However, no significant influence of the coating type on the wetting angle was observed. In all cases (with and without coatings), the highest θ value was obtained for the pattern compounds containing dimethylglyoxime.

2. The minimum spreading area of 90—130 mm^2, corresponding to minimal interaction between the binder and the pattern compound, was achieved using varnish-based coatings, as well as varnish with rosin. In the case of repair wax-based coatings, the spreading area was 170—180 mm^2. The modification of the pattern compound with various additives, in all likelihood, does not have a significant impact on the spreading area of the colloidal silica binder on the surface of the pattern compound samples.

3. The use of repair wax-based protective coatings in the production of ceramic molds with colloidal silica binder resulted in sagging and cracking, which prevented the successful fabrication of molds with pattern compound *#5* containing dimethylglyoxime. The mold produced using pattern compound *#2* (with magnesium sulfate and polyvinyl alcohol additives)

was successfully fabricated; however, partial destruction of the inner mold surface and sagging were observed. Molds coated with varnish and varnish with rosin exhibited no visible defects or manufacturing issues.

4. The castings produced in the ceramic molds with varnish and varnish with rosin as protective coatings on the patterns exhibited no visible defects and had a surface roughness of $Rz = 25 \div 35$ μm. The casting obtained in the mold with a repair wax-based protective coating showed mechanical penetration defects, with ceramic mold particles detected within the casting. Additionally, it exhibited significant dimensional deviations due to sagging caused by the degradation of the inner mold surface.

5. The linear shrinkage of the castings produced using molds with varnish and varnish with rosin coatings on the patterns was higher compared to those with repair wax-based coatings. This was also associated with the formation of bubbles and sagging on the pattern surface during the mold layer formation process.

References

1. Kanyo J.E., Schafföner S., Uwanyuze R.S., Leary K.S. An overview of ceramic molds for investment casting of nickel superalloys. *Journal of the European Ceramic Society.* 2020;40(15):4955—4973. https://doi.org/10.1016/j.jeurceramsoc.2020.07.013
2. Selvaraj S.K., Sundaramali G., Dev S.J., Swathish R.S., Karthikeyan R., Vishaal K.E.V., Paramasivam V. Recent advancements in the field of Ni-based superalloys. *Advances in Materials Science and Engineering.* 2021;Dec.2021:9723450. https://doi.org/10.1155/2021/9723450
3. Kumar S., Karunakar D.B. Development of wax blend pattern and optimization of injection process parameters by grey-fuzzy logic in investment casting process. *International Journal of Metalcasting.* 2022;16: 962—972. https://doi.org/10.1007/s40962-021-00655-y
4. Pradyumna R., Sridhar S., Satyanarayana A., Chauhan A.S., Baig M.A.H. Wax patterns for integrally cast rotors/stators of aeroengine gas turbines. *Materials Today: Proceedings.* 2015;2(4—5):1714—1722. https://doi.org/10.1016/j.matpr.2015.07.005
5. Prokopchuk N.R., Gorshcharik N.D., Klyuev A.Yu., Kozlov N.G., Rozhkova E.I., Latyshevich I.A., Bakovich N.A. Pattern compounds for high precision casting. *Izvestiya Natsional'noi akademii nauk Belarusi. Seriya khimicheskikh nauk*. 2015;4:122—128. (In Russ.).
Прокопчук Н.Р., Горщарик Н.Д., Клюев А.Ю., Козлов Н.Г., Рожкова Е.И., Латышевич И.А., Баковач Н.А. Модельные составы для точного литья. *Известия Национальной академии наук Беларуси. Серия химических наук.* 2015;4:122—128.
6. Dubrovskii V.A. Investment casting pattern compound: Patent 2123902 (RF). 1997. (In Russ.).
Дубровский В.А. Модельная композиция для выплавляемых моделей: Патент 2123902 (РФ). 1997.
7. Uskov D.I. Core composition for obtaining precision castings. In: *Youth and science:* Proceedings of the X Anniversary National Scientific and Technical Conference of students, graduate students and young scientists with international participation, dedicated to the 80th anniversary of the formation of the Krasnoyarsk region (15–25 April 2014). Krasnoyarsk: SFU, 2014. P. 1–4. (In Russ.).
Усков Д.И. Стержневой состав для получения прецизионных отливок. В сб: *Молодежь и наука:* Материалы X Юбилейной Всеросс. науч.-техн. конференции студентов, аспирантов и молодых ученых с междунар. участием, посвященной 80-летию образования Красноярского края (15—25 апреля 2014 г.). Красноярск: СФУ, 2014. С. 1—4.
8. Gromakov A.I., Mikhnev M.M., Uskov D.I. Compound for the manufacture of water-soluble cores. In: *Proceedings of the International Scientific Conference "Reshetnev Readings"* (9–12 November 2016). Krasnoyarsk: Sibirskii gosudarstvennyi universitet nauki i tekhnologii imeni akademika M.F. Reshetneva, 2016. Vol. 2. P. 332–333. (In Russ.).
Громаков А.И., Михнев М.М., Усков Д.И. Смесь для изготовления водорастворимых стержней. В сб: *Материалы Международной научной конференции «Решетневские чтения»* (9—12 ноября 2016 г.). Красноярск: Сибирский государственный университет науки и технологий им. академика М.Ф. Решетнева, 2016. Т. 2. С. 332—333.
9. Fujitta T. Pattern material for making foundry patterns for use in investments casting process: Patent 4939187 (USA). 1990.
10. Stadnichuk V.I. A method of manufacturing ceramic molds using soluble patterns: Patent 2499651 (RF). 2012. (In Russ.).
Стадничук В.И. Способ изготовления керамических форм по растворяемым моделям: Патент 2499651 (РФ). 2012.
11. Lakeev A.S., Shcheglovitov L.A., Kuz'min Yu.D. Progressive methods of manufacturing high precision castings. Kiev: Tekhnika, 1984. 160 p. (In Russ.).

Лакеев А.С., Щегловитов Л.А., Кузьмин Ю.Д. Прогрессивные способы изготовления точных отливок. Киев: Техника, 1984. 160 с.

12. Sumin E.I., Andrianov L.P. Composition for making water-soluble patterns: Author's certificate 602288 (USSR). 1976. (In Russ.).
Сумин Е.И., Андрианов Л.П. Композиция для изготовления водорастворимых моделей: Авт. св-во 602288 (СССР). 1976.
13. Seyedraoufi Z.S., Mirdamadi Sh. Synthesis, microstructure and mechanical properties of porous Mg—Zn scaffolds. *Journal of the Mechanical Behavior of Biomedical Materials*. 2013;21:1—8. https://doi.org/10.1016/j.jmbbm.2013.01.023
14. Wen C.E., Yamada Y., Shimojima K., Chino Y., Hosokawa H., Mabuchi M. Compressibility of porous magnesium foam: dependency on porosity and pore. *Materials Letters*. 2004;58(3—4):357—360. https://doi.org/10.1016/S0167-577X(03)00500-7
15. Hao G.L., Han F.S., Li W.D. Processing and mechanical properties of magnesium foams. *Journal of Porous Materials*. 2009;16:251—256. https://doi.org/10.1007/s10934-008-9194-y
16. Marutani Y., Kamitani T. Manufacturing sacrificial patterns for casting by salt powder lamination. *Rapid Prototyping Journal*. 2004;10(5):281—287. https://doi.org/10.1108/13552540410562313
17. Rutto H.K. Urea-based moulding compounds for investment casting: Thesis for the degree Philosophiae Doctor in Chemical Engineering. Pretoria: University of Pretoria, 2006.
18. Investment casting. Eds. Ya.I. Shklennik, V.A. Ozerov. 2-nd ed., rev. and supl. Moscow: Mashinostroenie, 1971. 436 p. (In Russ.).
Литье по выплавляемым моделями. Под ред. Я.И. Шкленника, В.А. Озерова. 2-е изд., перераб. и доп. М.: Машиностроение, 1971. 436 с.
19. Churkin B.S., Churkin A.B., Kategorenko Yu.I. Special casting methods. Ekaterinburg: Ross. gos. prof.-ped. un-t, 2012. 189 p. (In Russ.).
Чуркин Б.С., Чуркин А.Б., Категоренко Ю.И. Специальные способы литья: Учеб.-метод. пос. Екатеринбург: Изд-во Рос. гос. проф.-пед. ун-та, 2012. 189 с.
20. Rutto H., Focke W. Thermomechanical properties of urea-based pattern molding compounds for investment casting. *International Polymer Processing*. 2010;25(1): 15—22. https://doi.org/10.3139/217.2256
21. Bazhenov V.E., Kovyshkina E.P., Nikitina A.A., Koltygin A.V. Influence of various additives on the properties of salt water-soluble carbamide-based pattern compounds. *Tsvetnye metally*. 2024;8:82—90. (In Russ.). https://doi.org/10.17580/tsm.2024.08.12
Баженов В.Е., Ковышкина Е.П., Никитина А.А., Колтыгин А.В. Влияние различных добавок на свойства солевых водорастворимых модельных масс на основе карбамида. *Цветные металлы*. 2024;8:82—90. https://doi.org/10.17580/tsm.2024.08.12
22. Bazhenov V.E., Kovyshkina E.P., Koltygin A.V., Belov V.D., Dmitriev D.N. Development of isolating composition for soluble salt models for investment casting. *Liteinoe proizvodstvo*. 2023;(6):30—37. (In Russ.).
Баженов В.Е., Ковышкина Е.П., Колтыгин А.В., Белов В.Д., Дмитриев Д.Н. Разработка разделительного состава для растворяемых солевых моделей при литье по выплавляемым моделям. *Литейное производство*. 2023;(6):30—37.
23. Stadnichuk V.I., Bessmertnyi V.S. Formation of protective hydrophobic films on the working surface of foundry ceramic molds. *Ogneupory i tekhnicheskaya keramika*. 2011;(4—5):8—10. (In Russ.).
Стадничук В.И., Бессмертный В.С. Формирование защитных гидрофобных пленок на рабочей поверхности литейных керамических форм. *Огнеупоры и техническая керамика*. 2011;(4—5):8—10.
24. Karanik Yu.A. Method of production of castings from ferrous and non-ferrous metals: Patent 2048955 (RF). 1995. (In Russ.).
Караник Ю.А. Способ изготовления отливок из черных и цветных металлов: Патент 2048955 (РФ). 1995.
25. Vasin Yu.P., Evseeva T.M., Lonzinger V.A., Aver'yanov E.F., Sezganov A.N., Rozovskii L.D., Khokhlova E.V. Method of making molds for investment casting: Author's certificate 1310098 (RF). 1985. (In Russ.).
Васин Ю.П., Евсеева Т.М., Лонзингер В.А., Аверьянов Е.Ф., Сезганов А.Н., Розовский Л.Д., Хохлова Е.В. Способ изготовления форм при литье по выплавляемым моделям: Авт. св-во 1310098 (РФ). 1985.
26. Koltygin A.V., Belov V.D., Bazhenov V.E., Kovyshkina E.P., Fadeev A.V. Solution for improving surface wetting of wax investment casting patterns: Patent application 2023110773 (RF). 2023. (In Russ.).
Колтыгин А.В., Белов В.Д., Баженов В.Е., Ковышкина Е.П., Фадеев А.В. Раствор для улучшения смачивания поверхности восковых моделей для литья по выплавляемым моделям: Заявка на патент 2023110773 (РФ). 2023.
27. Bazhenov V.E., Kovyshkina E.P., Sannikov A.V., Kolty-

gin A.V., Ten D.V., Rizhsky A.A., Belov V.D., Lazarev E.A. Analysis of the slurry and ceramic properties for investment casting obtained with domestic colloidal silica binders. *Izvestiya. Non-Ferrous Metallurgy.* 2023;29(2):15—28. (In Russ.). https://doi.org/10.17073/0021-3438-2023-2-15-28

Баженов В.Е., Ковышкина Е.П., Санников А.В., Колтыгин А.В., Тен Д.В., Рижский А.А., Белов В.Д., Лазарев Е.А. Анализ свойств суспензии и керамики для литья по выплавляемым моделям, полученных на отечественных связующих на водной основе. *Известия вузов. Цветная металлургия*. 2023;29(2):15—28. https://doi.org/10.17073/0021-3438-2023-2-15-28

Information about the authors

Viacheslav E. Bazhenov – Cand. Sci. (Eng.), Assistant Prof., Department of Foundry Technologies and Material Art Working (FT&MAW), National University of Science and Technology "MISIS" (NUST MISIS).
https://orcid.org/0000-0003-3214-1935
E-mail: V.E.Bagenov@gmail.com

Elena P. Kovyshkina – Postgraduate Student, Department of FT&MAW, NUST MISIS.
https://orcid.org/0000-0001-8603-1630
E-mail: Kovyshkina@ic-ltm.ru

Anna A. Nikitina – Laboratory Assistant, Department of FT&MAW, NUST MISIS.
https://orcid.org/0000-0002-5399-0330
E-mail: nikitina.misis@gmail.com

Yuri V. Tselovalnik – Cand. Sci. (Eng.), Senior Lecturer, Department of FT&MAW, NUST MISIS.
https://orcid.org/0000-0001-9102-016X
E-mail: tselovalnikyuri@gmail.com

Anastasia A. Belova – Postgraduate Student, Department of FT&MAW, NUST MISIS.
https://orcid.org/0009-0008-4199-8942
E-mail: belova@ic-ltm.ru

Andrey V. Koltygin – Cand. Sci. (Eng.), Assistant Prof., Department of FT&MAW, NUST MISIS.
https://orcid.org/0000-0002-8376-0480
E-mail: misistlp@mail.ru

Vladimir D. Belov – Dr. Sci. (Eng.), Head of the Department of FT&MAW, NUST MISIS.
https://orcid.org/0000-0003-3607-8144
E-mail: vdbelov@mail.ru

Boris E. Hvatskov – Senior Expert of the Innovations Development Department of the General Constructor's Division, PJSC "UEC-Kuznetsov".
E-mail: be.hvatskov@uec-kuznetsov.ru

Информация об авторах

Вячеслав Евгеньевич Баженов – к.т.н., доцент кафедры литейных технологий и художественной обработки материалов (ЛТиХОМ) Национального исследовательского технологического университета «МИСИС» (НИТУ МИСИС).
https://orcid.org/0000-0003-3214-1935
E-mail: V.E.Bagenov@gmail.com

Елена Павловна Ковышкина – аспирант кафедры ЛТиХОМ, НИТУ МИСИС.
https://orcid.org/0000-0001-8603-1630
E-mail: Kovyshkina@ic-ltm.ru

Анна Андреевна Никитина – учебный мастер кафедры ЛТиХОМ, НИТУ МИСИС.
https://orcid.org/0000-0002-5399-0330
E-mail: nikitina.misis@gmail.com

Юрий Всеволодович Целовальник – к.т.н., ст. преподаватель кафедры ЛТиХОМ, НИТУ МИСИС.
https://orcid.org/0000-0001-9102-016X
E-mail: tselovalnikyuri@gmail.com

Анастасия Андреевна Белова – аспирант кафедры ЛТиХОМ, НИТУ МИСИС.
https://orcid.org/0009-0008-4199-8942
E-mail: belova@ic-ltm.ru

Андрей Вадимович Колтыгин – к.т.н., доцент кафедры ЛТиХОМ, НИТУ МИСИС.
https://orcid.org/0000-0002-8376-0480
E-mail: misistlp@mail.ru

Владимир Дмитриевич Белов – д.т.н., заведующий кафедрой ЛТиХОМ, НИТУ МИСИС.
https://orcid.org/0000-0003-3607-8144
E-mail: vdbelov@mail.ru

Борис Евгеньевич Хвацков – вед. специалист отдела инновационного развития службы генерального конструктора, ПАО «ОДК-Кузнецов».
E-mail: be.hvatskov@uec-kuznetsov.ru

Contribution of the authors

V.E. Bazhenov – development of the main concept, analysis of research results, and manuscript writing.

E.P. Kovyshkina – conducting experiments and analysis of research results.

A.A. Nikitina – conducting experiments and analysis of research results.

Yu.V. Tselovalnik – conducting experiments and analysis of research results.

A.A. Belova – conducting experiments and analysis of research results.

A.V. Koltygin – scientific supervision and manuscript editing.

V.D. Belov – general supervision and manuscript editing.

B.E. Hvatskov – defining the research objectives and tasks, and resource provision.

Вклад авторов

В.Е. Баженов – формирование основной концепции, обработка результатов исследований, написание текста статьи.

Е.П. Ковышкина – проведение экспериментов, обработка результатов исследований.

А.А. Никитина – проведение экспериментов, обработка результатов исследований.

Ю.В. Целовальник – проведение экспериментов, обработка результатов исследований.

А.А. Белова – проведение экспериментов, обработка результатов исследований.

А.В. Колтыгин – научное руководство, редактирование текста статьи.

В.Д. Белов – общее руководство, редактирование текста статьи.

Б.Е. Хвацков – формулировка цели и задачи исследований, обеспечение ресурсами.

The article was submitted 05.06.2024, revised 10.08.2024, accepted for publication 13.08.2024
Статья поступила в редакцию 05.06.2024, доработана 10.08.2024, подписана в печать 13.08.2024

UDC 669.715 : 539.89 : 539.4
https://doi.org/10.17073/0021-3438-2025-1-58-66

Research article
Научная статья

Effect of rotary forging on the structure and mechanical properties of two eutectic alloys of the Al–La and Al–Ca–La systems

V.A. Andreev[1], **M.V. Gorshenkov**[2], **E.A. Naumova**[2], **S.O. Rogachev**[1,2]

[1] **Baikov Institute of Metallurgy and Materials Science of the Russian Academy of Sciences**
49 Leninskiy Prosp., Moscow 119334, Russia

[2] **National University of Science and Technology "MISIS"**
1 Bld, 4 Leninskiy Prosp., Moscow 119049, Russia

✉ Stanislav O. Rogachev (csaap@mail.ru)

Abstract: Recently developed aluminum alloys based on the eutectic composition of the Al–Ca system exhibit excellent casting properties and, unlike silumins, show good deformability. The development of multi-component alloys, where calcium is partially replaced by lanthanum, cerium, nickel, and other eutectic-forming elements, improves their properties by producing a finer eutectic structure and enhancing their heat resistance. These alloys can all be strengthened through deformation, with severe plastic deformations being especially effective. Among these methods, rotary forging is of particular interest due to its ability to produce long billets. Lanthanum, at a specific concentration, significantly improves the alloy's plasticity, making the Al–La system particularly well-suited for deformation processing. This study investigates the effect of rotary forging on the microstructure and mechanical properties of two eutectic alloys, Al–10La and Al–6Ca–3La (wt. %). Billets in the as-cast state were rotary forged from an initial diameter of 20 mm to a final nominal diameter of 5 mm under isothermal conditions: at room temperature for the Al–10La alloy and at 200 °C for the Al–6Ca–3La alloy. The results showed that rotary forging led to an elongated structure in both alloys, with micron-sized grains forming inside the dendrites and eutectic particles being refined. In the Al–10La alloy, the dislocation density was low, while in the Al–6Ca–3La alloy, the dislocation density was higher. The Al–10La alloy showed a slight tendency to soften during rotary forging, whereas the Al–6Ca–3La alloy exhibited a marked tendency to strengthen (its strength doubled). Both alloys retained high plasticity (elongation) after forging. After annealing at 300 °C, the strength of both alloys remained stable. The tensile strength of the Al–6Ca–3La alloy at 300 °C was higher than that of the Al–10La alloy, with values of 53 MPa and 44 MPa, respectively.

Keywords: aluminum alloy, rotary forging, microstructure, mechanical properties.

Acknowledgments: The work was carried out within the state assignment of Baikov Institute of Metallurgy and Materials Science of Russian Academy of Sciences (project No. 075-00320-24-00).
We thank M.A. Barykin for assistance in obtaining ingots and A.V. Doroshenko for assistance in conducting the research.

For citation: Andreev V.A., Gorshenkov M.V., Naumova E.A., Rogachev S.O. Effect of rotary forging on the structure and mechanical properties of two eutectic alloys of the Al–La and Al–Ca–La systems. *Izvestiya. Non-Ferrous Metallurgy.* 2025;31(1):58–66.
https://doi.org/10.17073/0021-3438-2025-1-58-66

Влияние ротационной ковки на структуру и механические свойства двух эвтектических сплавов систем Al–La и Al–Ca–La

В.А. Андреев[1], **М.В. Горшенков**[2], **Е.А. Наумова**[2], **С.О. Рогачев**[1,2]

[1] **Институт металлургии и материаловедения им. А.А. Байкова РАН**
Россия, 119334, г. Москва, Ленинский пр-т, 49

[2] **Национальный исследовательский технологический университет «МИСИС»**
Россия, 119049, г. Москва, Ленинский пр-т, 4, стр. 1

✉ Станислав Олегович Рогачев (csaap@mail.ru)

Аннотация: Разработанные в последние годы алюминиевые сплавы на основе эвтектики системы алюминий–кальций обладают превосходными литейными свойствами и, в отличие от силуминов, хорошо деформируются. Создание многокомпонентных сплавов, в которых кальций частично замещен лантаном, церием, никелем и другими эвтектикообразующими элементами, позволяет улучшать свойства сплавов за счет формирования более дисперсной эвтектики, а также повышать их теплостойкость. Все перечисленные сплавы можно упрочнять деформационными методами, при этом особенно эффективны методы больших пластических деформаций. Среди них ротационная ковка представляет наибольший интерес ввиду возможности получения длинномерных заготовок. Лантан в определенной концентрации эффективно повышает пластичность, поэтому сплав системы Al–La является наиболее подходящим для деформационной обработки. Было изучено влияние ротационной ковки на микроструктуру и механические свойства двух эвтектических сплавов: Al–10La и Al–6Ca–3La (мас. %). Ротационную ковку заготовок в исходно литом состоянии с начального диаметра 20 мм на конечный номинальный диаметр 5 мм осуществляли в изотермических условиях: для сплава Al–10La – при комнатной температуре, а для сплава Al–6Ca–3La – при t = 200 °C. Установлено, что в результате ротационной ковки структура обоих сплавов становится вытянутой, внутри дендритов формируются зерна микронного размера, а частицы эвтектики измельчаются. При этом в сплаве Al–10La наблюдается низкая плотность дислокаций, в то время как в сплаве Al–6Ca–3La – повышенная. Сплав Al–10La склонен к небольшому разупрочнению в условиях ротационной ковки, в отличие от сплава Al–6Ca–3La, который проявляет заметную тенденцию к деформационному упрочнению (прочность увеличивается в 2 раза); при этом оба сплава в состоянии после ковки сохраняют высокую пластичность (относительное удлинение). Уровень прочности обоих сплавов сохраняется после отжига при t = 300 °C. Предел прочности сплава Al–6Ca–3La при температуре испытания 300 °C выше в сравнении со сплавом Al–10La – соответственно 53 и 44 МПа.

Ключевые слова: алюминиевый сплав, ротационная ковка, микроструктура, механические свойства.

Благодарности: Работа выполнена в рамках государственного задания ИМЕТ РАН № 075-00320-24-00.
Благодарим М.А. Барыкина за помощь в получении слитков и А.В. Дорошенко за помощь в проведении исследований.

Для цитирования: Андреев В.А., Горшенков М.В., Наумова Е.А., Рогачев С.О. Влияние ротационной ковки на структуру и механические свойства двух эвтектических сплавов систем Al–La и Al–Ca–La. *Известия вузов. Цветная металлургия*. 2025;31(1):58–66. https://doi.org/10.17073/0021-3438-2025-1-58-66

Introduction

Aluminum alloys based on the Al—Me eutectic system (where Me = Ca, Ce, La, Ni, Fe) feature a composite structure comprising an aluminum matrix and eutectic phases. These alloys exhibit excellent casting properties and good deformability [1—6]. Additionally, alloys such as Al—La, Al—Ce, Al—Ni, and, in some cases, Al—Fe demonstrate enhanced heat resistance [7; 8]. While these alloys have similar strength levels, their plasticity varies significantly, as it directly depends on the composition of the eutectic. Lanthanum, in certain concentrations, effectively increases plasticity [9], making the Al—La system particularly suitable for deformation processing. The elongation at fracture for the eutectic composition of Al—10La (wt. %) is approximately 22 % [9]. However, increasing the lanthanum content beyond this level reduces plasticity [10]. A drawback of lanthanum is its high cost. On the other hand, among the alloys mentioned above, Al—Ca alloys are the most cost-effective. Therefore, the use of small amounts of lanthanum in complex eutectic compositions, such as Al—Ca—La-based alloys, is of interest. Complex eutectics have been studied in several works [11—13].

All these alloys can be effectively strengthened using both traditional deformation methods, such as rolling,

and severe plastic deformation techniques [6; 9; 11; 14—16]. Among these techniques, rotary forging stands out due to its ability to achieve high deformation levels while also enabling the production of long billets [17—19].

Building on this, the present study examines the effect of lanthanum in the eutectic composition on the strength and plasticity of the Al—6%Ca—3%La aluminum alloy under rotary forging conditions. For comparison, the eutectic alloy Al—10%La was selected as a reference.

Materials and methods

Two alloys near the eutectic composition, Al—6Ca—3La and Al—10La (wt. %), were studied. Castings with a length of 200 mm and a diameter of 22 mm were turned on a lathe to a final diameter of 20 mm and then subjected to rotary forging. The as-cast billets were forged to a final nominal diameter of 5 mm using a rotary forging machine (RKM1, model V2129.01) in multiple passes, with the reduction per pass ranging from 5 % to 22 % (averaging 13 %). Before each pass, billets of the Al—6Ca—3La alloy were heated to 200 °C in an electric-tube furnace and held at this temperature for 10—15 min, whereas billets of the Al—10La alloy were forged without preheating. For larger diameters (greater than 10 mm), the billets were fed manually, while for subsequent passes, automatic roller feeding was employed. This ensured billet alignment and more uniform deformation distribution along the billet's length. The final diameters of the Al—6Ca—3La and Al—10La alloy billets were 5.5 mm and 5.4 mm, respectively, corresponding to an equivalent strain of $e = 2.6$.

The characterization of the specimens was carried out using transmission electron microscopy (TEM) (JEM-1400 and JEM-2100 microscopes, JEOL, Japan), Vickers microhardness measurements (Micromet 5101, Buehler, USA), and tensile testing. Two types of specimens were prepared for tensile tests: cylindrical specimens with a gauge section of ∅4×10 mm and flat specimens with a gauge section of 5×1,5×1 mm. Tensile tests at room temperature were conducted on both cylindrical and flat specimens using Instron 5569 and Instron 5966 testing machines (Instron Corp., USA), respectively. Tests at 300 °C were performed exclusively on cylindrical specimens using an Instron 3382 machine. The strain rate during tensile testing was maintained at 0.002 s^{-1}.

Research results

The as-cast Al—10La alloy exhibited a predominantly eutectic structure [(Al) + $Al_{11}La_3$] with a small fraction of aluminum dendrites (Fig. 1, *a*). As a result of rotary forging, the structural elements of the alloy were elongated along the billet axis. Additionally, ultrafine grains smaller than 1 μm were formed within the dendrites (indicated by arrows in Fig. 2, *a*), and the eutectic particles were fragmented into pieces approximately 100—200 nm in length due to cleavage. This is evidenced by the flat boundary between two fragmented particles (Fig. 2, *b*). Evidently, in certain areas of the structure, mixing of dendrites and eutectic phases occurs as a result of mass transfer. TEM images show that the dislocation density in the alloy is low.

The difference in the microstructure of the as-cast Al—6Ca—3La alloy compared to the Al—10La alloy lies in the presence of shorter and wider eutectic particles (Fig. 1, *b*). According to [20], the Al—Ca—La system forms a ternary eutectic [(Al)+Al_4(Ca,La) + + $Al_{11}(La,Ca)_3$]. During rotary forging of the Al—6Ca—3La alloy, similar to the Al—10La alloy, mixing

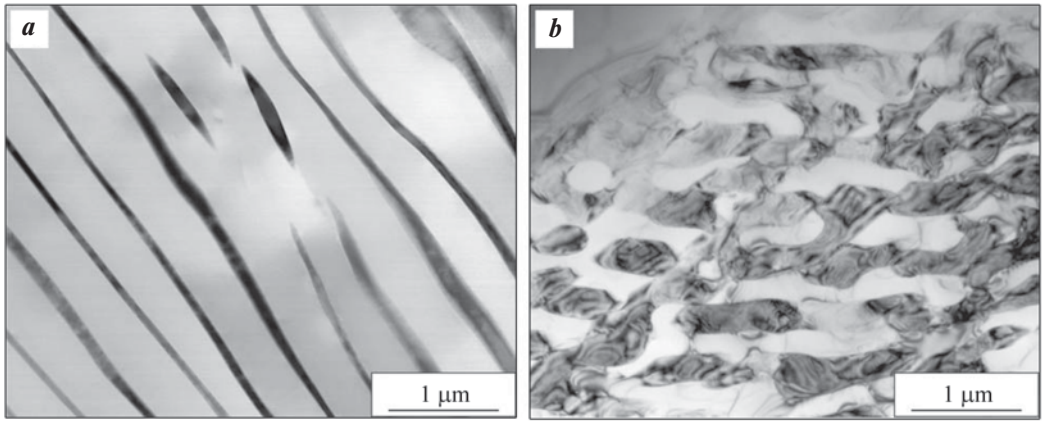

Fig. 1. Microstructure of the as-cast Al–10La (***a***) and Al – 6Ca – 3La (***b***) alloys (bright-field TEM images)

Рис. 1. Микроструктура сплавов Al–10La (***a***) и Al–6Ca–3La (***b***) в литом состоянии (светлопольные изображения ПЭМ)

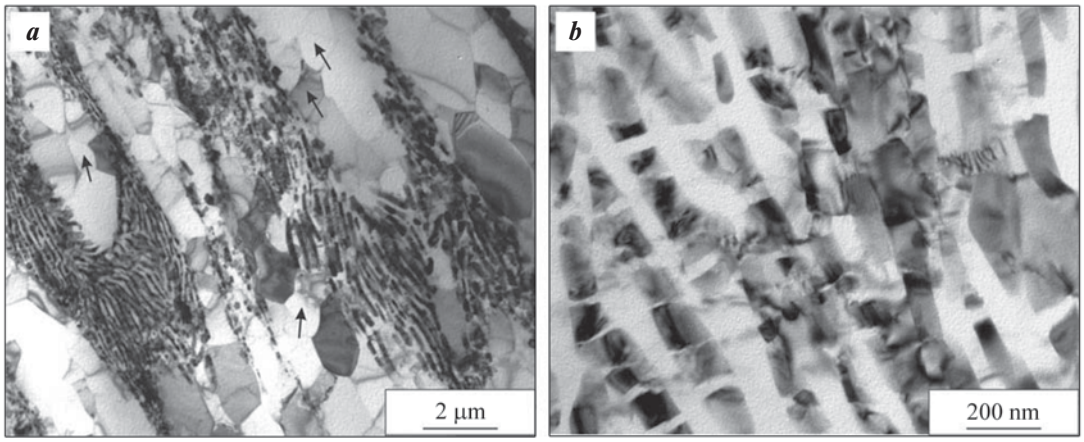

Fig. 2. Microstructure of the Al–10La alloy after rotary forging (bright-fields TEM images)

Рис. 2. Микроструктура сплава Al–10La после ротационной ковки (светлопольные изображения ПЭМ)

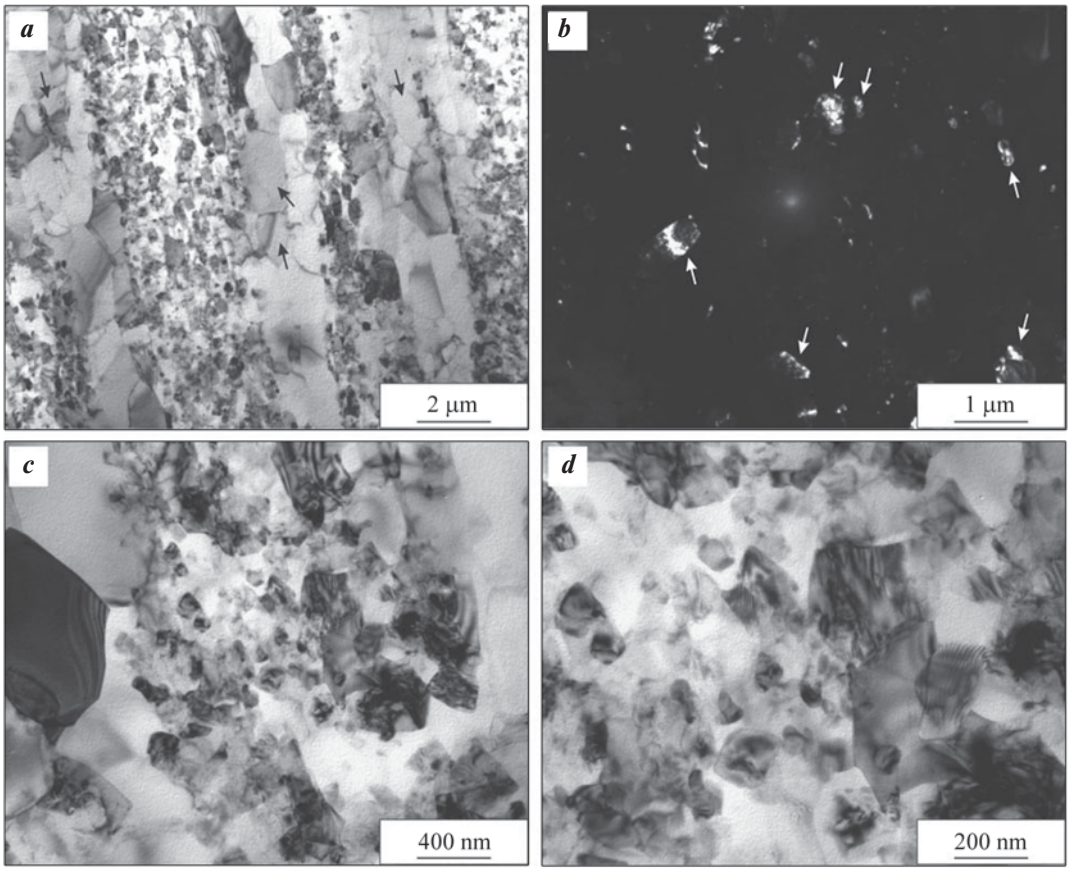

Fig. 3. Microstructure of the Al–6Ca–3La alloy after rotary forging
a, ***c***, ***d*** – bright-field TEM images; ***b*** – dark-field TEM image in (Al) reflections

Рис. 3. Микроструктура сплава Al–6Ca–3La после ротационной ковки
a, ***c***, ***d*** – светлопольные изображения ПЭМ; ***b*** – темнопольное изображение ПЭМ в рефлексах (Al)

of dendrites and eutectic phases occurs, the structural elements become elongated, and ultrafine grains form within the dendrites (indicated by arrows in Fig. 3, *a*, *b*). The eutectic particles are fragmented to a greater extent, reaching sizes of 50—100 nm, with evidence of diffusion processes indicated by the rounded shapes of the fragmented particles (Fig. 3, *c*, *d*). The former eutectic structure exhibits a higher dislocation density,

as reflected by the characteristic contrast in the TEM images.

The mechanical properties of the aluminum alloys in as-cast and forged conditions, obtained at room temperature, are presented in Table 1. The yield strength ($\sigma_{0.2}$) and ultimate tensile strength (σ_u) of the as-cast Al—10La alloy were 113 MPa and 173 MPa, respectively, with a total elongation (δ) ~22 %. For the as-cast Al—6Ca—3La alloy, the values were $\sigma_{0.2}$ = 109 MPa, σ_u = 194 MPa, and δ = 20 %.

Typical tensile curves obtained during testing of cylindrical specimens of forged alloys are shown in Fig. 4. The main difference between testing flat and cylindrical specimens of the Al—10La alloy is the significantly higher elongation of the latter (by a factor of 2, as shown in Table 1). In contrast, for the Al—6Ca—3La alloy, the difference in mechanical properties between cylindrical and flat specimens is negligible (Table 1).

After rotary forging of the Al—10La alloy, its yield strength remains unchanged or increases by no more than 10 %, while its ultimate tensile strength decreases by 18 %. At the same time, the total elongation increases slightly (Table 1). Additionally, the shape of the tensile curve changes: the uniform plastic deformation region (up to necking) decreases significantly, from 8 % to 1.5 %. As a result, nearly all of the specimen's elongation occurs in the localized deformation region (Fig. 4, *a*).

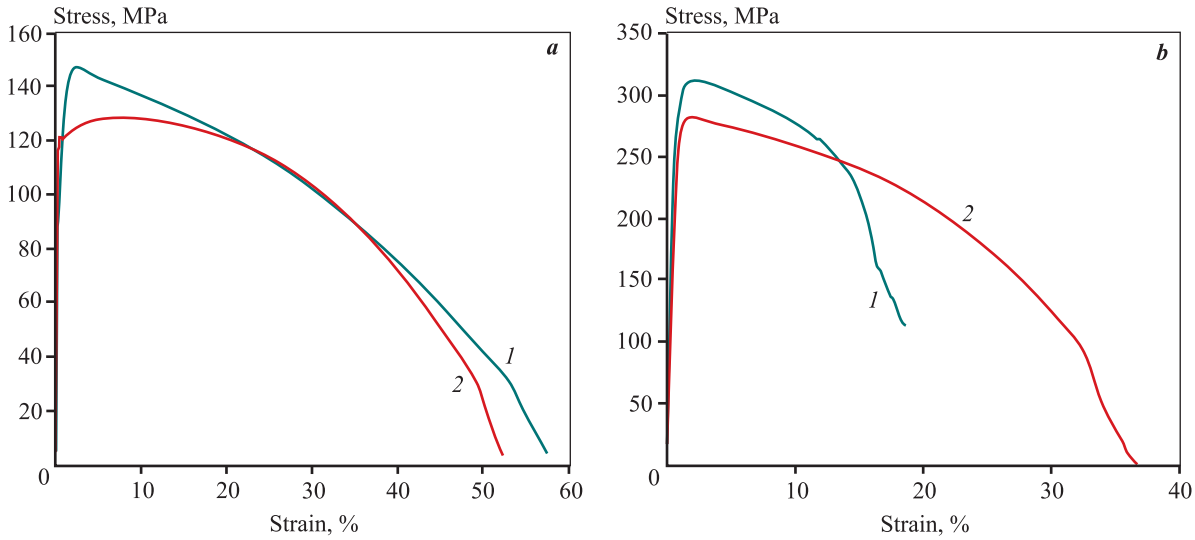

Fig. 4. Tensile curves at room temperature for specimens of Al–10La (***a***) and Al–6Ca–3La (***b***) alloys after rotary forging (***1***) and after subsequent annealing at t = 300 °C (***2***)

Рис. 4. Кривые растяжения при комнатной температуре образцов сплавов Al–10La (***a***) и Al–6Ca–3La (***b***) после ротационной ковки (***1***) и последующего отжига при t = 300 °C (***2***)

Table 1. **Mechanical properties of aluminum alloys in various conditions at room temperature**

Таблица 1. Механические свойства алюминиевых сплавов в различных состояниях при комнатной температуре

Alloy	Material condition	Specimen type	$\sigma_{0.2}$, MPa	σ_u, MPa	δ, %	δ_u, %
Al–10La	As-cast	Flat	113 ± 2	173 ± 3	22 ± 1	8 ± 1
	RF*	Flat	126 ± 3	142 ± 1	27 ± 2	1.5 ± 0.5
		Cylindrical	101 ± 2	147 ± 3	58 ± 2	2.5 ± 0.5
	RF + annealing at 300 °C	Cylindrical	123 ± 2	131 ± 2	52 ± 2	8 ± 1
Al–6Ca–3La	As-cast	Flat	109 ± 2	194 ± 3	19.5 ± 1.3	8.5 ± 0.5
	RF	Flat	252 ± 4	303 ± 3	23.5 ± 0.5	2.5 ± 0.3
		Cylindrical	285 ± 3	312 ± 6	21.6 ± 1.5	3.0 ± 0.5
	RF + annealing at 300 °C	Cylindrical	250 ± 6	283 ± 6	37 ± 2	2.0 ± 0.5

* RF – rotary forging.

In the case of the Al—6Ca—3La alloy, rotary forging results in a 2.3-fold increase in its yield strength and a 1.6-fold increase in its ultimate tensile strength, while the total elongation increases only slightly, from 19 % to 23 % (Table 1). However, the uniform elongation of the forged specimen also decreases, from 8.5 % to 2.5 % (Fig. 4, *b*).

The tensile test results correlate well with the measured microhardness values (Fig. 5). The average microhardness of the as-cast Al—10La and Al—6Ca—3La alloys was 52 ± 2 HV and 58 ± 1 HV, respectively. After rotary forging, the microhardness decreased to 42 ± 1 HV (softening) for Al—10La and increased to 82 ± 2 HV (strengthening) for Al—6Ca—3La. The microhardness was uniformly distributed across the cross-section of the billets for both alloys.

Annealing of specimens of both alloys at 300 °C for 1 h reduces their strength by no more than 10 % (see Table 1 and Fig. 4). For the Al—10La alloy, the total elongation remains essentially unchanged, but the uniform deformation increases significantly (up to 8 %). Conversely, for the Al—6Ca—3La alloy, the total elongation increases to 37 %, while the uniform deformation remains unchanged. The retention of a high combination of mechanical properties in both alloys after annealing at 300 °C demonstrates their high thermal stability.

Table 2 presents the mechanical properties of the forged aluminum alloys tested at 300 °C, and Fig. 6 shows the corresponding tensile curves. Increasing the test temperature from room temperature to 300 °C causes significant softening in both alloys. For

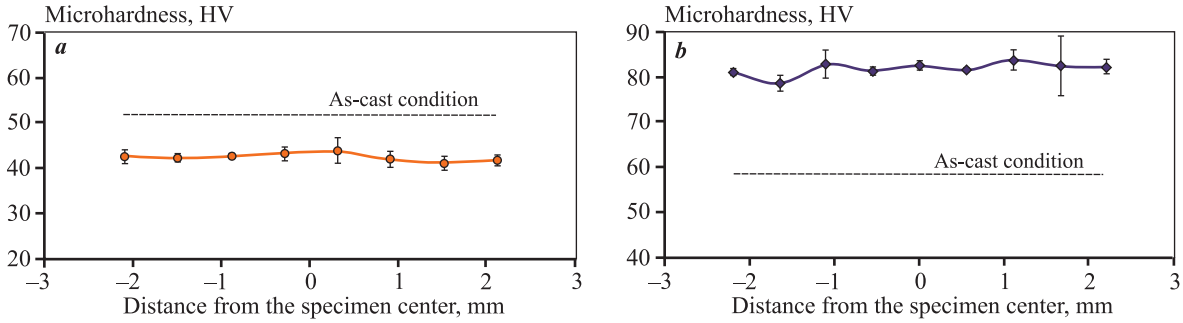

Fig. 5. Microhardness distribution across the cross-section of specimens of Al–10La (***a***) and Al–6Ca–3La (***b***) alloys before and after rotary forging

Рис. 5. Распределение микротвердости в поперечном сечении образцов сплавов Al–10La (***a***) и Al–6Ca–3La (***b***) до и после ротационной ковки

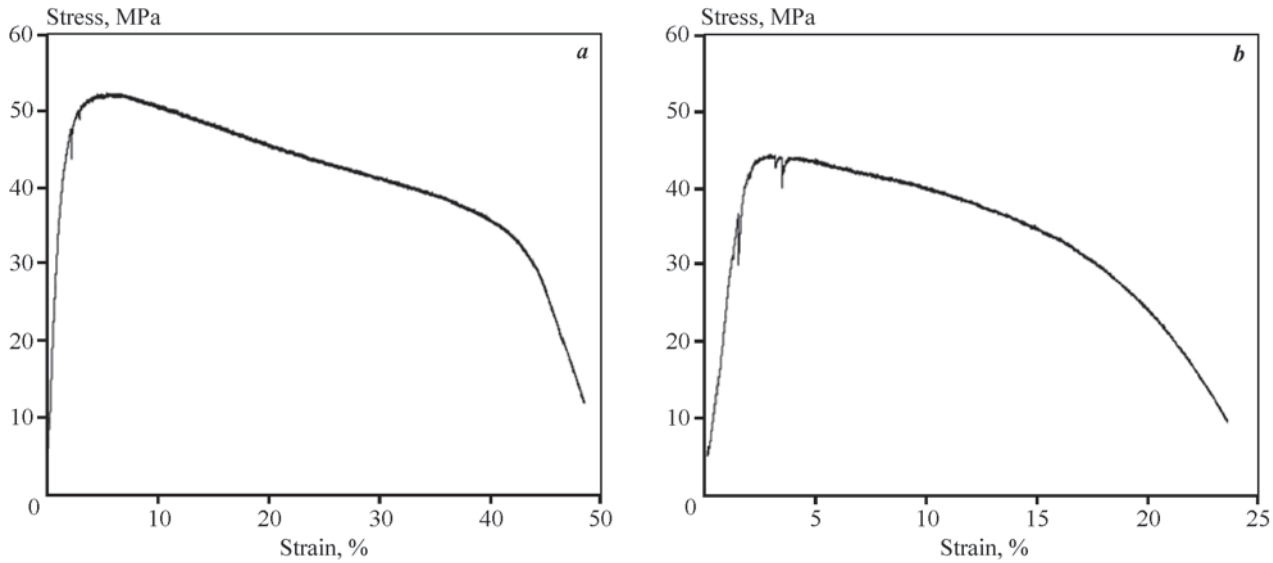

Fig. 6. Tensile curves at a test temperature of 300 °C for forged Al–6Ca–3La (***a***) and Al–10La (***b***) alloys

Рис. 6. Кривые растяжения при температуре испытания 300 °C кованых сплавов Al–6Ca–3La (***a***) и Al–10La (***b***)

Table 2. **Mechanical properties of forged aluminum alloys at a test temperature of 300 °C**

Таблица 2. Механические свойства кованых алюминиевых сплавов при температуре испытания 300 °C

Alloy	Specimen type	$\sigma_{0.2}$, MPa	σ_u, MPa	δ, %
Al–10La	Cylindrical	34 ± 1	44 ± 1	22.9 ± 0.5
Al–6Ca–3La	Cylindrical	36 ± 1	53 ± 1	47.7 ± 0.5

the Al—10La alloy, the yield strength and ultimate tensile strength decrease to 34 MPa and 44 MPa, respectively, which is a 3-fold reduction, while the total elongation decreases by a factor of 2.5. For the Al—6Ca—3La alloy, the yield strength and ultimate tensile strength decrease to 36 MPa and 53 MPa, respectively, representing reductions by factors of 8 and 6. However, the total elongation, in contrast, doubles. This level of strength is comparable to D18 or AMts alloys and slightly lower than AMg2 alloy. Despite undergoing more intense softening, the Al—6Ca—3La alloy exhibits slightly higher strength at a test temperature of 300 °C compared to the Al—10La alloy.

Discussion of results

According to the microhardness measurements and tensile test results, the Al—10La alloy exhibits slight softening under rotary forging conditions, in contrast to the Al—6Ca—3La alloy, which demonstrates a significant tendency for deformation strengthening. Additionally, in both alloys, uniform deformation (up to necking) decreases after deformation processing, while total elongation to fracture increases. The low strength of the Al—10La alloy after rotary forging, comparable to its as-cast condition, is supported by the low dislocation density observed in its microstructure (see Fig. 2, *a*), which may be attributed to recovery processes. On the other hand, the low dislocation density in the alloy's structure contributes to its high plasticity. Previous studies have shown that eutectic $Al_{11}La_3$ particles, due to their specific crystallographic relationship with the aluminum matrix, are easily cut by dislocations [9], which also positively affects plasticity. Interestingly, despite the low dislocation density in its structure, the uniform deformation of the Al—10La alloy is only about 2 %, with elongation mainly occurring in the localized deformation region, i.e., after necking begins.

In contrast, the Al—6Ca—3La alloy accumulates a high dislocation density and undergoes significant eutectic particle refinement as a result of rotary forging, leading to a substantial increase in strength. Despite its high strength, the alloy also retains high plasticity (with elongation primarily occurring in the localized deformation region, similar to the Al—10La alloy). This behavior may be attributed to the presence of ultrafine aluminum grains (which, being defect-free, form layers between the former eutectic, see Fig. 3, *a*) that promote stress relaxation, as well as the positive effect of lanthanum in the complex eutectic on dislocation slip processes.

Conclusion

Rotary forging was performed on billets of the eutectic aluminum alloys Al—10La and Al—6Ca—3La in the as-cast condition, reducing their initial nominal diameter of 20 mm to a final nominal diameter of 5 mm. It was found that as a result of forging, the structure of both alloys becomes aligned along the billet axis, with new ultrafine grains (less than 1 μm) forming within the dendrites and eutectic particles becoming refined (to 100—200 nm in the Al—10La alloy and 50—100 nm in the Al—6Ca—3La alloy). In the Al—10La alloy, a low dislocation density was observed, while the Al—6Ca—3La alloy exhibited a high dislocation density. The structural changes in the alloys significantly affect their mechanical properties: the Al—10La alloy undergoes slight softening under rotary forging, while the Al—6Ca—3La alloy exhibits a pronounced tendency for deformation strengthening, with its strength doubling. The ultimate tensile strength of the forged Al—10La and Al—6Ca—3La alloys was approximately 150 MPa and 300 MPa, respectively. Both alloys retained high plasticity after forging, with total elongation exceeding 20 %. The strength of both alloys remained stable after annealing at 300 °C. At a test temperature of 300 °C, the ultimate tensile strength of the Al—6Ca—3La alloy slightly exceeded that of the Al—10La alloy, at 53 MPa and 44 MPa, respectively.

References

1. Ozturk K., Chen Long-Qing, Liu Zi-Kui. Thermodynamic assessment of the Al—Ca binary system using random solution and associate models. *Journal of Alloys and Compounds*. 2002;340(1—2):199—206. https://doi.org/10.1016/S0925-8388(01)01713-3
2. Hawksworth A., Rainforth W.M., Jones H. Solidification microstructure selection in the Al-rich Al—La, Al—Ce and Al—Nd systems. *Journal of Crystal Growth*. 1999;197(1—2):286—296. https://doi.org/10.1016/S0022-0248(98)00955-5

3. Cacciamani G., Ferro R. Thermodynamic modeling of some aluminium-rare earth binary systems: Al—La, Al—Ce and Al—Nd. *Calphad*. 2001;25(4):583—597. https://doi.org/10.1016/S0364-5916(02)00009-3
4. Czerwinski F. Cerium in aluminum alloys. *Journal of Materials Science*. 2020;55:24—72. https://doi.org/10.1007/s10853-019-03892-z
5. Voroshilov D.S., Sidelnikov S.B., Bespalov V.M., Sokolov R.E., Bermeshev T.V., Berngardt V.A., Lezhnev S.N., Durnopyanov A.V., Kovaleva A.A., Konstantinov I.L., Novikova O.S., Motkov M.M. Combined rolling-extrusion of various billets from the Al—Ce—La alloy for electrical wire production. *The International Journal of Advanced Manufacturing Technology*. 2024;131:4699—4725. https://doi.org/10.1007/s00170-024-13339-8
6. Belov N.A., Alabin A.N., Eskin D.G. Improving the properties of cold rolled Al—6%Ni sheets by alloying and heat treatment. *Scripta Materialia*. 2004;50(1):89—94. https://doi.org/10.1016/j.scriptamat.2003.09.033
7. Cao Z., Kong G., Che Ch., Wang Y., Peng H. Experimental investigation of eutectic point in Al-rich Al—La, Al—Ce, Al—Pr and Al—Nd systems. *Journal of Rare Earths*. 2017;35(10):1022—1028. https://doi.org/10.1016/S1002-0721(17)61008-1
8. Belov N.A., Zolotorevskii V.S. Casting alloys on the base of aluminum-nickel eutectic (nikalines) as possible alternative to silumins. *Tsvetnye Metally*. 2002;(2):99—105. (In Russ.).
Белов Н.А., Золоторевский В.С. Литейные сплавы на основе алюминиево-никелевой эвтектики (никалины) как возможная альтернатива силуминам. *Цветные металлы*. 2003;(2):99—105.
9. Rogachev S.O., Naumova E.A., Lukina E.A, Zavodov A.V., Khatkevich V.M. High strength Al—La, Al—Ce, and Al—Ni eutectic aluminum alloys obtained by high-pressure torsion. *Materials*. 2021;14(21):6404. https://doi.org/10.3390/ma14216404
10. He Y., Liu J., Qiu Sh., Deng Zh., Zhang J., Shen Y. Microstructure evolution and mechanical properties of Al—La alloys with varying La contents. *Materials Science and Engineering: A*. 2017;701:134—142. https://doi.org/10.1016/j.msea.2017.06.023
11. Murashkin M.Y., Sabirov I., Medvedev A.E., Enikeev N.A., Lefebvre W., Valiev R.Z., Sauvage X. Mechanical and electrical properties of an ultrafine grained Al—8.5 wt.% RE (RE = 5.4 wt.% Ce, 3.1 wt.% La) alloy processed by severe plastic deformation. *Materials and Design*. 2016;90:433—442. https://doi.org/10.1016/j.matdes.2015.10.163
12. Shurkin P.K., Letyagin N.V., Yakushkova A.I., Samoshina M.E., Ozherelkov D.Y., Akopyan T.K. Remarkable thermal stability of the Al—Ca—Ni—Mn alloy manufactured by laserpowder bed fusion. *Materials Letters*. 2021;285:129074. https://doi.org/10.1016/j.matlet.2020.129074
13. Belov N.A., Naumova E.A., Eskin D.G. Casting alloys of the Al—Ce—Ni system: microstructural approach to alloy design. *Materials Science and Engineering: A*. 1999;271(1—2):134—142. https://doi.org/10.1016/S0921-5093(99)00343-3
14. Rogachev S.O., Naumova E.A., Karelin R.D., Andreev V.A., Perkas M.M., Yusupov V.S., Khatkevich V.M. Structure and mechanical properties of Al—Ca—Mn—Fe—Zr—Sc eutectic aluminum alloy after Warm equal channel angular pressing. *Russian Journal of Non-Ferrous Metals*. 2021;62:293—301. https://doi.org/10.3103/S1067821221030123
Рогачев С.О., Наумова Е.А., Карелин Р.Д., Андреев В.А., Перкас М.М., Юсупов В.С., Хаткевич В.М. Структура и механические свойства эвтектического алюминиевого сплава Al—Ca—Mn—Fe—Zr—Sc после теплого равноканального углового прессования. *Известия вузов. Цветная металлургия*. 2021;27(2):56—65. https://doi.org/10.17073/0021-3438-2021-2-56-65
15. Xu R., Lu Y., Dai Y., Brognara A., Hahn H., Ivanisenko Y. Processing of high-strength thermal-resistant Al — 2.2 % cerium — 1.3 % lanthanum alloy rods with high electric conductivity by High Pressure Torsion Extrusion. *Journal of Materials Science*. 2024;59:9075—9090. https://doi.org/10.1007/s10853-024-09713-2
16. Duchaussoy A., Sauvage X., Edalati K., Horita Z., Renou G., Deschamps A., Geuser F.D. Structure and mechanical behavior of ultrafine-grained aluminum-iron alloy stabilized by nanoscaled intermetallic particles. *Acta Materialia*. 2019;167:89—102. https://doi.org/10.1016/j.actamat.2019.01.027
17. Rogachev S.O., Andreev V.A., Yusupov V.S., Bondareva S.A., Hatkevich V.M., Nikolaev E.V. Effect of rotary forging on microstructure evolution and mechanical properties of aluminum alloy / copper bimetallic material. *Metals and Materials International*. 2022;28:1038-1046. https://doi.org/10.1007/s12540-020-00964-7
18. Klumpp A., Kauffmann A., Seils S., Dietrich S., Schulze V. Influence of cold rotary swaging on microstructure and uniaxial mechanical behavior in alloy 718. *Metallurgical and Materials Transactions A*. 2021;52:2021—4331. https://doi.org/10.1007/s11661-021-06371-w

19. Asfandiyarov R.N., Raab G.I. Investigation of the method of rotary swaging under the conditions of large strains. *Vestnik UGATU*. 2016;20(3(73)):3—6. (In Russ.).
Асфандияров Р.Н., Рааб Г.И. Исследование метода ротационного обжатия в условиях больших деформаций. *Вестник УГАТУ*. 2016;20(3(73)):3—6.

20. Akopyan T.K., Belov N.A., Lukyanchuk A.A., Letyagin N.V., Sviridova T.A., Petrova A.N., Fortuna A.S., Musin A.F. Effect of high pressure torsion on the precipitation hardening in Al—Ca—La based eutectic alloy. *Materials Science and Engineering: A*. 2021;802:140633. https://doi.org/10.1016/j.msea.2020.140633

Information about the authors

Vladimir A. Andreev – Cand. Sci. (Eng.), Leading Researcher, Baikov Institute of Metallurgy and Materials Science of the Russian Academy of Sciences.
https://orcid.org/0000-0003-3937-1952
E-mail: andreev.icmateks@gmail.com

Mikhail V. Gorshenkov – Cand. Sci. (Eng.), Assistant Professor of the Department of physical materials science, National University of Science and Technology "MISIS" (NUST MISIS).
https://orcid.org/0000-0001-8780-7584
E-mail: mvg@misis.ru

Evgeniya A. Naumova – Cand. Sci. (Eng.), Assistant Professor of the Department of metal forming, NUST MISIS.
https://orcid.org/0000-0002-4419-2943
E-mail: jan73@mail.ru

Stanislav O. Rogachev – Dr. Sci. (Eng.), Assistant Professor of the Department of physical metallurgy and physics of strength, NUST MISIS.
https://orcid.org/0000-0001-7769-7748
E-mail: csaap@mail.ru

Информация об авторах

Владимир Александрович Андреев – к.т.н., вед. науч. сотрудник Института металлургии и материаловедения (ИМЕТ) им. А.А. Байкова РАН.
https://orcid.org/0000-0003-3937-1952
E-mail: andreev.icmateks@gmail.com

Михаил Владимирович Горшенков – к.т.н., доцент кафедры физического материаловедения Национального исследовательского технологического университета (НИТУ) «МИСИС».
https://orcid.org/0000-0001-8780-7584
E-mail: mvg@misis.ru

Евгения Александровна Наумова – к.т.н., доцент кафедры обработки металлов давлением НИТУ МИСИС.
https://orcid.org/0000-0002-4419-2943
E-mail: jan73@mail.ru

Станислав Олегович Рогачев – д.т.н., доцент кафедры металловедения и физики прочности НИТУ МИСИС.
https://orcid.org/0000-0001-7769-7748
E-mail: csaap@mail.ru

Contribution of the authors

V.A. Andreev – developed the methodology, performed the experiments.

M.V. Gorshenkov – conducted electron microscopy analysis, contributed to the discussion of results.

E.A. Naumova – defined the objectives of the work, contributed to the discussion of results.

S.O. Rogachev – defined the objectives of the work, performed the experiments, wrote the article.

Вклад авторов

В.А. Андреев – определение методологии, проведение экспериментов.

М.В. Горшенков – проведение электронно-микроскопического анализа, участие в обсуждении результатов.

Е.А. Наумова – определение цели работы, участие в обсуждении результатов.

С.О. Рогачев – определение цели работы, проведение экспериментов, написание статьи.

The article was submitted 28.06.2024, revised 12.08.2024, accepted for publication 14.08.2024

Статья поступила в редакцию 28.06.2024, доработана 12.08.2024, подписана в печать 14.08.2024

UDC 669.017.165
https://doi.org/10.17073/0021-3438-2025-1-67-79

Research article
Научная статья

Effect of hot deformation and heat treatment conditions on the structure and mechanical properties of the VIT1 alloy based on orthorhombic titanium aluminide

V.S. Sokolovsky[1], **E.I. Nozdracheva**[1], **K.A. Kyaramyan**[2], **Yu.G. Bykov**[2], **E.B. Alekseev**[3], **G.A. Salishchev**[1]

[1] **Belgorod State National Research University**
85 Pobedy Str., Belgorod 308015, Russia

[2] **Branch of JSC "United Engine Corporation"**
"Research Institute of Technology and Organization of Engine Production"
16 Budyonny Prosp., Moscow 105118, Russia

[3] **All-Russian Scientific Research Institute of Aviation Materials**
of the National Research Centre "Kurchatov Institute"
17 Radio Str., Moscow 105005, Russia

✉ Vitaly S. Sokolovsky (sokolovskiy@bsu.edu.ru)

Abstract: The effect of thermo-mechanical treatment on the structure and mechanical properties of the hot-rolled orthorhombic titanium aluminide alloy VIT1 was investigated. The evolution of the microstructure and mechanical behavior of the alloy during hot deformation in the temperature range of 850–1050 °C was studied. It was established that at a temperature of 950 °C, a strain rate of $\dot{\varepsilon} = 5 \cdot 10^{-4}$ s^{-1} and a strain of $\varepsilon = 70$ %, the microstructure formed during hot deformation, due to the processes of recrystallization and spheroidization, consisted of grains ~1 μm in size, comprising β-, α_2-, and O-phases. It was shown that increasing the deformation temperature led to the dissolution of O-phase particles and a significant deceleration in the development of dynamic recrystallization. Homogeneous fine-grained billets were obtained via multi-directional isothermal forging, and the effect of heat treatment (quenching and aging) on the structure and mechanical properties of the alloy was examined. Based on a preliminary study of the influence of heating temperature on the alloy's structure and properties, the temperature ranges for quenching and aging were determined. It was demonstrated that the most balanced levels of strength, ductility, and heat resistance were achieved after heat treatment under the following conditions: holding for 4 h at 1025 °C followed by air cooling, and aging at 850 °C for 6 h.

Keywords: orthorhombic titanium aluminide Ti_2NbAl, VIT1 alloy, multi-directional isothermal forging, quenching, aging, mechanical properties.

Acknowledgements: The authors gratefully acknowledge the financial support from the Russian Science Foundation (Grant No. 19-79-30066). The authors are grateful to the personnel of the Joint Research Center "Technology and Materials" of Belgorod State National Research University, for their assistance. https://rscf.ru/prjcard_int?19-79-30066

For citation: Sokolovsky V.S., Nozdracheva E.I., Kyaramyan K.A., Bykov Yu.G., Alekseev E.B., Salishchev G.A. Effect of hot deformation and heat treatment conditions on the structure and mechanical properties of the VIT1 alloy based on orthorhombic titanium aluminide. *Izvestiya. Non-Ferrous Metallurgy*. 2025;31(1):67–79. https://doi.org/10.17073/0021-3438-2025-1-67-79

Влияние режимов горячей деформации и термической обработки на структуру и механические свойства сплава на основе орторомбического алюминида титана ВИТ1

В.С. Соколовский[1], **Е.И. Ноздрачева**[1], **К.А. Кярамян**[2], **Ю.Г. Быков**[2], **Е.Б. Алексеев**[3], **Г.А. Салищев**[1]

[1] **Белгородский государственный национальный исследовательский университет**
Россия, 308015, г. Белгород, ул. Победы, 85

[2] **Филиал АО «Объединенная двигателестроительная корпорация» «Научно-исследовательский институт технологии и организации производства двигателей»**
Россия, 105118, г. Москва, пр-т Буденного, 16

[3] **Всероссийский научно-исследовательский институт авиационных материалов Национального исследовательского центра «Курчатовский институт»**
Россия, 105005, г. Москва, ул. Радио, 17

✉ Виталий Сергеевич Соколовский (sokolovskiy@bsu.edu.ru)

Аннотация: Исследовано влияние деформационно-термической обработки на структуру и механические характеристики сплава на основе орторомбического алюминида титана ВИТ1 в горячекатаном состоянии. Проведено изучение эволюции микроструктуры и механического поведения сплава при горячей деформации в температурном интервале 850–1050 °С. Установлено, что при температуре t = 950 °С, скорости деформации $\dot{\varepsilon} = 5 \cdot 10^{-4}$ $с^{-1}$ и степени деформации ε = 70 % в сплаве, вследствие протекания при горячей деформации процессов рекристаллизации и сфероидизации, формируется микроструктура с размером зерен ~1 мкм, состоящая из β-, α_2- и О-фаз. Показано, что повышение температуры деформации ведет к растворению частиц О-фазы и резкому замедлению развития динамической рекристаллизации. Всесторонней изотермической ковкой получены заготовки с однородной мелкозернистой структурой и исследовано влияние термической обработки (закалки и старения) на структуру и механические свойства сплава. По результатам предварительного изучения влияния температуры нагрева на структуру и свойства сплава определены интервалы температур закалки и старения. Показано, что наиболее сбалансированный уровень прочности, пластичности и жаропрочности получен после термической обработки при следующих условиях: выдержка 4 ч при t = 1025 °С с последующей закалкой на воздухе, старение 850 °С в течение 6 ч.

Ключевые слова: орторомбический алюминид титана Ti_2NbAl, сплав ВИТ1, всесторонняя изотермическая ковка, закалка, старение, механические свойства.

Благодарности: Работа выполнена при финансовой поддержке Российского научного фонда (соглашение № 19-79-30066) с использованием оборудования Центра коллективного пользования «Технологии и материалы» НИУ «БелГУ», https://rscf.ru/prjcard_int?19-79-30066

Для цитирования: Соколовский В.С., Ноздрачева Е.И., Кярамян К.А., Быков Ю.Г., Алексеев Е.Б., Салищев Г.А. Влияние режимов горячей деформации и термической обработки на структуру и механические свойства сплава на основе орторомбического алюминида титана ВИТ1. *Известия вузов. Цветная металлургия*. 2025;31(1):67–79.
https://doi.org/10.17073/0021-3438-2025-1-67-79

Introduction

The intermetallic alloy VIT1 (density ρ ~ 5.3 g/cm^3) based on orthorhombic titanium aluminide Ti_2NbAl was developed at FSUE "VIAM" (Moscow, Russia) [1]. It is characterized by high specific properties, an operating temperature of up to 700 °C, and is considered a promising material for high-pressure compressor (HPC) blades in modern gas turbine engines [1; 2]. Alloys based on Ti_2NbAl are deformable and undergo hot forging and/or rolling in the single-phase β-region [3–7]. In the as-cast state, the alloy exhibits extremely low ductility [1]. Hot forging or rolling in the β-, followed by the ($\beta + \alpha_2$)-phase regions significantly refines the struc-

ture, which simultaneously enhances both ductility and strength [3]. For example, a notable improvement in these properties was achieved in the Ti—20.3Al—22.1Nb—1.2Zr—1.3V—0.9Mo—0.3Si alloy through multi-directional isothermal forging, resulting in a submicron grain/particle size of 0.3 μm and achieving ultimate tensile strength σ_u = 1400 MPa and elongation δ = 25 % [8]. The grain refinement effect is retained during heat treatment. In the VTI-4 alloy, after forging and rolling in the ($\beta + \alpha_2$)-phase region, followed by a two-step heat treatment (1025 °C quenching in oil + + 750 °C for 3 h with air cooling), satisfactory values of σ_u = 1081 MPa and δ = 7.2 % were obtained [9]. In the Ti—22Al—27Nb alloy, reducing the β-grain size from 200 to 5 μm through hot rolling in the ($\beta + \alpha_2$)-phase region and subsequent heat treatment (heating to the ($\beta + \alpha_2$)-phase region followed by furnace cooling) increased the σ_u from 900 to 1050 MPa and the δ from 5 % to 15 % [5].

It is important to emphasize that grain refinement in orthorhombic titanium aluminide alloys leads to reduced creep resistance [9]. Therefore, when determining their mechanical properties, it is essential to balance strength, ductility, and heat resistance. However, systematic studies in this direction are practically absent. The formation of a fine-grained structure also significantly enhances the hot ductility of these alloys, which can be utilized in the manufacturing of complex-shaped components.

Another equally important microstructural parameter is the size of the O-phase particles, which form during the aging of quenched alloys and significantly affect their mechanical characteristics [10—13]. For instance, it was shown in [11] that increasing the aging temperature from 750 to 850 °C led to an increase in elongation from 0.4 % to 5.0 %, while the yield strength decreased from 1295 to 960 MPa. However, the literature lacks systematic data that could recommend specific conditions of deformation and heat treatment for orthorhombic titanium aluminide alloys to achieve a high combination of mechanical properties. In this regard, the aim of the present study was to develop processing conditions for structure refinement through isothermal forging and heat treatment of the VIT1 alloy to ensure a balance of strength, ductility, and heat resistance.

Materials and methods

The material studied was a 35-mm-thick hot-rolled plate of the VIT1 alloy, based on orthorhombic titanium aluminide. Isothermal uniaxial compression tests were conducted at temperatures of 850, 900, 950, 1000, and 1050 °C and a strain rate of $\dot{\varepsilon} = 5 \cdot 10^{-4}$ s^{-1}. Specimens with a diameter of 10 mm and a height of 15 mm were cut from the plate parallel to the rolling direction using wire electrical discharge machining. The tests were performed on an Instron 300LX universal testing machine. The specimens were placed in a furnace preheated to the deformation temperature, held for 10 min, deformed to a strain of ε = 70 %, and then quenched in water.

Billets measuring 35×40×100 mm, cut from the plate in the rolling direction, were annealed at 1100 °C for 0.5 h. Subsequently, multi-directional isothermal forging was performed at 950 °C on a DEVR 400 press equipped with a die block, with final-stage upsetting [14]. The initial strain rate was ~10^{-3} s^{-1}, and the total strain was — ε_Σ = 750 %. As a result, forgings with dimensions of 120×120×14 mm were obtained.

For heat treatment, specimens with dimensions of 5×5×5 mm were cut. Quenching was carried out after a 2-hour hold at 950—1100 °C, followed by water cooling. Aging was conducted at 750, 800, 820, and 850 °C for holding times of 0.5, 1, 2, 4, 6, 8, 12, 24, 48, 96, and 192 h.

The microstructure was evaluated using a scanning electron microscope (SEM) FEI Quanta 600 and a transmission electron microscope (TEM) Jeol JEM-2100. Electron backscatter diffraction (EBSD) mapping was performed using the TSL Data Collection version 6.2 software, with a scanning step of 100 nm. Data processing was carried out using TSL OIM Analysis version 6. The volumetric phase fraction was determined from SEM images according to ASTM E562-11, and the fraction of recrystallized grains was evaluated from EBSD data. TEM foils were prepared at –35 °C using an electrolyte consisting of methanol (60 %), butanol (34 %), and perchloric acid (6 %). The Vickers microhardness was measured using a Wolpert 402MVD hardness tester, following GOST 9450-76. The measurements were taken using a diamond pyramid with a base angle of 136° under a load of 500 g and a dwell time of 10 s.

For tensile testing, cylindrical specimens were prepared in accordance with GOST 1497-84, with a gauge section diameter of 3 mm and a length of 15.35 mm, and tested on an Instron 5882 machine at an initial strain rate of 10^{-3} s^{-1}. Creep tests were conducted on cylindrical specimens prepared according to GOST 10145-81, with a gauge section diameter of 5 mm and a length of 27 mm, using an ATS Creep Tester 2330 machine. Three thermocouples were attached to the specimen to monitor temperature, and an extensometer was installed to record elongation. The specimens were heated at a rate of 550 °C/h to

650 °C, held for 30 min, and then automatically loaded to a stress of 380 MPa.

Results and discussion

Fig. 1 shows the initial microstructure of the hot-rolled VIT1 alloy plate. The microstructure consists of β-grains elongated along the rolling direction, with an average length and width of approximately 500 μm and 150 μm, respectively (Fig. 1, *a*, *c*). Particles of the α_2-phase, averaging 3 μm in size, are predominantly located along the grain boundaries (Fig. 1, *a*, *b*). Electron diffraction patterns obtained via TEM also revealed the presence of needle-shaped O-phase particles with an average diameter of 200 nm and lengths ranging from 0.2 to 3 μm (Fig. 1, *d*).

To determine the optimal conditions for isothermal forging, the effect of deformation temperature on the mechanical behavior and structural evolution during uniaxial compression was studied. In specimens cut from the plate, the elongated grains formed during rolling were oriented parallel to the deformation axis (Fig. 1, *c*). At t = 850 °C, the σ–ε curve exhibits a peak followed by a sharp softening (Fig. 2), indicating the development of dynamic recrystallization (Fig. 3) and likely the localization of plastic deformation. With a further increase in temperature to 950 °C, the peak stresses decrease, and the steady-state plastic deformation stage becomes more prolonged. At t = 975÷1050 °C, the curves show no initial strengthening during flow, and a slight increase in stress with strain is attributed to the frictional contribution at the specimen surface.

After the tests, the specimens were cut along the deformation axis for further microstructural analysis. The microstructure of the deformed alloy at t = 850 °C is shown in Fig. 3, *a*. During deformation, recrystallization occurs in the β-phase, accompanied by spheroidization of O- and α_2-phase particles [15], resulting in the formation of a fine-grained structure in the central part of the specimen (Fig. 3, *a*). The average grain/particle size was 0.5 μm. Increasing the deformation temperature to 900 °C led to an increase in grain/particle size to 0.6 μm (Fig. 3, *b*).

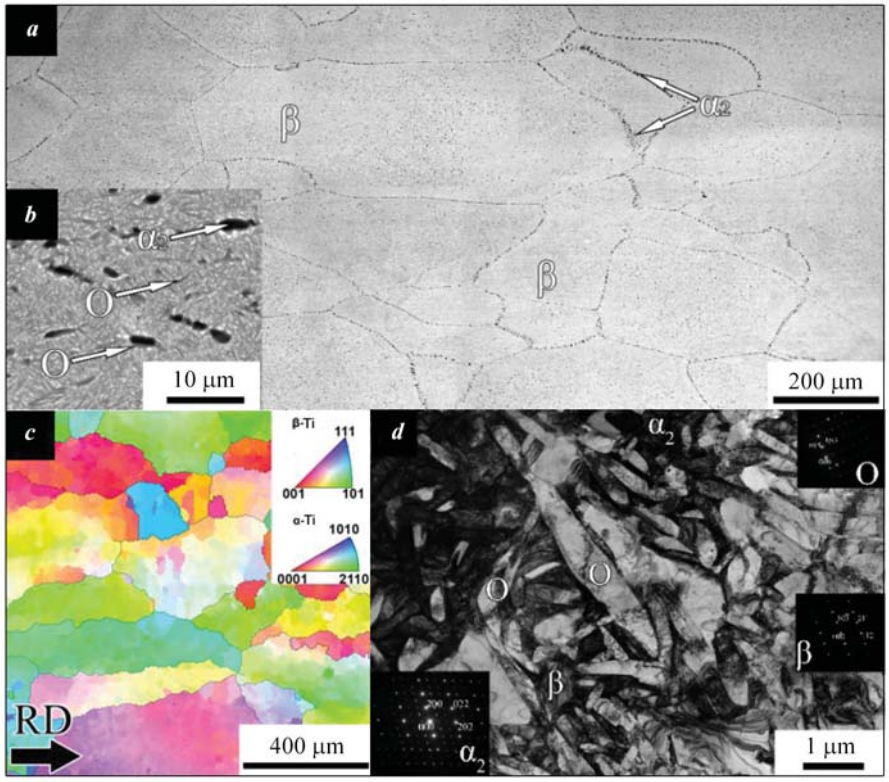

Fig. 1. Microstructure of the hot-rolled VIT1 alloy plate

a – overview SEM image; ***b*** – magnified SEM section; ***c*** – inverse pole figure map, with the rolling direction indicated by an arrow; ***d*** – electron diffraction patterns of the β-, α_2-, and O-phases

Рис. 1. Микроструктура горячекатаной плиты сплава ВИТ1

a – обзорный снимок СЭМ; ***b*** – увеличенный участок структуры СЭМ; ***c*** – карта обратных полюсные фигур, стрелкой показано направление прокатки; ***d*** – ПЭМ-картины электронной дифракции β-, α_2- и O-фаз

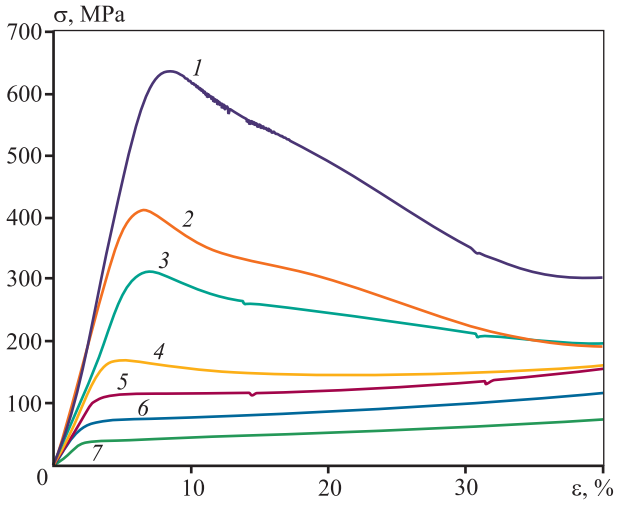

Fig. 2. σ–ε curves of the VIT1 alloy at $t = 850 \div 1050$ °C and $\dot{\varepsilon} = 5 \cdot 10^{-4}$ s^{-1}

t, °C: ***1*** – 850, ***2*** – 900, ***3*** – 925, ***4*** – 950, ***5*** – 975, ***6*** – 1000, *7* – 1050

Рис. 2. Кривые σ–ε сплава ВИТ1 при $t = 850 \div 1050$ °C и $\dot{\varepsilon} = 5 \cdot 10^{-4}$ с$^{-1}$

t, °C: ***1*** – 850, ***2*** – 900, ***3*** – 925, ***4*** – 950, ***5*** – 975, ***6*** – 1000, *7* – 1050

An important factor influencing structural evolution is the phase composition of the alloy and its changes during heating (Fig. 4). As the temperature increases from 850 to 900 °C, the volume fraction ratio of O- and β-phases changes slightly: the O-phase fraction decreases from 86 to 73 vol. %, while the β-phase fraction increases from 13 to 24 vol. % and the α_2-phase fraction from 1 to 3 vol. %. The microstructure of the alloy after deformation at $t = 950$ °C is characterized by significantly larger β-phase grains (2 μm), with O-phase (1 μm) and α_2-phase particles (1.5 μm) located both within the grains and along their boundaries (Fig. 3, *c*). The volume fraction of the O-phase decreases significantly to 22 vol. %, accompanied by an increase in the β-phase fraction to 75 vol. % and the α_2-phase fraction to 13 vol. % (Fig. 4).

The microstructural study using EBSD analysis revealed that during deformation, the initial grains align along the metal flow direction, forming a texture that becomes sharper at lower temperatures (Fig. 4). It can be observed that at $t = 950$ °C, the main structural chang-

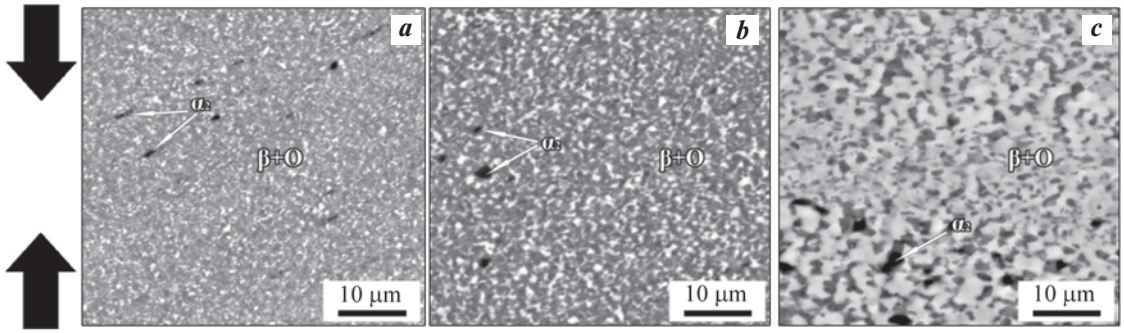

Fig. 3. Microstructure of the VIT1 alloy after deformation (SEM)

t, °C: ***a*** – 850, ***b*** – 900, ***c*** – 950; $\dot{\varepsilon} = 5 \cdot 10^{-4}$ s^{-1}; ε = 70 %. The deformation axis is oriented vertically

Рис. 3. Микроструктура после деформации сплава ВИТ1 (СЭМ)

t, °C: ***a*** – 850, ***b*** – 900, ***c*** – 950; $\dot{\varepsilon} = 5 \cdot 10^{-4}$ с$^{-1}$; ε = 70 %. Ось деформации ориентирована вертикально

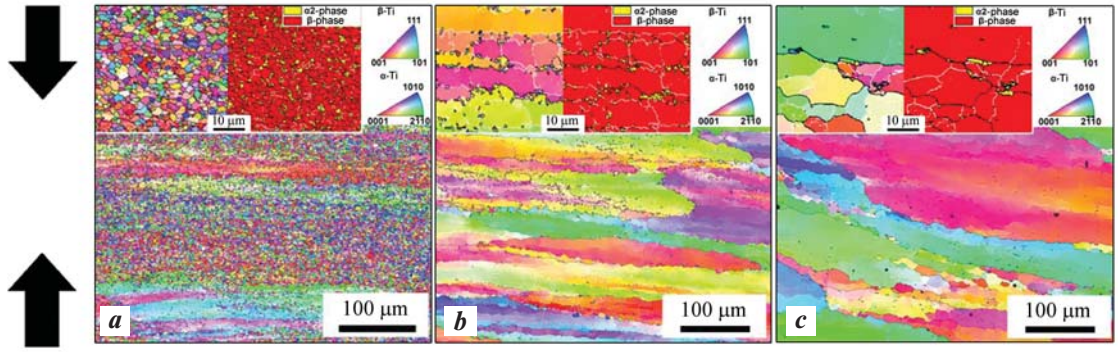

Fig. 4. Microstructure of the VIT1 alloy after deformation (EBSD IPF maps)

t, °C: ***a*** – 950, ***b*** – 975, ***c*** – 1000; $\dot{\varepsilon} = 5 \cdot 10^{-4}$ s^{-1}; ε = 70 %. The deformation axis is oriented vertically

Рис. 4. Микроструктура после деформации сплава ВИТ1 (EBSD IPF-карты)

t, °C: ***a*** – 950, ***b*** – 975, ***c*** – 1000; $\dot{\varepsilon} = 5 \cdot 10^{-4}$ с$^{-1}$; ε = 70 %. Ось деформации ориентирована вертикально

es occur predominantly within the original β-grains, which exhibit highly curved boundaries due to their migration (Fig. 4, *a*).

A further increase in the deformation temperature to 975 °C leads to the complete dissolution of O-phase particles, an increase in the β-phase fraction (89 vol. %), and a reduction in the α_2-phase fraction (11 vol. %) (Fig. 4, *b*). As a result, dynamic recovery dominates during deformation, with only slight curvature observed at some boundaries and the appearance of new recrystallized grains, approximately 10 μm in size. The average size of the large elongated β-phase grains is 160×30 μm, which is significantly smaller than in the initial state. The size of the α_2-phase particles remains unchanged at 1.5 μm. Thus, the dissolution of O-phase particles, a reduction in the α_2-phase fraction, and an increase in temperature significantly suppress dynamic recrystallization in the β-phase, as evidenced by the small number of new grains and the formation of predominantly low-angle boundaries within the original β-grains (Fig. 4, *b*). At a deformation temperature of 1000 °C, the alloy's microstructure consists of relatively large elongated β-phase grains with an average size of 200×70 μm and a small number of equiaxed α_2-phase grains, approximately 2 μm in size (4 vol. %) (Fig. 4, *c*). Further temperature increases lead to a noticeable growth of β-grains.

Thus, the results of the conducted tests demonstrate that deformation of the alloy via uniaxial compression under isothermal conditions can produce a fine-grained structure at a temperature of 950 °C. Lowering the deformation temperature below 950 °C leads to significant localization of plastic deformation, while increasing it results in the complete dissolution of the O-phase, which severely slows the kinetics of dynamic recrystallization and prevents grain refinement. Achieving a uniform fine-grained structure throughout the entire specimen volume requires increasing the degree of deformation during processing, which is possible through multi-directional isothermal forging [8; 14; 16].

An additional effect can be achieved by annealing the billets above the polymorphic transformation temperature, which helps mitigate the inheritance of the rolling texture during subsequent forging. It was observed that heating to 1100 °C and holding for 0.5 h results in the formation of polygonal grains with an average size of 200 μm (Fig. 5, *a*). The annealed billets were subjected to multi-directional isothermal forging at 950 °C [17—19], resulting in a homogeneous microstructure with an average grain/particle size of ~1 μm (Fig. 5, *b*).

As noted earlier, the balance of strength, ductility, and heat resistance in orthorhombic titanium aluminide alloys is determined by a combination of microstructural factors: β-grain size, the dispersion, and volume fraction of strengthening α_2- and O-phase particles. The dispersion and volume fraction of the O-phase are governed by the supersaturation of alloying elements in the β-phase, which depends significantly on the selected quenching temperature. From the results, it is evident that complete dissolution of the O-phase occurs at temperatures above 950 °C. Therefore, potential quenching temperatures are in the range of 975 °C and above. The upper temperature limit is clearly constrained by β-grain growth, necessitating a study of its temperature dependence.

To determine quenching temperatures, the alloy was heated after forging in the temperature range of 950—1100 °C with a holding time of 2 h. At t = 950 °C, the β-phase grain size increased to 2 μm, and the particle size was 1 μm (Fig. 6, *a*). Heating to 975 °C resulted in

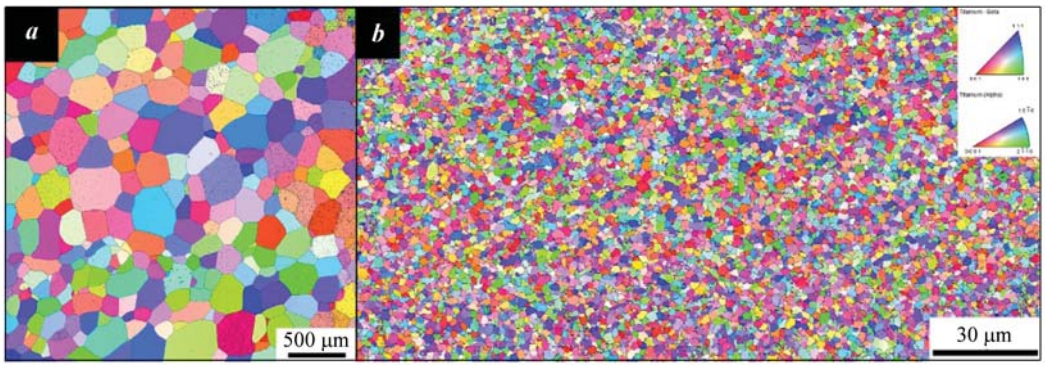

Fig. 5. Microstructure of epy VIT1 alloy after annealing at t = 1100 °C for 0.5 h (EBSD IPF map) (***a***) and after multi-directional isothermal forging at t = 950 °C, strain rate of 10^{-3} s^{-1}, and accumulative strain of 750 % (***b***)

Рис. 5. Микроструктура сплава ВИТ1 после отжига при t = 1100 °C, τ = 0,5 ч (EBSD IPF-карта) (***a***) и после всесторонней изотермической ковки при t = 950 °C, скорости деформации 10^{-3} $с^{-1}$, накопленной степени деформации 750 % (***b***)

complete dissolution of the O-phase and a reduction in the α_2-phase volume fraction from 13 to 11 vol. % (Fig. 6, *b*). The β-phase grain size increased to 4 μm, while the α_2-phase particle size remained unchanged. After heating to 1000 °C, the β-phase grain size increased to 6 μm (Fig. 6, *c*), and at 1025 °C, it reached 8 μm (Fig. 6, *d*). At these temperatures, the α_2-phase fraction decreased to 5 and 3 vol. %, respectively. Further temperature increases to 1050 and 1075 °C caused a sharp growth in β-phase grains to 50 and 100 μm, respectively, while the α_2-phase volume fraction decreased to 1—2 vol. % (Fig. 6, *e*, *f*). Complete dissolution of the α_2-phase was observed after heating and holding at 1100 °C, where the average β-phase grain size reached 200 μm (Fig. 6, *f*).

Hus, as the heating temperature for quenching increases within the range of 950—1025 °C, a gradual increase in β-grain size from 4 to 8 μm is observed. However, heating to 1050—1100 °C results in a sharp growth of β-grains due to a reduction in the α_2-phase fraction. A quenching temperature of 975 °C was preliminarily selected for determining the aging conditions.

Fig. 7 shows the evolution of the microstructure of the quenched VIT1 alloy during aging at t = 750, 800, and 850 °C for 0.5, 6, 48, and 192 h. It can be observed that, with increasing aging time, needle-shaped O-phase particles precipitate within the β-phase and form interlayers along the grain boundaries. The lower the aging temperature, the thinner the O-phase particles at all holding times (Table 1, Fig. 7). As the holding time increases, coarsening and spheroidization of the O-phase particles are observed, and, at longer holding times, some α_2-phase particles transform into the O-phase [20; 21] (Fig. 7, *g*—*l*). Thus, it was established that during aging, O-phase particles of varying dispersion precipitate, with dispersion decreasing as both temperature and holding time increase.

The change in the microhardness of the alloy correlates with the evolution of its microstructure during aging (Fig. 8). The formation of fine acicular O-phase particles at the initial stage of aging (τ = 0.5 h) leads to a sharp strengthening of the quenched alloy, with a greater effect observed at lower temperatures. With a further increase in aging time (τ > 1 h), softening occurs due to the coarsening of the O-phase particles. However, after τ > 4 h, the microhardness changes only slightly. The most significant decrease in microhardness is observed after aging times exceeding 48 h at all temperatures. This is likely due to the continued coarsening and spheroidization of the O-phase particles, along with the transformation of $\alpha_2 \rightarrow$ O. The fact that the microhardness of the alloy stabilizes after the initial softening suggests a certain structural stabilization at this stage of aging. Based

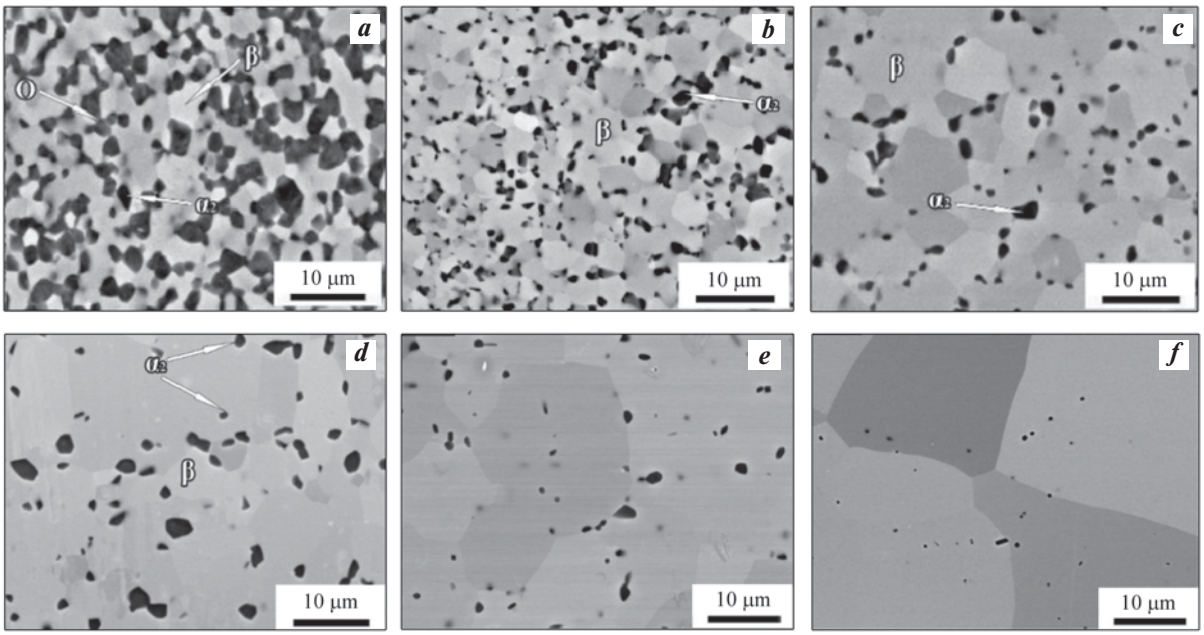

Fig. 6. Microstructure of the VIT1 alloy forged under isothermal conditions and quenched at various temperatures (SEM)
t, °C: ***a*** – 950, ***b*** – 975, ***c*** – 1000, ***d*** – 1025, ***e*** – 1050, ***f*** – 1075

Рис. 6. Микроструктура кованного в изотермических условиях сплава ВИТ1 после закалки при различных температурах (СЭМ)
t, °C: ***a*** – 950, ***b*** – 975, ***c*** – 1000, ***d*** – 1025, ***e*** – 1050, ***f*** – 1075

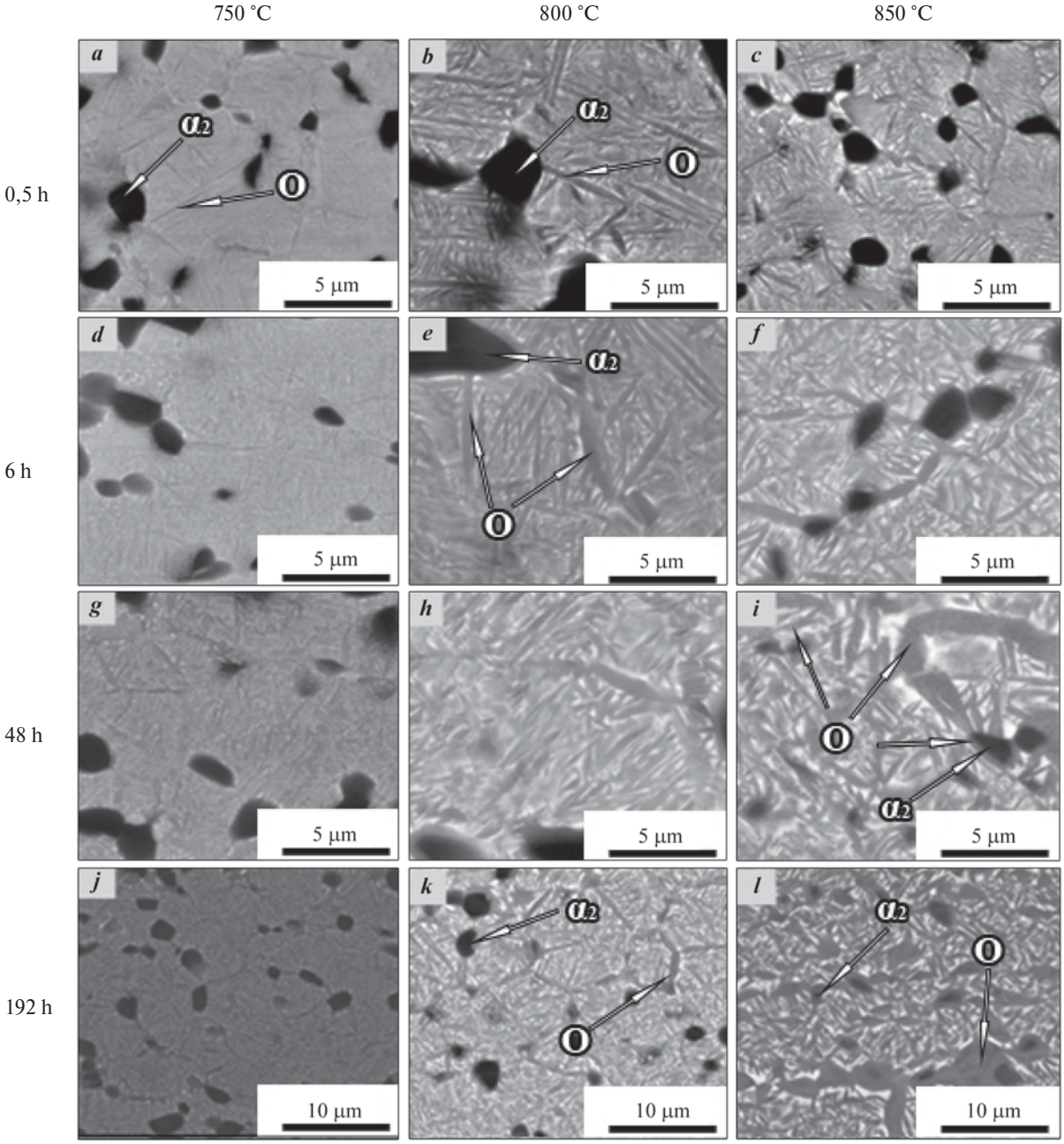

Fig. 7. Microstructure of the VIT1 alloy after quenching at $t = 975$ °C and aging (SEM)

Рис. 7. Микроструктура сплава ВИТ1 после закалки с $t = 975$ °C и старения (СЭМ)

on these findings, an aging time of 6 h was selected for further studies.

The results of tensile testing for the alloy after heat treatment (quenching at $t = 975$ °C, holding for 2 h, and aging at $t = 750$, 800, and 850 °C for 6 h [22]) are presented in Table 2. It is evident that the lowest aging temperature corresponds to the highest strength ($\sigma_u = 1450$ MPa) and the lowest ductility ($\delta = 2$ %). Increasing the aging temperature to 800 °C slightly reduces the yield strength but significantly increases ductility to 6.2 %. Further increasing the aging temperature to 850 °C reduces σ_u to 1200 MPa while raising δ to 8.0 %. Meanwhile, creep testing at $t = 650$ °C and $\sigma = 380$ MPa for the alloy aged at $t = 800$ °C revealed a time-to-failure of only $\tau = 40$ h. This short time-to-failure is evidently related to the small β-grain size (4 μm) in this alloy state (Table 2).

Therefore, additional studies were conducted to evaluate the mechanical properties of the alloy with larger β-grain sizes. To achieve coarser grains, the quenching temperature was increased to 1000 and 1025 °C, while the aging temperature was maintained at 850 °C to

Table. 1. **Thickness of O-phase particles after quenching at t = 975 °C and aging**

Таблица 1. Толщина частиц О-фазы после закалки с t = 975 °C и старения

t, °C	Thickness of O-phase particles, nm, at τ, h					
	0,5	6	12	48	96	192
750	65 ± 15	68 ± 25	70 ± 30	95 ± 35	100 ± 30	120 ± 50
800	70 ± 20	100 ± 30	130 ± 40	150 ± 40	180 ± 50	230 ± 100
850	75 ± 35	120 ± 70	160 ± 75	190 ± 20	240 ± 111	310 ± 120

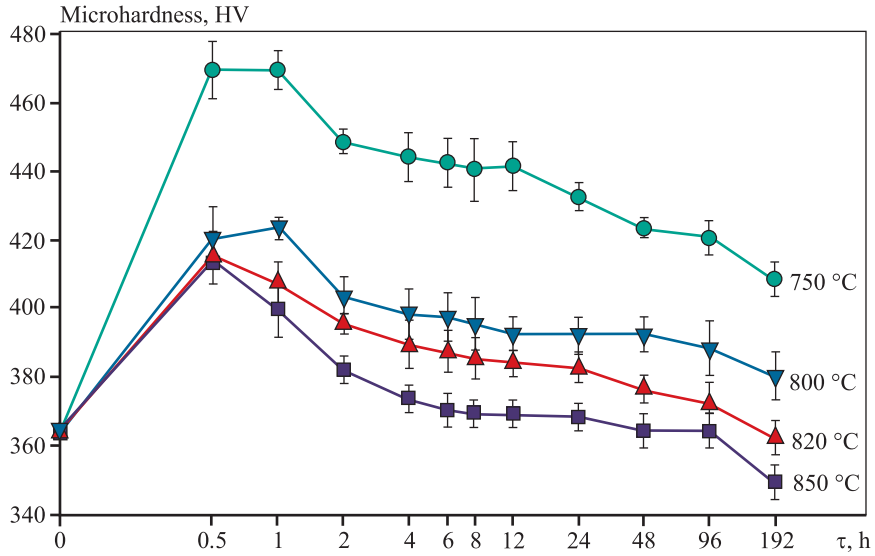

Fig. 8. Dependence of the microhardness of the VIT1 alloy after quenching (t = 975 °C) and aging (t = 750÷850 °C) on holding time

Рис. 8. Зависимость микротвердости сплава ВИТ1 после закалки (t = 975 °C) и старения (t = 750÷850 °C) от времени выдержки

compensate for the loss of ductility (Table 2). The most balanced combination of strength (σ_u = 1260 МПа), ductility (δ = 5.8 %), and time-to-failure (299 h) was observed with a β-grain size of 12 μm, achieved after heat treatment under the following conditions: quenching at t = 1025 °C, holding for 4 h, and aging at t = = 850 °C for 6 h. The obtained mechanical properties surpass those reported in [1; 2], where the VIT1 alloy subjected to multi-stage forging and rolling followed by heat treatment demonstrated σ_u = 1150 MPa and δ = = 4 %. A clear advantage of using multi-directional isothermal forging as a preliminary processing step is the significant improvement in hot ductility, which is characteristic of fine-grained alloys [23—26].

Conclusions

1. The effect of hot deformation by uniaxial compression in the temperature range of 850—1050 °C on the mechanical behavior and structural evolution of the VIT1 alloy in a hot-rolled coarse-grained state was investigated. It was shown that the most intense microstructure refinement (average grain size ~1 μm) occurs in the (α_2 + β + O)-phase region at 950 °C due to active dynamic recrystallization and spheroidization. As the temperature increases and transitions into the (α_2 + β)-phase region, the activation of dynamic recovery, caused by the dissolution of O-phase particles, reduces the degree of microstructure refinement.

2. Multi-directional isothermal forging of hot-rolled VIT1 billets at 950 °C with a total strain of 750 % produced forgings with a homogeneous fine-grained structure (~1 μm grain size). It was demonstrated that the uniformity of the microstructure could be improved by preliminary annealing at 1100 °C. The temperature dependence of grain size in fine-grained billets revealed a gradual increase from 4 to 8 μm in the range of 950—1025 °C (2-hour hold), with a sharp growth to

Table. 2. **Mechanical properties of the VIT1 alloy after forging and heat treatment**

Таблица 2. Механические свойства сплава ВИТ1 после ковки и термической обработки

Heat treatment			Size of β-grains, μm	$\sigma_{0.2}$, MPa	σ_u, MPa	δ, %	Time-to-failure, h, at t = 650 °C and σ = 380 MPa
t_{quen}, °C	t_{aging}, °C	τ, h					
975	750	2 6	4	1340 ± 25	1450 ± 30	2.0 ± 0.2	–
975	800	2 6	4	1280 ± 20	1420 ± 30	6.2 ± 0.3	40
975	850	2 6	4	1020 ± 20	1200 ± 25	8.0 ± 0.5	–
1000	800	2 6	6	1230 ± 30	1350 ± 35	6.0 ± 0.4	100
1025	800	2 6	8	1200 ± 30	1300 ± 30	5.9 ± 0.4	170
1025	850	4 6	12	1180 ± 30	1260 ± 30	5.8 ± 0.3	299

50 μm at 1050 °C and further to 200 μm at 1100 °C, due to a reduction in the volume fraction of α_2-phase particles.

3. The changes in microhardness and the evolution of microstructure during the aging of the quenched alloy were studied. It was found that the formation of fine acicular O-phase particles at the initial stage leads to a sharp strengthening of the quenched alloy, with a greater effect observed at lower temperatures. Prolonged aging results in softening caused by the coarsening and spheroidization of O-phase particles, as well as α_2-phase degradation due to the $\alpha_2 \rightarrow O$.

4. Based on the conducted studies, the quenching temperature range (975—1025 °C) and aging temperature range (750—850 °C) were selected to ensure a balance of strength, ductility, and heat resistance in the alloy processed by multi-directional isothermal forging. Mechanical testing results indicate that quenching at 1025 °C with a 4-hour hold, followed by aging at 850 °C for 6 h, provides the most balanced combination of strength ($\sigma_{0.2}$ = 1180 MPa, σ_u = 1260 MPa), ductility (δ = 5.8 %), and heat resistance (time-to-failure of 299 h at 650 °C and 380 MPa).

References

1. NRC “Kurchatov Institute”. All-Russian Scientific Research Institute of Aviation Materials. Plates from intermetallic titanium alloy of VIT1 grade.
URL: https://catalog.viam.ru/catalog/vit1/plity-iz-intermetallidnogo-titanovogo-splava-marki-vit1/ (accessed: 28.02.2024). (In Russ.).
НИЦ «Курчатовский институт». Всероссийский научно-исследовательский институт авиационных материалов. Плиты из интерметаллидного титанового сплава марки ВИТ1. URL: https://catalog.viam.ru/catalog/vit1/plity-iz-intermetallidnogo-titanovogo-splava-marki-vit1/ (дата обращения: 28.02.2024).
2. Alekseev E.B., Nochovnaya N.A., Panin P.V. Investigation of structure and phase composition of experimental heat resistant alloy based on Ti_2AlNb intermetallide in deformed state. *Titan*. 2014;(4):12—17. (In Russ.).
Алексеев Е.Б., Ночовная Н.А., Панин П.В. Исследование структуры и фазового состава опытного жаропрочного сплава на основе интерметаллида Ti_2AlNb в деформированном состоянии. *Титан*. 2014;(4):12—17.
3. Kablov E.N., Ivanov V.I., Antashev V.G., Savel'eva Yu.G. Titanium-based alloy and product made of it. Patent 2001125968/02 (RF). 2003. (In Russ.).
Каблов Е.Н., Иванов В.И., Анташев В.Г., Савельева Ю.Г. Сплав на основе титана и изделие, выполненное из него: Патент 2001125968/02 (РФ). 2003.
4. Sui X., Wang G., Liu Q., Liu Y., Chen Y. Fabricating Ti_2AlNb sheet with tensile strength higher than 1500 MPa by hot packed rolling spark-plasma-sintered pre-alloyed Ti_2AlNb powder at the B2 + O phase field. *Journal of Alloys and Compounds*. 2021;876:160110. https://doi.org/10.1016/j.jallcom.2021.160110
5. Sui X.C., Liu Q., Luo S.Y., Liu Y.K., Li Z.L., Kang Q.X., Wang G.F. Achieving high ductility of Ti_2AlNb sheet without sacrificing the tensile strength without post heat treatment. *Materials Science & Engineering A*. 2022;840:142897. https://doi.org/10.1016/j.msea.2022.142897

6. Yang Z., Liu H., Cui Z., Zhang H., Chen F. Refinement mechanism of centimeter-grade coarse grains in as-cast Ti_2AlNb-based alloy during multi-directional forging. *Materials & Design*. 2022;225(5):111508. https://doi.org/10.1016/j.matdes.2022.111508
7. Wei J.-X., Jia Y., Zhang Y.-Y., Luo X.-Y., Zhao X.-X., Zhang C.-J., Cao S.-Z., Du Z.-H., Han J.-C. Effect of hot rolling process on the evolution of microstructure and mechanical properties of Ti_2AlNb-based alloy foil during cold rolling. *Materials Characterization*. 2024;210:113784. https://doi.org/10.1016/j.matchar.2024.113784
8. Shagiev M.R., Salishchev G.A. Microstructure and mechanical properties of nanostructured intermetallic alloy based on Ti_2AlNb. *Materials Science Forum*. 2008; 584—586(1):153—158. https://doi.org/10.4028/www.scientific.net/MSF.584-586.153
9. Nochovnaya N.A., Ivanov V.I., Alekseev E.B., Kochetkov A.S. Ways of optimizing the properties of alloys based on titanium intermetallides. *Aviatsionnye materialy i tekhnologii*. 2012;S:196—206. (In Russ.).
Ночовная Н.А., Иванов В.И., Алексеев Е.Б., Кочетков А.С. Пути оптимизации эксплуатационных свойств сплавов на основе интерметаллидов титана. *Авиационные материалы и технологии*. 2012;S: 196—206.
10. Boehlert C.J., Miracle D.B. Part II. The creep behavior of Ti—Al—Nb O + bcc orthorhombic alloys. *Metallurgical and Materials Transactions A*. 1999;30:2349—2367. https://doi.org/10.1007/s11661-999-0244-0
11. Skvortsova S.V., Il'in A.A., Mamonov A.M., Nochovnaya N.A., Umarova O.Z. Structure and properties of semifinished sheet products made of an intermetallic refractory alloy based on Ti_2AlNb. *Materials Science*. 2016;51(6):821—826. https://doi.org/10.1007/s11003-016-9907-3
12. Illarionov A.G., Demakov S.L., Vodolazsky F.V., Stepanov S.I., Illarionova S.M., Shabanov M.A., Popov A.A. Alloys based on orthorhombic titanium intermetallic compound Ti_2AlNb: phase composition, alloying, structure, properties. *Metallurgist*. 2023;(3):42—54 (In Russ.).
Илларионов А.Г., Демаков С.Л., Водолазский Ф.В., Степанов С.И., Илларионова С.М., Шабанов М.А., Попов А.А. Сплавы на основе орторомбического интерметаллида титана Ti_2AlNb: фазовый состав, легирование, структура, свойства. *Металлург.* 2023;(3): 42—54. https://doi.org/10.52351/00260827_2023_03_42
13. Goyal K., Sardana N. Mechanical properties of the Ti_2AlNb intermetallic: A review. *Transactions of the Indian Institute of Metals*. 2021;74(8):1839—1853. https://doi.org/10.1007/s12666-021-02307-5
14. Zherebtsov S., Kudryavtsev E., Kostjuchenko S., Malysheva S., Salishchev G.. Strength and ductility-related properties of ultrafine grained two-phase titanium alloy produced by warm multiaxial forging. *Materials Science and Engineering A*. 2012;536:190—196. https://doi.org/10.1016/j.msea.2011.12.102
15. Zhang Y., Tian S., Jiang H., Zhang G., Zhang S., Lin H., Wang J. Research on hot deformation behavior of Mo-containing Ti_2AlNb-based alloy. *Advanced Engineering Materials*. 2021;23(10):2100. https://doi.org/10.1002/adem.202100449
16. Wang W., Zeng W., Liu Y., Xie G., Liang X. Microstructural evolution and mechanical properties of Ti—22Al—25Nb (at. %) orthorhombic alloy with three typical microstructures. *Journal of Materials Engineering and Performance*. 2018;27:293—303. https://doi.org/10.1007/s11665-017-3040-9
17. Sokolovsky V.S., Volokitina E.I., Salishchev G.A., Bykov Yu.G., Kyaramyan K.A. Method of manufacturing gas turbine engine blades from intermetallic alloy based on orthorhombic titanium aluminide: Patent 2800270 (RF). 2023. (In Russ.).
Соколовский В.С., Волокитина Е.И., Салищев Г.А., Быков Ю.Г., Кярамян К.А. Способ изготовления лопаток газотурбинных двигателей из интерметаллидного сплава на основе орторомбического алюминида титана: Патент 2800270 (РФ). 2023.
18. Sokolovsky V.S., Volokitina E.I., Salishchev G.A., Bykov Yu.G., Kyaramyan K.A. Method of manufacturing gas turbine engine blades from an alloy based on orthorhombic titanium aluminide: Patent 2790704 (RF). 2023. (In Russ.).
Соколовский В.С., Волокитина Е.И., Салищев Г.А., Быков Ю.Г., Кярамян К.А. Способ изготовления лопаток газотурбинных двигателей из сплава на основе орторомбического алюминида титана: Патент 2790704 (РФ). 2023.
19. Sokolovsky V.S., Volokitina E.I., Salishchev G.A., Bykov Yu.G., Kyaramyan K.A. Method of manufacturing gas turbine engine blades from deformed blanks of orthorhombic titanium aluminide based alloys: Patent 2790711 (RF). 2023. (In Russ.).
Соколовский В.С., Волокитина Е.И., Салищев Г.А., Быков Ю.Г., Кярамян К.А. Способ изготовления лопаток газотурбинных двигателей из деформированных заготовок сплава на основе орторомбического алюминида титана: Патент 2790711 (РФ). 2023.
20. Khadzhieva O.G., Illarionov A.G., Popov A.A. Effect of aging on structure and properties of quenched alloy based on orthorhombic titanium aluminide Ti_2AlNb. *The Physics of Metals and Metallography*. 2014;115:12—20. https://doi.org/10.7868/S0015323014010094

Хаджиева О.Г., Илларионов А.Г., Попов А.А. Влияние старения на структуру и свойства закаленного сплава на основе орторомбического алюминида титана (Ti_2AlNb). *Физика металлов и металловедение*. 2014;115(1):14—22.

21. He D., Li L., Chi J., Zhang H., Zhang G., He G., Yan J., Zhang H., Guo W. Promoted phase transformation of α_2 to O in Ti_2AlNb alloy with improved mechanical performance via laser shock peening. *Materials & Design*. 2023;229:111900. https://doi.org/10.1016/j.matdes.2023.111900
22. Sokolovsky V.S., Volokitina E.I., Salishchev G.A., Bykov Yu.G., Kyaramyan K.A. Method of manufacturing gas turbine engine blades from Ti2AlNb aluminide-based alloys: Patent 2801383 (RF). 2023. (In Russ.).
Соколовский В.С., Волокитина Е.И., Салищев Г.А., Быков Ю.Г., Кярамян К.А. Способ изготовления лопаток газотурбинных двигателей из сплава на основе алюминида Ti_2AlNb: Патент 2801383 (РФ). 2023.
23. Kaibyshev O.A. Superplasticity of alloys, intermetallics and ceramics. Berlin: Springer-Verlag, 1992. 317 p.
24. Qu S.J., Feng A.H., Shagiev M.R., Xie H., Li B.B., Shen J. Superplastic behavior of the fine-grained Ti—21Al—18Nb—1Mo—2V—0.3Si intermetallic alloy. *Letters on Materials*. 2018;8(4s):567—571. https://doi.org/10.22226/2410-3535-2018-4-567-571
25. Wang W., Zeng W., Xue C., Liang X., Zhang J. Microstructure control and mechanical properties from isothermal forging and heat treatment of Ti—22Al—25Nb (at.%) orthorhombic alloy. *Intermetallics*. 2015;56:79—86. http://dx.doi.org/10.1016/j.intermet.2014.07.011
26. Wu Y., Fan R.-L., Zhou X.-J., Chen M.-H. Microstructure and hot flow stress at 970 °C of various heat-treated Ti_2AlNb sheets. *Rare Metals*. 2020;39(6):695—706. https://doi.org/10.1007/s12598-020-01408-2

Information about the authors

Vitaly S. Sokolovsky – Cand. Sci. (Eng.), Researcher of the Laboratory of Bulk Nanostructured Materials, Belgorod State National University.
https://orcid.org/0000-0002-4363-3604
E-mail: sokolovskiy@bsu.edu.ru

Elena I. Nozdracheva – Junior Researcher of the Laboratory of Bulk Nanostructured Materials, Belgorod State National University.
https://orcid.org/0000-0001-9554-2651
E-mail: nozdracheva@bsu.edu.ru

Karen A. Kyaramyan – Head of the Metallurgical Production Department of the Branch of JSC "United Engine Corporation" "Research Institute of Technology and Organization of Engine Production".
E-mail: om-niid@uecrus.com

Yuri G. Bykov – Cand. Sci. (Eng.), Chief Specialist of the Metallurgical Production Department of the Branch of JSC "United Engine Corporation" "Research Institute of Technology and Organization of Engine Production".
E-mail: om-niid@uecrus.com

Evgeny B. Alekseev – Cand. Sci. (Eng.), Head of Sector of the Department "Titanium, magnesium, beryllium and aluminum alloys" of the Laboratory No. 8, All-Russian Scientific Research Institute of Aviation Materials of the National Research Centre "Kurchatov Institute".
E-mail: hiten_@mail.ru

Gennady A. Salishchev – Dr. Sci. (Eng.), Professor, Head of the Laboratory of Bulk Nanostructured Materials, Belgorod State National University.
https://orcid.org/0000-0002-0815-3525
E-mail: salishchev_g@bsu.edu.ru

Информация об авторах

Виталий Сергеевич Соколовский – к.т.н., науч. сотрудник лаборатории объемных наноструктурных материалов Белгородского государственного национального университета (НИУ «БелГУ»).
https://orcid.org/0000-0002-4363-3604
E-mail: sokolovskiy@bsu.edu.ru

Елена Ивановна Ноздрачева – мл. науч. сотрудник лаборатории объемных наноструктурных материалов НИУ «БелГУ».
https://orcid.org/0000-0001-9554-2651
E-mail: nozdracheva@bsu.edu.ru

Карен Абовович Кярамян – начальник отдела металлургического производства филиала АО «Объединенная двигателестроительная корпорация» «Научно-исследовательского института технологии и организации производства двигателей» (филиал АО «ОДК» «НИИД»).
E-mail: om-niid@uecrus.com

Юрий Геннадьевич Быков – к.т.н., гл. специалист отдела металлургического производства филиала АО «ОДК» «НИИД».
E-mail: om-niid@uecrus.com

Евгений Борисович Алексеев – к.т.н., начальник сектора научно-исследовательского отдела «Титановые, магниевые, бериллиевые и алюминиевые сплавы» лаборатории № 8 Всероссийского научно-исследовательского института авиационных материалов Национального исследовательского центра «Курчатовский институт».
E-mail: hiten_@mail.ru

Геннадий Алексеевич Салищев – д.т.н., профессор, заведующий лабораторией объемных наноструктурных материалов НИУ «БелГУ».
https://orcid.org/0000-0002-0815-3525
E-mail: salishchev_g@bsu.edu.ru

Contribution of the authors

V.S. Sokolovsky – conducted microstructural examinations and mechanical tests, wrote the paper.

E.I. Nozdracheva – conducted studies to determine the chemical composition of the alloy and performed mechanical tests.

K.A. Kyaramyan – analyzed the effect of processing conditions on the alloy's microhardness, participated in result discussions.

Yu.G. Bykov – analyzed the effect of processing conditions on the mechanical properties of the alloys, participated in result discussions.

E.B. Alekseev – analyzed microstructural studies, participated in result discussions.

G.A. Salishchev – defined the aim of the study and the research concept, wrote the paper, and participated in result discussions.

Вклад авторов

В.С. Соколовский – проведение микроструктурных исследований и механических испытаний, написание статьи.

Е.И. Ноздрачева – проведение исследований по определению химического состава сплава и механических испытаний.

К.А. Кярамян – анализ результатов влияния режимов обработки на микротвердость сплава, обсуждение результатов.

Ю.Г. Быков – анализ результатов влияния режимов обработки на механические свойства сплавов, обсуждение результатов.

Е.Б. Алексеев – анализ микроструктурных исследований, обсуждение результатов.

Г.А. Салищев – определение цели работы и концепции исследований, написание статьи, обсуждение результатов.

The article was submitted 29.02.2024, revised 03.05.2024, accepted for publication 23.05.2024

Статья поступила в редакцию 29.02.2024, доработана 03.05.2024, подписана в печать 23.05.2024

ENERGY AND RESOURCE SAVING / ЭНЕРГО- И РЕСУРСОСБЕРЕЖЕНИЕ

UDC 66-9
https://doi.org/10.17073/0021-3438-2025-1-80-90

Research article
Научная статья

Enhancing efficiency and modeling the operation of the afterburning chamber in the Vanyukov furnace

V.A. Kirsanov[1], **Yu.F. Poberezhny**[1], **N.G. Mikhailov**[1], **M.M. Sladkov**[2], **S.N. Gotenko**[2]

[1] **Ural Research and Design Institute of Mining Processing, Metallurgy, Chemistry, Standartization**
87 Khokhryakov Str., Ekaterinburg 620063, Russia

[2] **Sredneuralsky Copper Smeltery**
1 Sredneuralskaya Str., Revda 623280, Russia

✉ Nikolai G. Mikhailov (Mikhaylov_NG@umbr.ru)

Abstract: This study investigates the process of enhancing the efficiency of the afterburning chamber in the Vanyukov furnace. Various operational modes of the furnace and the chamber were analyzed to identify optimal conditions for sulfur oxidation and afterburning, as well as methods for reducing accretions. Measurements and analyses of off-gas compositions were conducted, and the dust content was determined. Simplifications and assumptions were applied in the calculations, enabling the modeling of gas flow, thermodynamic processes, velocity profiles, and interaction zones. Some thermodynamic calculations of counter-penetrating gas jets were based on hypotheses derived from heat exchange theories in mixing devices. Experimental results of numerical modeling and predictive simulations within the afterburning chamber are presented. Parameters were measured, and aerodynamic characteristics of the tuyeres were charted at an average oxygen supply to the chamber of no more than 2500 n.m^3/h (38 n.m^3 per ton of batch load). Recommendations for effective technological operations were proposed. The expertise of specialists from the Sredneuralsk Copper Smelter, along with the results of trials and process modeling, facilitated the selection of the optimal tuyere air distribution. The findings reveal the complexity of aerodynamic and thermodynamic processes occurring within the afterburning chamber. These include interactions between tuyere cooling airflows, heat release from exothermic oxidation reactions, and forced and natural convection of off-gases with varying temperature gradients, all visualized within a single projection.

Keywords: afterburning chamber, improving efficiency, modeling, Vanyukov process.

For citation: Kirsanov V.A., Poberezhny Yu.F., Mikhailov N.G., Sladkov M.M., Gotenko S.N. Enhancing efficiency and modeling the operation of the afterburning chamber in the Vanyukov furnace. *Izvestiya. Non-Ferrous Metallurgy.* 2025;31(1):80–90.
https://doi.org/10.17073/0021-3438-2025-1-80-90

Повышение эффективности и моделирование использования камеры дожигания в печи Ванюкова

В.А. Кирсанов[1], **Ю.Ф. Побережный**[1], **Н.Г. Михайлов**[1], **М.М. Сладков**[2], **С.Н. Готенко**[2]

[1] **Уральский научно-исследовательский и проектный институт обогащения и механической обработки полезных ископаемых**
Россия, 620063, Свердловская обл., г. Екатеринбург, ул. Хохрякова, 87

[2] **Среднеуральский медеплавильный завод**
Россия, 623280, Свердловская обл., г. Ревда, ул. Среднеуральская, 1

✉ Николай Григорьевич Михайлов (Mikhaylov_NG@umbr.ru)

Аннотация: В исследуемом процессе повышения эффективности использования камеры дожигания в печи Ванюкова изучены различные эксплуатационные варианты работы печи и камеры, найдены режимы оптимального окисления и дожигания серы, выявлены способы снижения настылеобразования. Проведены измерения и анализ отходящих газов. Определен состав пыли.

По результатам выполненных расчетов применяли ряд упрощений и допущений, позволяющих представлять движение газов, термодинамические процессы, профиль скоростей, области взаимодействия. Некоторые варианты термодинамических расчетов взаимопроникающих встречных струй построены на гипотезах, заимствованных из теории теплообмена в смешивающих аппаратах. Представлены экспериментальные результаты численного моделирования и варианты некоторых прогнозных симуляций, происходящих в камере дожигания печи Ванюкова. Проведены замеры параметров, построены графики аэродинамических характеристик фурм при среднем значении подачи кислорода в пространство камеры дожигания не более 2500 н.м^3/ч (38 н.м^3/т загрузки шихты). Предложены мероприятия для эффективной технологической эксплуатации. Опыт специалистов Среднеуральского медеплавильного завода, результаты испытаний и моделирования процесса способствовали выбору наилучшего распределения дутья по фурмам. Полученные результаты свидетельствуют о достаточно сложных аэродинамических и термодинамических процессах, происходящих в пространстве камеры дожигания, представлении в одной проекции взаимодействий явлений динамики фурменных дутьевых потоков охлаждения, выделения тепловой энергии экзотермических реакций окисления, принудительной и естественной конвекции отходящих расплавных газов с различными температурными градиентами.

Ключевые слова: камера дожигания, повышение эффективности, моделирование, процесс Ванюкова.

Для цитирования: Кирсанов В.А., Побережный Ю.Ф., Михайлов Н.Г., Сладков М.М., Готенко С.Н. Повышение эффективности и моделирование использования камеры дожигания в печи Ванюкова. *Известия вузов. Цветная металлургия*. 2025;31(1):80–90. https://doi.org/10.17073/0021-3438-2025-1-80-90

Introduction

The domestic smelting technology — known as the Vanyukov process, employed for processing sulfide-copper concentrates — has several advantages over foreign analogs, including high specific productivity, process flexibility, simplicity and reliability of the metallurgical unit, and low capital and operating costs. The smelting technology, in general, can be characterized as a semi-autogenous process [1—3].

During the testing period, the charge materials composition was as follows (wt. %): Cu — 17.97, S — 26.16, SiO — 15.28, Zn — 1.75, Pb — 0.25, others — 38.59.

In the horizontal section, the furnace consists of smelting-oxidation and sedimentation zones, while in the vertical section, it is divided into superstratum, supra-tuyere, and sub-tuyere zones. The furnace, in cross-section, is a rectangular-trapezoidal unit into which the blast is introduced through tuyeres. Charge materials are fed into the working space of the unit via loading devices. During the first stage of processing, heating, oxidation, and melting of the charge materials dominate [4]. The process characteristics are heavily influenced by the chemical, mineralogical, and granulometric composition of the ore [5]. In the supra-tuyere zone, processes such as melting, dissolution of refractory components, sulfide oxidation, and the coalescence of matte droplets take place [6—8]. Oxidation of off-gases occurs in the afterburning chamber, which is equipped with four tuyeres.

The issues related to improving efficiency and the simulation and optimization of the afterburning chamber's operation in the Vanyukov furnace will be examined in detail, as enhancing operational energy efficiency holds both practical and theoretical significance [9].

Research methodology

The methodology for determining the optimal modes of blast supply to the tuyere row of the afterburning chamber and optimizing the sulfur afterburning process was divided into practical and methodological components, with elements of visual representation.

In the methodological component, based on the results of the calculations, a number of simplifications and assumptions were applied to model gas flow, velocity profiles [10], thermal processes, and surface interaction zones. Some thermodynamic calculations of interpenetrating counter jets were built on concepts borrowed from the theory of heat exchange in mixing devices [11; 12]. For the numerical theoretical aspects of modeling hydrodynamic characteristics, the following formulas were used:

$$W_2 = [0.5gh^{-1}Ld^{-1}\gamma_0\mu(1 + \beta t)]^{0.5}, \quad (1)$$

$$\mathrm{Re} = Wd_t/\nu, \quad (2)$$

where γ_0 — specific mass of the gas; β — coefficient of volumetric gas expansion; L — space length; d — space diameter; h — geometric head; g — gravitational acceleration; μ — friction coefficient; t — temperature; ν — viscosity coefficient; W — blast velocity; W_2 — gas flow velocity; d_t — tuyere outlet diameter; Re — Reynolds number (dimensionless coefficient).

During the numerical modeling of heat release in the afterburning chamber, combustion reactions of sulfur and sulfur dioxide were considered:

$$S + O_2 = SO_2 + 297\ \mathrm{kJ}, \quad (3)$$

$$2SO_2 + O_2 = 2SO_3 + 192\ \mathrm{kJ}. \quad (4)$$

To analyze the thermal processes in the studied O_{xyz} space, the area of off-gas flow, A, was divided into grid

sections ΔN_1, ΔN_2, ..., ΔN_n with volumes ΔV_1, ΔV_2, ..., ΔV_n. The integral sum for the function $f(x,y,z)$ over area A is given by

$$M_n = \sum f(x_j, y_j, z_j)\Delta V_j. \quad (5)$$

The volumetric region of heat release from the jet streams was determined as:

$$\int dx \int dy \int f(x,y,z)dz, \quad (6)$$

$$a \le x \le b,\ c \le y \le e,\ m \le z \le n. \quad (7)$$

For each operational mode, technological data were monitored, and the composition of the off-gases was determined. Based on the balance indicators, the afterburning efficiency was evaluated (Table 1).

Table 1 includes the following parameters: S_a — amount of sulfur dioxide after the afterburning chamber; S_v — sulfur content in dust; S_{sh} — sulfur content in the charge materials; K_v — oxygen concentration in the off-gases exiting the afterburning chamber; K_d — oxygen supplied to the afterburning chamber.

To determine afterburning efficiency, the oxygen and gas blast parameters at the furnace's tuyere rows were recorded. Oxygen was supplied for afterburning at a rate not exceeding 2500 n.m^3/h (38 n.m^3 per ton of charge). Operating parameters were determined using measurement instrument readings. For comprehensive analysis, data from the information system's hourly and shift reports on furnace performance were used. Information on the composition of matte, slag, and dust was considered, and the composition of off-gases was analyzed.

Table. 1. **Combustion efficiency assessment**

Таблица 1. Оценка полноты сжигания

Mode	S_{sh}	S_a	S_v	K_v	K_d	Effect
Baseline	const	↕	↕	↕	↕	
1	const	↑	↓	↑	↑	+
2	const	↓	↑	↓	↓	–
3	const	↑	↓	↕	↕	+
4	const	↓	↑	↑	↕	–

Note. ↑ – increase, ↓ – decrease, ↕ – baseline values, «+» or «–» – indicates the afterburning efficiency achieved.

Results and discussion

In the studied gas flow process, the operational features of the afterburning chamber and the dynamic effects of jets emerging from the furnace tuyeres were examined, despite the presence of thermal and gas-dynamic inhomogeneities. Various operational modes of the furnace and afterburning chamber were analyzed, leading to the identification of optimal oxidation regimes and methods for enhancing the efficiency of accretion reduction. Schematic of the tuyere row is presented in Fig. 1.

During the tests, the oxygen pressure at the tuyere was regulated using shut-off and control valves, with the pressure readings recorded on the installed manometer, as well as the flow rate monitored via the information system. The resulting characteristics are presented in Fig. 2 and Table 2.

The provided tuyere characteristics enable individual regulation of the oxygen flow rate through each tuyere in varying proportions, while maintaining an approximate overall oxygen supply to the afterburning chamber depending on the furnace load.

A more detailed examination of the blast supply through the tuyeres of the afterburning chamber reveals that, due to turbulence, the free jet mixes with the surrounding medium as it moves away from the source. Free boundary layer forms within the jet, expanding

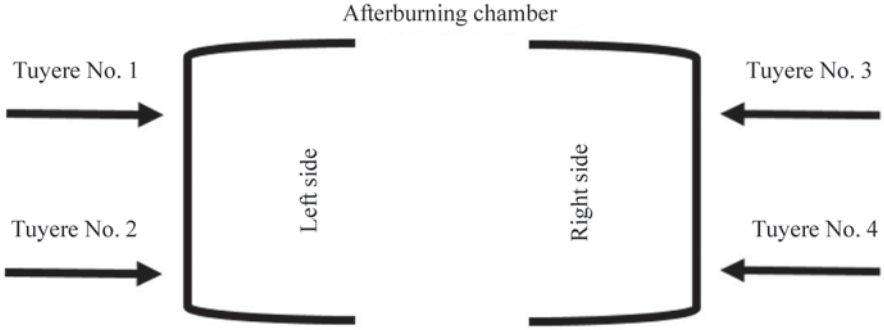

Fig. 1. Afterburning chamber tuyeres

Рис. 1. Фурмы камеры дожигания

Table. 2. **Calculated blast velocity modes**

Таблица 2. Расчетные скорости дутьевых режимов

Right side of the afterburning chamber						Left side of the afterburning chamber					
Tuyere *1*			Tuyere *2*			Tuyere *3*			Tuyere *4*		
W, m/s	Re, 10^4		*W*, m/s	Re, 10^4		*W*, m/s	Re, 10^4		*W*, m/s	Re, 10^4	
102.1	26–67	min	93.8	24–60	min	74.1	19–60	min	81.66	21–61	min
124.3			105.9			93.8			102.83		
142.2			118.0			110.4			115.69		
155.0			133.1			128.5			134.59		
166.3			143.7			139.1			146.69		
189.0		max	163.3		max	158.8		max	166.35		max
211.7			181.5			177.7			181.47		
242.7			196.6			196.6			201.13		
264.6			219.3			214.7			219.27		
			235.9			234.4			240.45		

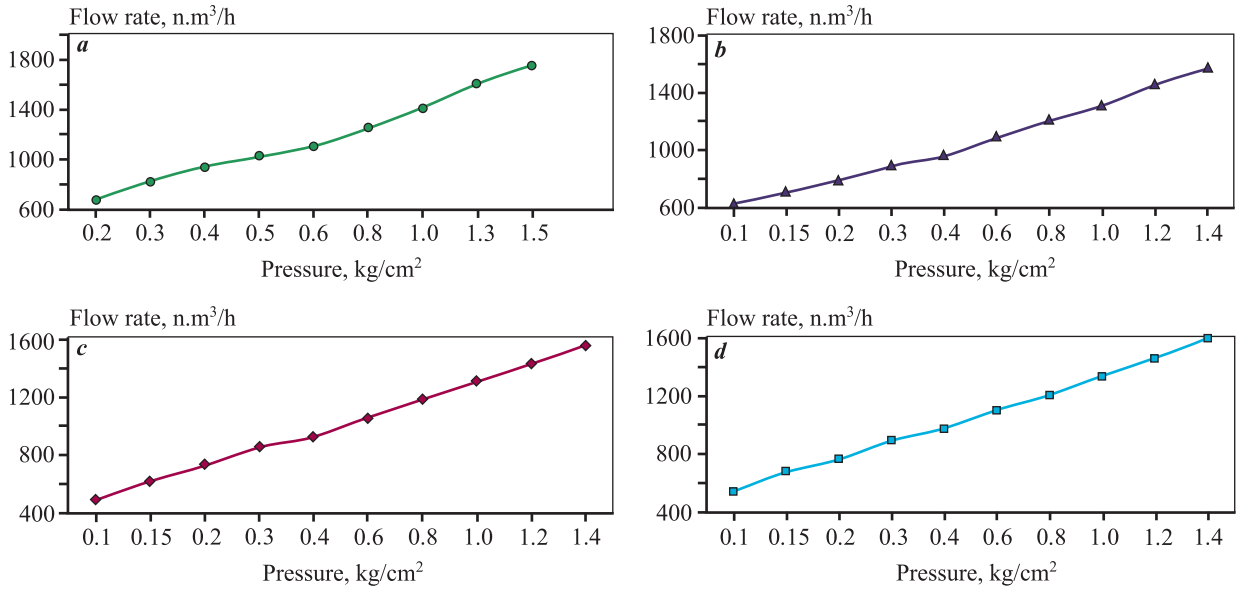

Fig. 2. Oxygen flow rate as a function of pressure

a – left side of the afterburning chamber, tuyere *1*; ***b*** – left side of the afterburning chamber, tuyere *2*;
c – right side of the afterburning chamber, tuyere *3*; ***d*** – right side of the afterburning chamber, tuyere *4*

Рис. 2. Зависимости расхода кислорода от давления

a – левая сторона камеры дожигания, фурма *1*; ***b*** – левая сторона камеры дожигания, фурма *2*;
c – правая сторона камеры дожигания, фурма *3*; ***d*** – правая сторона камеры дожигания, фурма *4*

outward from the nozzle, with primary mixing beginning at this boundary. This velocity adjustment within the jet leads to the formation of vortex regions in the cross-sectional plane. In other words, the most active interaction area is the collision point of the jets. This is because the velocities of the opposing jets are similar, causing the laminar flow zone to transition into turbulence [13—15]. Fig. 3 illustrates the vortex collision structures at relatively similar velocities of the opposing jets.

Due to the characteristics of off-gas flow and the non-uniformity caused by the connection of the furnace's tuyere rows and its geometry, jet flow modeling in the afterburning chamber represents a specific case [16—26].

The concentration of thermal energy in the jet interaction zones was calculated for both sulfur oxidation and

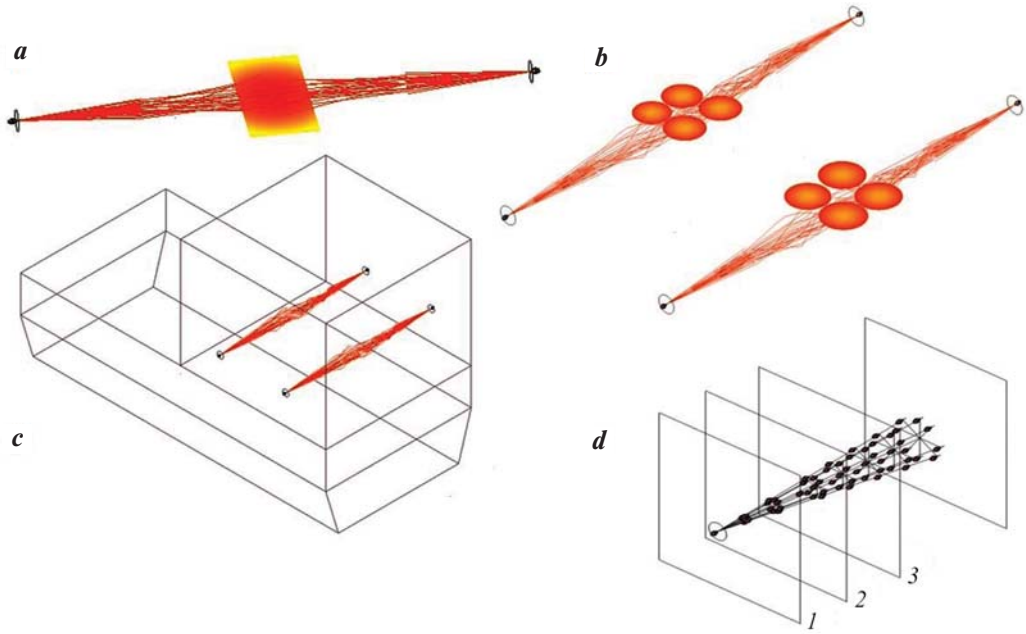

Fig. 3. Vortex collision structures

a – thermal zone of vortex collision; ***b*** – thermal structure of vortex collision; ***c*** – free turbulent jets in the afterburning chamber space; ***d*** – sections of a free turbulent jet: laminar (***1***), transitional (***2***), fully turbulent (***3***)

Рис. 3. Структуры вихревого соударения

a – термическая область вихревого соударения; ***b***– термическая структура вихревого соударения; ***c*** – свободные турбулентные струи в пространстве камеры дожигания; ***d*** – участки свободной турбулентной струи: ламинарный (***1***), переходной (***2***) и свободный турбулентный (***3***)

natural gas combustion processes. It was assumed that the Mach number for jets during sulfur oxidation does not exceed 0.52.

The calculated surface areas were determined for the jet collision zones and the jet flow regions. Within the boundaries of the interaction zone, a geometric figure was constructed with its axis aligned to the axis of the analyzed regions. Using polynomial distribution, it was assumed that a certain amount of sulfur is probabilistically combusted within the surface interaction zone.

As a result, the following volumetric heat loads were obtained: 500—1500 kW for oxidation processes and 1100—2200 kW for natural gas combustion. The normative heat load values for these processes were applied to the volumetric space of the afterburning chamber, while the actual heat load was determined based on the constructed surface interaction zones. The results are summarized in Table 3.

Examples of gas flow and jet stream are shown in Fig. 4.

The three-dimensional representation of the gas flows in the furnace reveals a variety of circulation zones. Velocity adjustments lead to the dominant jet, with the highest momentum and exit velocity, restructuring the opposing jet. This results in displacement starting from the turbulent boundary layer, causing jet separation. The flows enveloping the restructured jet acquire turbulent properties and a lower velocity, vectorially directed toward the boundaries of the afterburning chamber space. Considering the dynamics of opposing jets, it can be concluded that changes in velocity characteristics not only alter the thermal interaction zone but also influence the exhaust gas flow. It has been established that the structure of the collision zone depends on the design and operational parameters of the jet flow's swirl [26, 27]. Understanding the behavior of opposing colliding jets can be utilized for cleaning and preventing active accretion formation, as well as optimizing sulfur

Table. 3. **Assessment of thermal energy concentrations**

Таблица 3. Оценка концентраций тепловой энергии

Process	Heat load, kW/m^3		Local heat load coefficient [26]
	Normative	Actual	
Sulfur oxidation	40	1500	37
Natural gas combustion	65	2200	34

oxidation processes. The parameters of the off-gas are presented in Table 4.

Observations indicate that the rate of tuyere fouling depends on the external environment, blast pressure, as well as the direction and composition of the particles in the exhaust gases. Dust samples were collected from several points along the gas duct: waste heat boiler, cooling tower, and electrostatic precipitator. The results of the dust composition analysis are shown in Table 5.

Comparative analysis of sulfur content in dust and charge under different operating modes of the afterburning chamber is presented in Fig. 5.

The tests revealed that sulfur afterburning regulation can be performed both quantitatively and qualitatively. Increasing oxygen supply to the afterburning chamber, up to certain limits, raises the sulfur dioxide concentration in the off-gas and reduces the sulfur mass fraction in the dust.

Using computer modeling, various cases of accretion formation on one of the afterburning chamber walls were visualized is presented in Fig. 6.

The illustrated accretion formation variants, which occur during operation as a result of dust particle sintering in the off-gas, affect the performance of the blast tuyeres. Tuyere fouling is detected either by changes in blast pressure, during tuyere cleaning, or visually through open "inspection windows".

During operation, spontaneous tuyere cleaning may

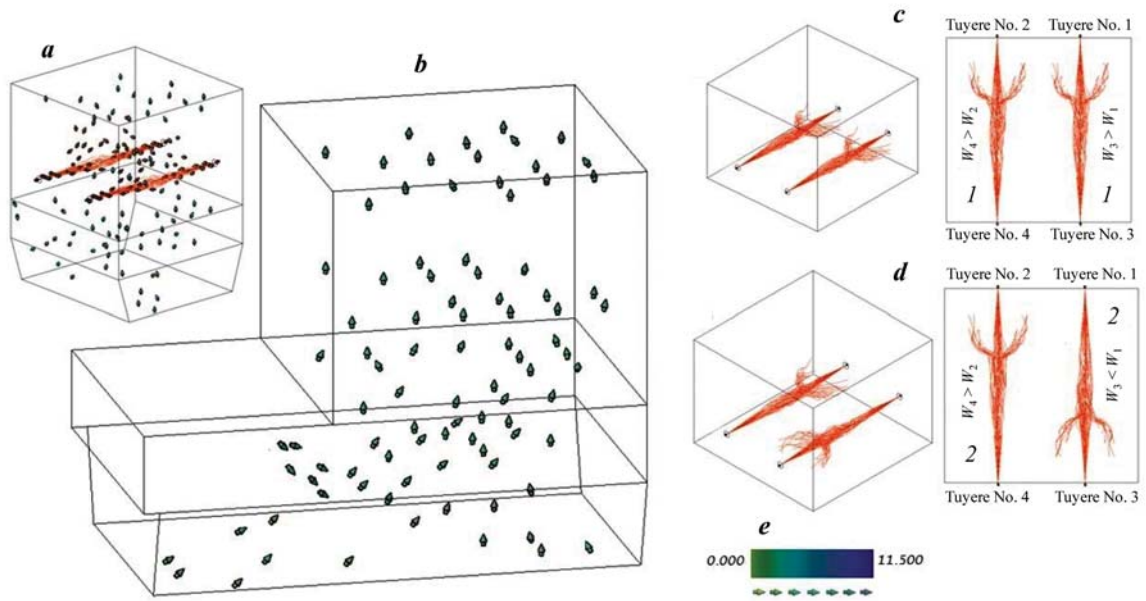

Fig. 4. Gas flow and jet stream

a – jet streams and off-gas flow; ***b*** – flow of high-temperature gases; ***c***, ***d*** – formation of collision structures at different jet velocities: ***1***, ***2*** – variations in jet velocity; ***e*** – velocity scale of high-temperature gases (m/s)

Рис. 4. Движение газов и струйный поток

a – струйный поток и движение уходящих газов; ***b*** – движение расплавных газов; ***c***, ***d*** – формирование структур соударения на разных струйных скоростях: ***1***, ***2*** – варианты скоростных изменений струй; ***e*** – шкала скорости расплавных газов, м/с

Table. 4. **Off-gas parameters**

Таблица 4. Параметры отходящих газов

Gas component	Gas density, kg/n.m^3	Mass fraction, kg/kg	Volume fraction, n.m^3/n.m^3
N_2	1.25	0.0483	0.0746
CO	1.25	–	–
CO_2	1.963	0.0768	0.0755
SO_2	2.855	0.07087	0.479
H_2O	0.863	0.139	0.334
O_2	1.427	0.027	0.0365
Note. The off-gas temperature is 1250 °C.			

occur, with the accretion breaking off due to the jet's own pressure. Installing a gas burner in the tuyeres of the third row is currently the primary method of combating accretion formation in the working space of the afterburning chamber. Table 6 shows the changes in the working space volume of the afterburning chamber due to accretion formation.

The data in Table 6 demonstrate that the working space volume of the afterburning chamber can significantly decrease due to perimetric accretion formation. This reduction leads to changes in the particle flow trajectories of the off-gases, deviations in the dynamic resistance during gas removal, and a decline in sulfur oxidation efficiency.

To determine the most efficient operation of the afterburning chamber, including the optimal oxygen flow through its tuyeres, calculation schemes and gas flow ratios were developed and evaluated for several existing and prospective operating modes. The optimal mode for the current system was identified, meeting the requirements for optimal afterburning, improved chamber efficiency, and enhanced sulfur oxidation. The results of gas composition measurements under different operating modes are presented in Table 7.

The results in Table 7 indicate that the uniformity of optimal sulfur oxidation and afterburning depends on jet dynamics. Various design options for modernizing the afterburning chamber are proposed in Fig. 7. Additional simulations and studies are necessary to confirm the effectiveness of these modernizations.

Conclusion

The findings highlight the complexity of the aerodynamic and thermodynamic processes within the afterburning chamber. The study employed turbulent jet theories and physical modeling. The blast supply was optimized for various experimental modes, with parameters measured and aerodynamic characteristics of the tuyeres charted at an average oxygen supply rate to the afterburning chamber of no more than 2500 n.m^3/h (38 n.m^3 per ton of charge). Gas analyses were performed, and the dust composition was determined at several points along the gas duct, including the waste heat boiler, cooling tower, and electrostatic precipitator.

Several schemes for modernizing the afterburning chamber and optimizing tuyere blast distribution were proposed. It was determined that the highest sulfur afterburning efficiency can be achieved by supplying a specific oxygen flow rate to each tuyere without altering the overall oxygen supply.

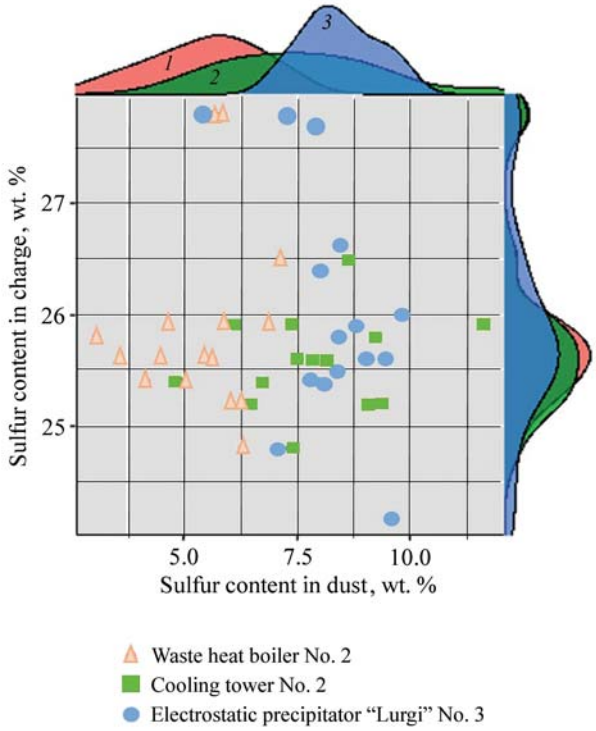

Fig. 5. Sulfur content in dust and charge under different operating modes of the afterburning chamber

1–3 – sulfur content density distribution assessment
1 – waste heat boiler No. 2; ***2*** – cooling tower No. 2;
3 – electrostatic precipitator "Lurgi" No. 3

Рис. 5. Содержание серы в пыли и шихте на разных режимах работы камеры дожигания

1–3 – оценка плотности распределения содержания серы
1 – котел-утилизатор № 2; ***2*** – башня охлаждения № 2;
3 – электрофильтр «Lurgi» № 3

Table. 5. **Dust composition, wt. %**

Таблица 5. Состав пыли, мас. %

Sampling point	Cu	S	Pb	Zn	Others
Cooling tower No. 2	19.45	5.45	3.69	3.28	68.13
Waste heat boiler No. 2	18.78	7.61	4.29	3.31	66.01
Electrostatic precipitator "Lurgi" No. 3	14.84	8.43	6.93	4.65	65.15

Table. 6. **Perimetric formation**

Таблица 6. Периметральное образование настыли

Variant	Working space volume, m^3	Thickness of wall accretion, m
1	55–59	0.1–0.2
2	49–53	0.25–0.35
3	37.5–43.0	0.50–0.65
4	34.0–37.6	0.65–0.75

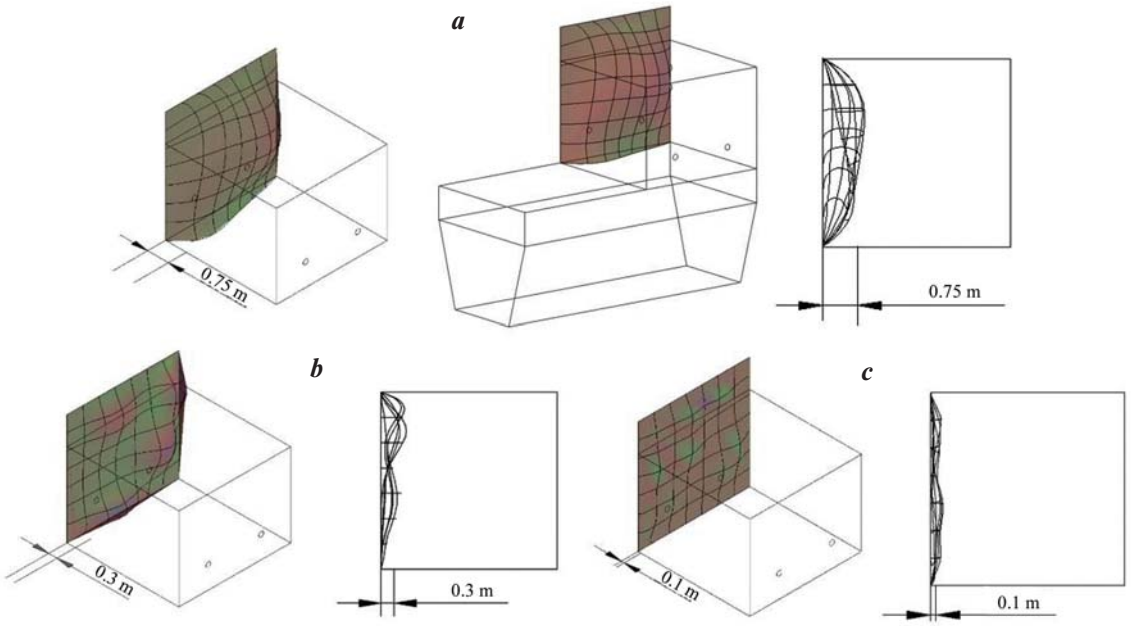

Fig. 6. Variants of accretion formation
Accretion thickness, m: ***a*** – 0.75; ***b*** – 0.3; ***c*** – 0.1

Рис. 6. Варианты настылеобразования
Толщина настыли, м: ***a*** – 0,75; ***b*** – 0,3; ***c*** – 0,1

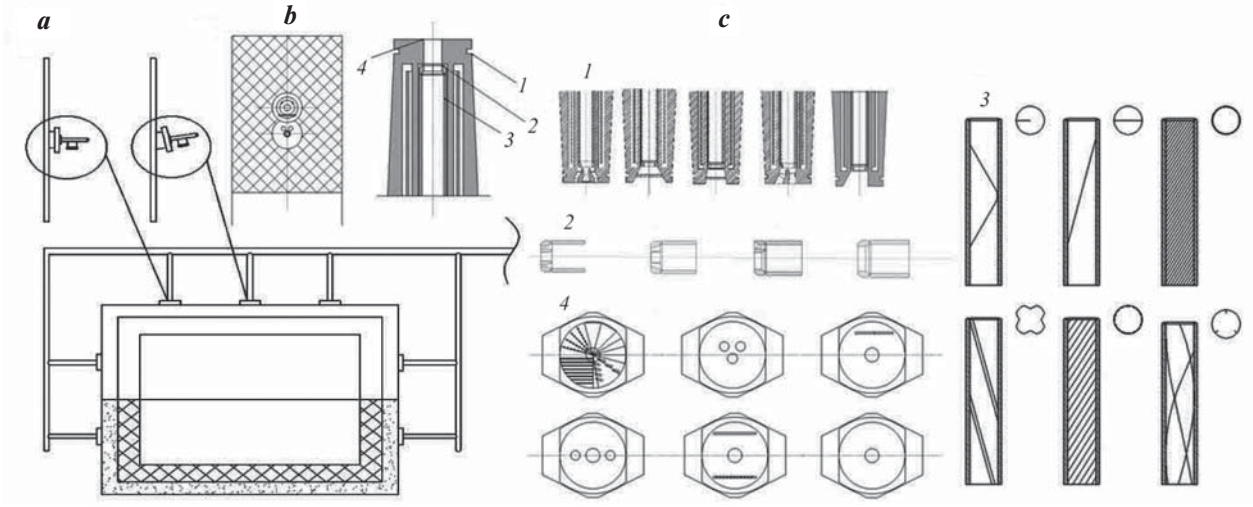

Fig. 7. Prospective options for modernizing the afterburning chamber [27–30]
a –arrangement of tuyeres in the afterburning chamber; ***b*** – multi-channel tuyere with two tiers of nozzles; ***c*** – modernization options for tuyere components: casing (***1***), sleeve (***2***), swirl inserts (***3***), and diffuser (***4***)

Рис. 7. Перспективные варианты направлений модернизации камеры дожигания [27–30]
a – вариант расположения фурм в камере дожигания; ***b*** – многоканальная фурма с двумя ярусами сопел; ***c*** – на участке фурмы варианты модернизации корпуса (***1***), втулки (***2***), вставок-завихрителя (***3***), рассекателя (***4***)

Measures for efficient operation and minimizing accretion formation in the Vanyukov furnace afterburning chamber were proposed. To implement a prospective automated operation, it is recommended to organize information tracking for each tuyere (pressure/flow rate), install regulating valves to adjust the blast flow rate to each tuyere without manual intervention, and introduce an automatic control system [31].

The expected outcomes of implementing these measures and recommendations include improved energy efficiency and operational safety, increased productivity, and enhanced control over the technological process.

Table. 7. **Off-gas composition measurements (wt.%) after afterburning in different operating modes of the afterburning chamber**

Таблица 7. Результаты измерений состава отходящих газов (мас. %) после дожигания на разных режимах эксплуатационной работы камеры дожигания

Measurement No.	First mode			Second mode		
	Oxygen supply to the afterburning chamber, $n.m^3/h$					
	2300			2500		
	SO_2	CO_2	O_2	SO_2	CO_2	O_2
1	38.0	10.4	4.0	42.4	11.0	4.5
2	40.0	10.0	4.5	41.0	10.5	4.5
3	38.0	10.4	4.6	42.0	11.0	4.5
4	39.8	10.9	4.5	42.4	11.6	5.0
5	38.4	10.4	4.7	43.0	12.0	5.0
	Average values					
	38.84	10.42	4.46	42.16	11.22	4.7

References

1. Lisienko V.G., Shchelokov Ya.M., Ladygichev M.G. Melting units: heat engineering, management and ecology. Moscow: Teplotekhnik, 2005. 912 p. (In Russ.).
Лисиенко В.Г., Щелоков Я.М., Ладыгичев М.Г. Плавильные агрегаты: теплотехника, управление и экология. М.: Теплотехник, 2005. 912 с.
2. Lisienko V.G., Shchelokov Ya.M., Ladygichev M.G. Fuel. Rational combustion, management and technological use. Moscow: Teplotekhnik, 2004. 832 p. (In Russ.).
Лисиенко В.Г., Щелоков Я.М., Ладыгичев М.Г. Топливо. Рациональное сжигание, управление и технологическое использование. М.: Теплотехник, 2004. 832 с.
3. Naboichenko S.S., Ageev N.G., Doroshkevich A.P., Zhukov V.P., Eliseev E.I. Processes and devices of non-ferrous metallurgy. Ekaterinburg: UGTU–UPI, 2005. 700 p. (In Russ.).
Набойченко С.С., Агеев Н.Г., Дорошкевич А.П., Жуков В.П., Елисеев Е.И. Процессы и аппараты цветной металлургии. Екатеринбург: УГТУ—УПИ, 2005. 700 с.
4. Sborshchikov G.S., Volodin A.M., Valavin V.S. Free convection of the melt in the furnace with a bubble layer during its blowing through a side tuyere established under the layer level. *Izvestiya. Non-Ferrous Metallurgy.* 2015;(2):58—68. (In Russ.).
Сборщиков Г.С., Володин А.М., Валавин В.С. Свободная конвекция расплава в печи с барботажным слоем при его продувке через боковую фурму, установленную под уровнем слоя. *Известия вузов. Цветная металлургия.* 2015;(2):58—68.
https://doi.org/10.17073/0021-3438-2015-2-58-68
5. Hoffman G.O. Metallurgy of copper. Sverdlovsk: GNTI, 1934. 475 p. (In Russ.).
Гофман Г.О. Металлургия меди. Свердловск: ГНТИ, 1934. 475 с.
6. Vanyukov A.V., Zaitsev V.Ya. Slags and matte of non–ferrous metallurgy. Moscow: Metallurgiya, 1969. 408 p. (In Russ.).
Ванюков А.В., Зайцев В.Я. Шлаки и штейны цветной металлургии. М.: Металлургия, 1969. 408 с.
7. Vaisburd S., Berner A., Brandon D.G., Kozhakhmetov S., Kenzhaliyev E., Zhalelev R. Slags & mattes in Vanyukov's process for the extraction of copper. *Metallurgical and Materials Transactions.* 2002;(33):551—559.
https://doi.org/10.1007/s11663-002-0034-1
8. Zhang H.L., Zhou C.Q., Bing W.U, Chen Y.M. Numerical simulation of multiphase flow in a Vanyukov furnace. *Journal of Southern African Institute of Mining and Metallurgy.* 2015;(115):457—463.
9. Anufriev V.P., Lisienko V.G., Chesnokov Yu.N., Lapteva A.V. Possibilities for implementing carbon policy in Russian regions. In: *Proceedings of the XII International conference «Russian regions in the focus of change»* (16–18 November 2017). Ekaterinburg: UMC UPI, 2018. Part 2. P. 536–550. (In Russ.).
Ануфриев В.П., Лисиенко В.Г., Чесноков Ю.Н., Лаптева А.В. Возможности реализации углеродной политики в российских регионах. В сб: *Материалы XII Международной конференции «Российские регионы в фокусе перемен»* (16—18 ноября 2017 г.). Екатеринбург: УМЦ УПИ, 2018. Ч. 2. С. 536—550.
10. Idelchik I.E. Handbook of hydraulic resistance. Moscow: Mashinostroenie, 1992. 672 p. (In Russ.).
Идельчик И.Е. Справочник по гидравлическим сопротивлениям. М.: Машиностроение, 1992. 672 с.
11. Kutateladze S.S. Fundamentals of the theory of heat transfer. Moscow: Atomizdat, 1979. 416 p. (In Russ.).
Кутателадзе С.С. Основы теории теплообмена. М.: Атомиздат, 1979. 416 с.
12. Baskakov A.P., Berg B.V., Vitt O.K., Filippovsky N.F. Teplotekhnika. Moscow: Energoatomizdat, 1991. 224 p. (In Russ.).
Баскаков А.П., Берг Б.В., Витт О.К., Филипповский Н.Ф. Теплотехника. М.: Энергоатомиздат, 1991. 224 с.

13. Abramovich G.N., Girshovich T.A., Krasheninnikov S.Yu., Secundov A.N., Smirnova I.P. Theory of turbulent jets. Moscow: Nauka, 1984. 710 p. (In Russ.).
Абрамович Г.Н., Гиршович Т.А., Крашенинников С.Ю., Секундов А.Н., Смирнова И.П. Теория турбулентных струй. М.: Наука, 1984. 710 с.
14. Colagrossi A., Marrone S., Colagrossi P., Le Touze D. Da Vinci's observation of turbulence: A French-Italian study aiming at numerically reproducing the physics behind one of his drawings, 500 years later. *Physics of Fluids*. 2021;(33):1—16. https://doi.org/10.1063/5.0070984
15. Prodanov S.A., Voronov G.V. Features of the movement of the gas medium in the above-tuyere zone of the Vanyukov furnace. In: *Materials of the V All-Russian scientific and practical conference of students, postgraduate students and young scientists* (12–13 May 2016). Ekaterinburg: UrFU, 2016. P. 91–98.
Проданов С.А., Воронов Г.В. Особенности движения газовой среды в надфурменной зоне печи Ванюкова. В сб. докл.: *Материалы V Всероссийской научно-практической конференции студентов, аспирантов и молодых ученых* (12—13 мая 2016 г.). Екатеринбург: УрФУ, 2016. С. 91—98.
16. Oliver T. Schmidt, Aaron Towne, Georgios Rigas, Tim Colonius, Guillaume A. Bres. Spectral analysis of jet turbulence. *Journal of Fluid Mechanics*. 2017;(855): 953—982. https://doi.org/10.1017/jfm.2018.675
17. Khansa Mahjoub Mohammed Merghani. Experimental study of a human-like exhaled airflow configuration and droplets dynamics in indoor environment. Paris: Universite Paris-EstCreteilVal-de-Marne, 2021. 183 p. https://theses.hal.science/tel-04022879
18. Barois T., Viggiano B., Basset T., Cal R.B., Volk R. Compensation of seeding bias for particle tracking velocimetry in turbulent flows. *Physical Review Fluids*. 2023;(8):1—16. https://doi.org/10.1103/PhysRevFluids.8.074603
19. Viggiano B., Basset T., Bourgoin M., Cal R.B., Chevillard L., Meneveau Ch., Volk R. Lagrangian modeling of a nonhomogeneous turbulent shear flow: Molding homogeneous and isotropic trajectories into a jet. *Physical Review Fluids*. 2024;(9):1—13.
https://doi.org/10.1103/PhysRevFluids.9.044604
20. Xinchen Zhang, Zhen Zhang, Alfonso Chinnici, Zhiwei Sun, Javen Qinfeng Shi, Graham J. Nathan, Rey C. Chin. Physics-informed data-driven unsteady Reynolds-averaged Navier—Stokes turbulence modeling for particle-laden jet flows. *Physical Review Fluids*. 2024;(36):1—23. https://doi.org/10.1063/5.0206090
21. Timothy C.W. Lau, Graham J. Nathan. Inuence of Stokes number on the velocity and concentration distributions in particle-laden jets. *Journal of Fluid Mechanics*. 2014;(757):432—457.
https://doi.org/10.1017/jfm.2014.496
22. Aitor Amatriain, Corrado Gargiulo, Gonzalo Rubio. Generalized wall-modeled large eddy simulation model for industrial applications. *Physics of Fluids*. 2024;(36): 1—21. https://doi.org/10.1063/5.0180690
23. Jonathan B. Freund. Nozzles, turbulence, and jet noise prediction. *Journal of Fluid Mechanics*. 2019;(860):1—4. https://doi.org/10.1017/jfm.2018.823
24. Muppidi S., Mahesh K., Direct numerical simulation of round turbulent jets in crossflow. *Journal of Fluid Mechanics*. 2007;(574):59—84.
https://doi.org/10.1017/S0022112006004034
25. Yu Zhou, Dewei Fan, Bingfu Zhang, Ruiying Li, Bernd R. Noack Artificial intelligence control of a turbulent jet. *Journal of Fluid Mechanics*. 2020;(897): 1—46. https://doi.org/10.1017/jfm.2020.392
26. Khudyakov P.Yu. Gas dynamics and heat transfer during collision of straight-flow gas jets: Abstract of the dissertation ... Cand. Sci. (Phys.-Math.). Ekaterinburg: UrFU, 2013. (In Russ.).
Худяков П.Ю. Газодинамика и теплообмен при соударении прямоточных газовых струй: Автореф. Дис. ... канд. физ.-мат. наук. Екатеринбург: УрФУ, 2013.
27. Phoebe Kuhn. Linear modeling of coherent structures in the self-similar region of a round turbulent jet: Diss. ... Dr. Eng. Berlin: Technischen Universität Berlin, 2023. https://doi.org/10.14279/depositonce-18798
28. Velkin V.I., Shkolny A.V., Kirillov M.P., Achkeev M.V., Gurin A.A. Swirler: Patent 2321779 (RF). 2006. (In Russ.).
Велькин В.И., Школьный А.В., Кириллов М.П., Ачкеев М.В., Гурин А.А. Завихритель: Патент 2321779 (РФ). 2006.
29. Francis B.J., Joubert H., Bakker M.L., Nikolic S., Gwynn-Jones S. Lance for use in a top submerged lance furnace. WO 2017/195105. 2017.
30. Shatokhin I.M., Kuzmin A.L. Method of circulating vacuuming of liquid metal, system and devices for its implementation: Patent 2213147 (RF). 2003. (In Russ.).
Шатохин И.М., Кузьмин А.Л. Способ циркуляционного вакуумирования жидкого металла, система и устройства для его осуществления: Патент 2213147 (РФ). 2003.
31. Zemtsov G.A., Puchkov A.E., Frolov L.I. Furma: Patent 2355779 (RF). 2009. (In Russ.).
Земцов Г.А., Пучков А.Е., Фролов Л.И. Фурма: Патент 2355779 (РФ). 2009.

Information about the authors

Vladimir A. Kirsanov – Advisor to the General Director for Engineering, Ural Research and Design Institute of Mining Processing, Metallurgy, Chemistry, Standartization (JSC "Uralmekhanobr").
E-mail: Kirsanov_VA@umbr.ru

Yuri F. Poberezhny – Head of the Bureau of Engineering and Innovation, JSC "Uralmekhanobr".
E-mail: Poberezhny_YF@umbr.ru

Nikolai G. Mikhailov – Leading Engineer of the Technological Audit Department, JSC "Uralmekhanobr".
https://orcid.org/0009-0006-2019-019X
E-mail: Mikhaylov_NG@umbr.ru

Maxim M. Sladkov – Chief Engineer of the Sredneuralsky Copper Smeltery (JSC "SUMZ").
E-mail: M.Sladkov@sumz.umn.ru

Sergey N. Gotenko – Head of the Technical Department, JSC "SUMZ".
E-mail: S.Gotenko@sumz.umn.ru

Информация об авторах

Владимир Андреевич Кирсанов – советник ген. директора по инжинирингу Уральского научного-исследовательского и проектного института обогащения и механической обработки полезных ископаемых (АО «Уралмеханобр»).
E-mail: Kirsanov_VA@umbr.ru

Юрий Федорович Побережный – начальник бюро инжиниринга и инноваций АО «Уралмеханобр».
E-mail: Poberezhny_YF@umbr.ru

Николай Григорьевич Михайлов – вед. инженер отдела технологического аудита АО «Уралмеханобр».
https://orcid.org/0009-0006-2019-019X
E-mail: Mikhaylov_NG@umbr.ru

Максим Михайлович Сладков – гл. инженер Среднеуральского медеплавильного завода (АО «СУМЗ»).
E-mail: M.Sladkov@sumz.umn.ru

Сергей Николаевич Готенко – начальник технического управления АО «СУМЗ».
E-mail: S.Gotenko@sumz.umn.ru

Contribution of the authors

V.A. Kirsanov – general supervision, editing of the article.

Yu.F. Poberezhny – participation in the discussion of results.

N.G. Mikhailov – data processing and preparation of the article.

M.M. Sladkov – resource support for the research.

S.N. Gotenko – resource support for the research.

Вклад авторов

В.А. Кирсанов – общее руководство, редактирование текста статьи.

Ю.Ф. Побережный – участие в обсуждении результатов.

Н.Г. Михайлов – обработка результатов исследования, подготовка статьи.

М.М. Сладков – ресурсное обеспечение исследования.

С.Н. Готенко– ресурсное обеспечение исследования.

The article was submitted 21.05.2024, revised 29.10.2024, accepted for publication 31.10.2024

Статья поступила в редакцию 21.05.2024, доработана 29.10.2024, подписана в печать 31.10.2024